# Measuring the quasar luminosity function below the detection threshold

*Author:*

Eliab Malefahlo

*Supervisors:*

Prof MARIO SANTOS
Dr JONATHAN ZWART
Prof MATT JARVIS
Prof ROY MAARTENS

**UNIVERSITY** *of the*
**WESTERN CAPE**

*A thesis submitted in fulfilment of the requirements*
*for the degree of Msc Astronomy*

*in the*

Astronomy group
Department of Physics and Astronomy

March 2016

# Declaration of Authorship

I, Eliab Malefahlo, declare that this thesis titled, 'Measuring the quasar luminosity function below the detection threshold' and the work presented in it are my own. I confirm that:

- This work was done wholly or mainly while in candidature for a research degree at this University.

- Where any part of this thesis has previously been submitted for a degree or any other qualification at this University or any other institution, this has been clearly stated.

- Where I have consulted the published work of others, this is always clearly attributed.

- Where I have quoted from the work of others, the source is always given. With the exception of such quotations, this thesis is entirely my own work.

- I have acknowledged all main sources of help.

- Where the thesis is based on work done by myself jointly with others, I have made clear exactly what was done by others and what I have contributed myself.


Signed:

_____

Date:

_____

University of the Western Cape

# *Abstract*

FACULTY NATURAL SCIENCE

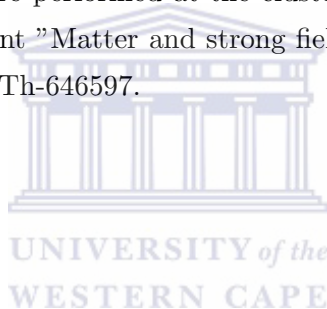Department of Physics and Astronomy

Msc Astronomy

**Measuring the quasar luminosity function below the detection threshold**

by Eliab Malefahlo

The radio emission of radio-quiet active galactic nuclei (AGN) is thought to be from star formation and AGN related emission. I investigate these sources using 1.4 GHz radio data from FIRST and three optical quasars samples from the SDSS: (i) a volume-limited sample in the redshift range $0.2 < z < 0.4$ defined by $M_i < -23$ (ii) magnitude-limited sample in the redshift range $1.8 < z < 2.5$ defined by $m_r \leq 18.5$ and (iii) a uniform sample in the redshift range $0.2 < z < 3.5$ (divided into 12 redshift bins). I constructed radio source counts and radio luminosity functions (RLFs) using the optical quasars detected in FIRST, which are consistent with literature results obtained using SDSS and NVSS quasars. There are differences at the low fluxs end because of the different resolutions of FIRST and NVSS. I applied a median stack method to the 12 redshift bins of the uniform sample and found that the median flux decreases from 182 $\mu$Jy in the lowest redshift bin to 39 $\mu$Jy and the highest redshift bin. This is because the high redshift quasars although more luminous than their low redshift counterparts, they are much further away so they have lower fluxes. I probed the quasar radio source counts to lower levels using reconstructed source counts obtained by applying the Bayesian stack technique. The reconstructed radio source counts were then used to constructed the quasar RLF to lower levels, where I found: (i) for $z < 1$ the constructed quasar RLF has the same slope as the detected quasars, suggesting that like the detect quasars their radio emission is dominated by AGN related emission (ii) above $z = 1$ the constructed RLF steepens with redshift, which suggests the strong link between accretion rate and radio jet power is gradually breaking down towards faint optical luminosities at high redshift.

# *Acknowledgements*

# Contents

# Chapter 1

# Introduction

In this thesis, I use a Bayesian stacking (Bayestack) technique to extend measurements of the quasar radio luminosity function (QRLF) and source counts of optically selected sources below the detection threshold of currently completed large-area radio surveys. I use the results to investigate the role of star formation and active galactic nuclear accretion (AGN) activity on the radio emission of quasars, in particular the radio-quiet quasars. First, I explore the importance of these two sources of emissions for galaxy formation and evolution.
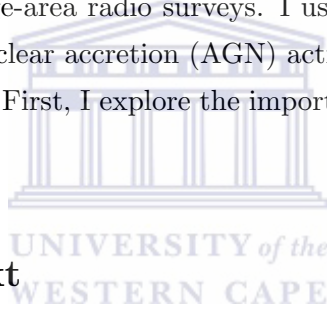
## 1.1 Cosmological context

### 1.1.1 Evolution of the Universe

The Big Bang theory is the most accepted evolutionary model of the Universe (see Peebles and Ratra [2003] for an overview). The theory states that the Universe originated from a singularity with infinite temperature and density, expanding to what is observed today (assuming general relativity holds in the early Universe; Hawking and Ellis [1973]). The Universe expanded and cooled growing exponentially in size over a short time scale $10^{-33}$ to $10^{-32}$ (inflation; e.g. Guth and Jagannathan [1998]). After inflation, elementary particles were formed and as the Universe continued to expand and cool some particles combined to form nucleons. Around 380,000 years after the Big Bang, the Universe became cool enough for atoms to form, making the Universe transparent because the free electrons that were scattering photons were captured to form these atoms (recombination).

The Big Bang model is a solution to Einstein's field equations by Alexander Friedman where he assumed an isotropic and homogeneous space on large scales. One of the strongest pieces of evidence supporting the model is the prediction of the Cosmic Microwave Background (CMB, Penzias and Wilson [1965]) radiation, the thermal afterglow of the Universe after recombination. The background
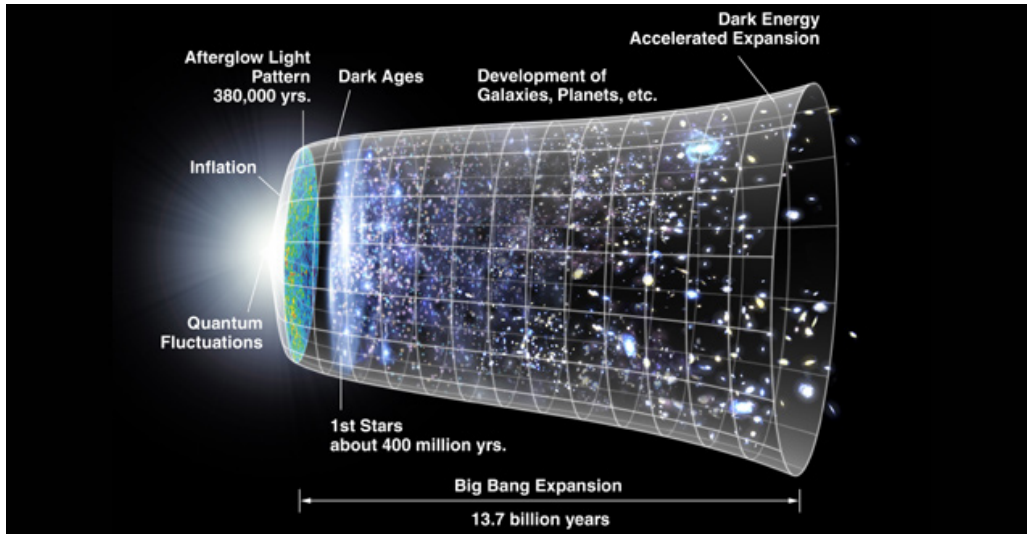
FIGURE 1.1: An artist impression on the time scale of the evolution of the Universe according to the Big Bang model. (NASA/WMAP science team).

radiation is an almost perfectly uniform blackbody with temperature fluctuations of the order $10^{-5}$ (Smoot et al. [1992]). Further evidence for the Big Bang includes; the expansion of the Universe (i.e. Hubble's law; Hubble [1929]) and the abundance of elements observed today (Alpher et al. [1948]). Measurements of the fluctuations in the CMB together with galaxy distribution measured in galaxy surveys place tight constraints on the cosmological parameters and favours the so-called ΛCDM model. This is parameterized with four types of matter: dark matter, baryonic matter, hot dark matter (radiation) and dark energy, the latter component dominates the current energy budget of the Universe and is responsible for the accelerated expansion of the Universe. The latest results from Planck Collaboration et al. [2015] give a Hubble constant, $H_0 = 67.8 \pm 0.9$ km s$^{-1}$Mpc$^{-1}$ and a dark matter density, $\Omega_m = 0.308 \pm 0.012$. The model, however, is not perfect and in solving some of its problems other problems arise.

The problems with the ΛCDM model arises when there is discrepancy between its predictions and observations. This leads to the introduction of quantities such as dark matter and dark energy to account for this discrepancy. Dark matter is used to account for the missing mass needed to explain the kinetic motions observed (i) from rotation curves of stars orbiting galactic centres (Rubin et al. [1980]) and (ii) in galaxies rotating about the centre of mass of their clusters (Zwicky [1937]). Dark matter makes up $\approx 90\%$ of matter and only interacts gravitationally, possibly weakly as well, with baryonic matter but does not absorb or emit electromagnetic radiation. Dark energy is the term given to the mysterious force pushing the expansion of the Universe in spite the gravitational force (Lemaître [1927],Hubble [1929]). It has recently been found that not only is the Universe expanding but that the expansion is accelerating (Riess et al. [1998], Perlmutter et al. [1999]). Dark matter makes up $\approx 70\%$ of the energy density of the Universe while baryonic matter makes up $\approx 30\%$.
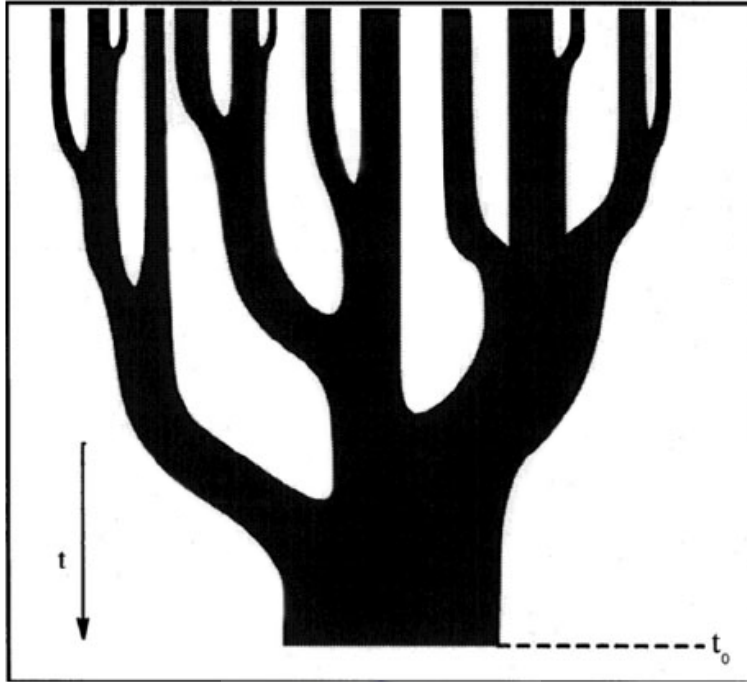
FIGURE 1.2: The hierarchical structure formation as small dark matter particles (branches) merge to form larger dark matter particles at time $t_0$ (Lacey and Cole [1993]).

### 1.1.2 Galaxy formation and evolution

The large-scale structure observed in the Universe today grew from the tiny fluctuations of the near-perfectly uniform early Universe under the influence of gravity. The growth of cosmic structure follows hierarchical formation (Lacey and Cole [1993]; Fig. 1.2), where smaller dark matter halos (branches) merge to form larger halos at later times. Galaxies form when baryons cool and collapse following the gravitational potential of the dark matter halos.

The evolution of dark-matter halos through hierarchical structure formation can be understood through N-body simulations (e.g. Springel et al. [2005]). The evolution of baryonic matter is more challenging because most of the physical processes governing their interactions are still rather poorly understood (e.g. star formation, supernovae feedback, AGN accretion and feedback). Models of galaxy formation use simplification and approximations to account for these complex processes, to model the evolution and distribution of galaxies in dark matter halos (e.g Somerville et al. [2008]). As a result, most N-body simulations can produce galaxy clustering that agree with large surveys (e.g. Campbell et al. [2015] found results that are consistent with those from the Galaxy and Mass Assembly Survey (GAMA; Driver et al. [2011]) $z < 0.7$, however, found discrepancies with SDSS and VIMOS Public Extragalactic Redshift Survey (VIPERS; Guzzo et al. [2014])), but have problems producing the relative galaxy abundances and masses.
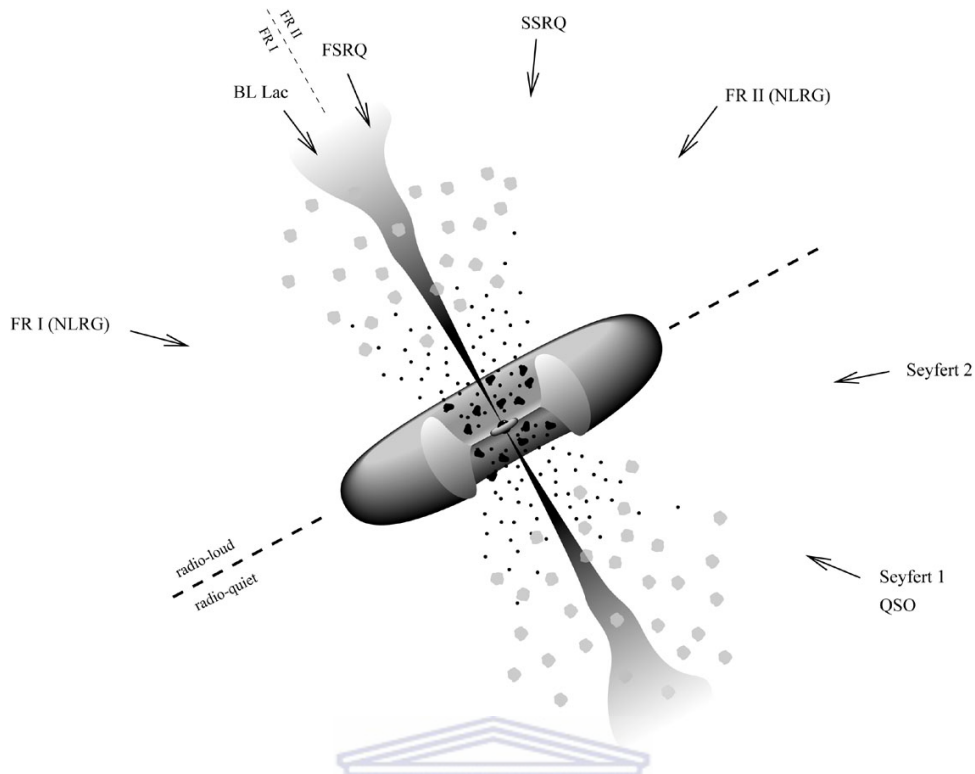
FIGURE 1.3: The unified model of AGN which explains the types of AGN by different observation angles. The arrows represent the observation angle, with respect to the jets, to observe a specific AGN type. Blazars Lacertae (BL Lac) and flat-spectrum radio quasars (FSRQ) have an unobscured view of the central region while steep spectrum radio quasars (SSRQ) and Fanaroff and Riley (FR: Fanaroff and Riley [1974]) narrow-Line Radio galaxies (NLRG) are obscured by the torus. On the radio quiet side, Seyfert 2 galaxies have a more edge-on view than Seyfert 1 and radio-quiet quasars (QSO). Adapted from Urry and Padovani [1995];Padovani et al. [1997]

## 1.2  Galactic processes

Galaxies are observed with different shapes and sizes, ranging from giant spherical blobs of red stars (elliptical) to disk galaxies with well-arranged gas and stars (spirals). These features have been observed since 1845 when William Parsons recorded a spiral structure in what was then known as a nebula within the Milky Way. Hubble [1925] proved that some of these nebulae are galaxies in their own right that came with a large variety of morphologies, which led to the first classification scheme known as Hubble's Tuning Fork (Hubble et al. [1936]).

The different shapes and sizes of galaxies result from interaction with each other gravitationally, through collisions and mergers or lack thereof. The exchange of material during this interaction influences the physical processes (star formation, AGN accretion and feedback), which in turn influence the properties of the galaxy.

### 1.2.1   Star formation

Star formation (SF) is a process where stars form from the collapse of a giant molecular cloud. The molecular clouds are self-gravitating regions mostly made up of hydrogen ($H_2$) and Carbon monoxide (CO). A typical cloud has a mass of $\approx 10^{5-6} M_\odot$ and average densities of $\approx 10^2$ cm$^{-3}$ (Williams et al. [2000]). Star formation occurs when some external stimulus causes instability in a smaller clump within the molecular cloud, which leads to the collapse of the clump under its own weight as it collapses the central temperature increases. The clump splits into smaller fragments, which also individually continue to collapse until the central regions of the fragments reach the required temperature needed to ignite nuclear fusion. The fusion generates outward (radiation) pressure that balances the gravitation force. The newly-born stars send winds and shock waves to the surrounding gas, which can prevent SF (negative feedback) or stimulate SF (positive feedback). Stars form according to the initial mass function (Elmegreen [1997]), whereby lower mass stars are more likely to form than their high-mass counterparts. The death of these high-mass stars usually results in a core collapse supernovae explosion, which sends shock waves to the surrounding gas (supernovae feedback).

The star formation rate (SFR) of a galaxy quantifies the average rate at which stars form in the galaxy, measured in solar masses per year ($M_\odot$ yr$^{-1}$). The SFR depends on the amount of molecular gas available as well as other processes that affect the gas (feedback and AGN accretion). The availability of large multi-wavelength data from various surveys has allowed for detailed studies of the phases and processes that lead to individual star formation as well as measurements of star-formation rates out to high redshifts (Dunne et al. [2009]; Karim et al. [2011], Zwart et al. [2014]). A typical galaxy such as the Milky Way has a SFR of 1 $M_\odot$ yr$^{-1}$, there are galaxies that have a low SFR and those that undergo an extremely high SFR $> 1000 M_\odot$ yr$^{-1}$. A typical galaxy type that has a low SFR is the old dead Ellipticals which mostly contain old stars with very little gas. Galaxies that have extremely high SFR are known as starbursting galaxies, which is a short-lived phase of a galaxy which is usually triggered by mergers or other forms of gravitational interaction with nearby galaxies.

Measuring the star-formation (SF) history of galaxies is important for understanding galaxy evolution; it allows measurements of the growth of stellar mass, and it allows measurements of supernova rates and can constrain cosmological parameters (see e.g. Karim et al. [2011] for an overview). SF leads to radio emission and there is a tight relation between SFR and the radio luminosity.

### 1.2.2   Active galactic nuclei

Recent studies have shown that local massive galaxies all contain a super-massive black hole (SMBH) at their centres (e.g. Tanaka et al. [1995]). An active galactic nuclei (AGN) is the central region of an
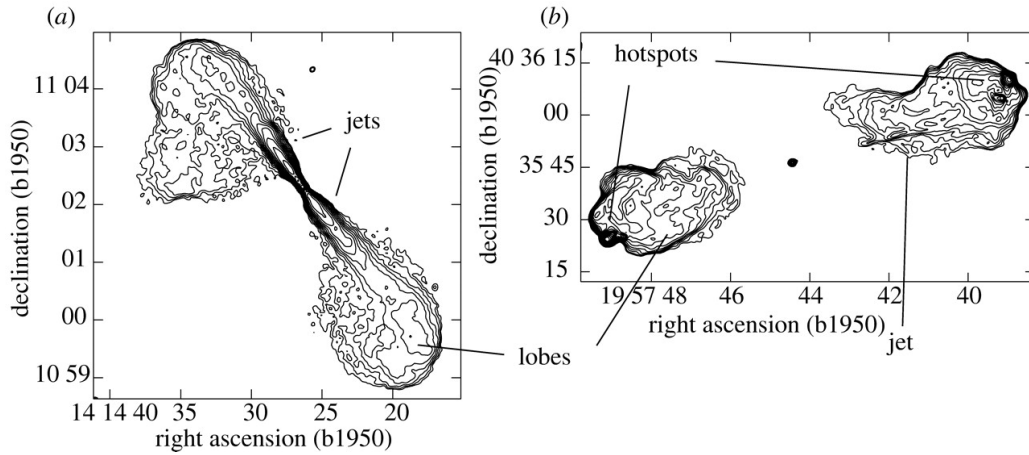
FIGURE 1.4: (a) shows the FRI radio galaxy 3C 296 (Leahy and Perley [1991]) and (b) shows the FRII radio galaxy Cygnus A Perley et al. [1984]. In both panels the contours represent the surface brightness (Hardcastle [2005]).

active galaxy (i.e one where matter is accreted onto the SMBH). The sources of radiation from an AGN are: (i) a fraction of the potential and kinetic energy of falling matter are converted into radiation, (ii) synchrotron radiation (Section 1.2.4) from the material in the jets and (iv) free-free (Bremsstrahlung) emission from accelerating/decelerating particles in the jets. Without gas to accrete, an AGN would shut down; for this reason, AGNs are usually found in galaxies with young stellar populations (more gas; Schawinski et al. [2009]) and typical have life span of $\approx 10^8$yr (Woltjer [1959]).

A typical picture of a (radio-loud) AGN includes an accretion disk surrounded by a thick dusty torus in the plane of the accretion flow and collimated jets of relativistic particles along the poles of the torus (Fig. 1.3). It is well established that the appearance of an AGN depends on the observing angle instead of underlying physical properties (Urry and Padovani [1995]). AGN are divided into two main types, type I and type II. Type I AGN are those seen from the line-of-sight of the black hole (i.e. unobscured) and contain broad emission lines produced by gas rapidly rotating around the black hole (denoted by the dark blobs in Fig. 1.3). Type II AGN are orientated so that the torus obscures the central black hole; these have narrow emission lines from the gas further away from the centre rotating less rapidly (Peterson [1997]).

Fig. 1.3 also shows AGN division related to the radio loudness. Radio-loud AGN have greater radio luminosities than radio-quiet (the technical definitions is given in Section 1.3). The old unification model claimed that radio-loud and radio-quiet AGN have similar processes just viewed from a different angle (e.g. Urry and Padovani [1995]; Fanidakis et al. [2011]). Some authors also claimed that radio-quiet AGNs are just scaled-down versions of radio-loud AGNs (e.g. Ulvestad et al. [2005]). However; they are essentially two different objects; radio-loud AGNs are mainly powered by synchrotron emission in the jets and radio-quiet AGN are mainly powered by SF (e.g.Padovani et al. [2011] Kimball
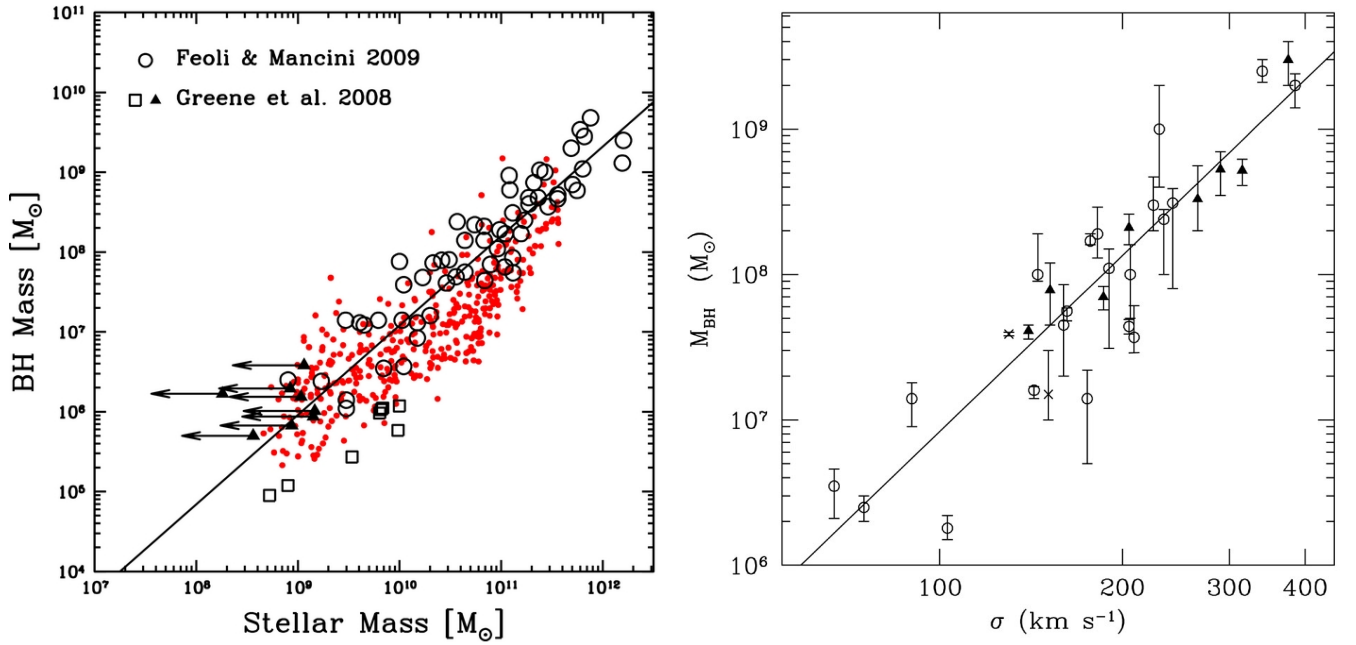
FIGURE 1.5: (left) The correlation between total stellar mass in the bulge and the mass of the black hole (BH mass). The red dots are from a simulation by Jahnke and Macciò [2011]; the open circles and triangles are observed data from Feoli and Mancini [2009] and Greene et al. [2008] respectively. (right) The black hole mass and dispersion velocity ($\sigma$) correlation, adapted from Kormendy and Richstone [1995].

et al. [2011b] ; Condon et al. [2013]) and radiation related directly or indirectly to AGN accretion (e.g. Gruppioni et al. [2003]; Jarvis and Rawlings [2004]). Radio-loud AGN are common in ellipticals and radio-quiet are common in SF spiral hosts (Dunlop et al. [2003]). Furthermore, radio-loud AGNs are thought to contain a binary SMBH system while radio-quiet have a normal SMBH (e.g. Sillanpää [1999]).

The final division considered in Fig. 1.3 is associated with the FR type I and type II classification by Fanaroff and Riley [1974]. FRI are galaxies with symmetric radio jets with most of their luminosity concentrated in the centre. FRII galaxies are more luminous than FRI, they have jets with lobes that contains bright hotspots at the end (Fig. 1.4).

### 1.2.3  Feedback

Studies on local galaxies have shown an interesting correlation between the mass of a SMBH and the total stellar mass of the bulge (Fig. 1.5a; e.g. Tremaine et al. [2002]) and an even tighter correlation between the SMBH mass and the stellar bulges' velocity dispersion (Fig. 1.5b; e.g. Gebhardt et al. [2000], Ferrarese and Merritt [2000]). These correlations suggest that there is a connection between the formation and evolution of SMBH and the bulge (Gebhardt et al. [2000]).Chen et al. [2013] found

a correlation between SFR and the black-hole accretion rate (linked by feedback).

Feedback is a process that regulates the growth of a galaxy, positive feedback leads to growth and negative feedback suppresses growth. There are various types of feedback process, the main ones being SN feedback and AGN feedback. SN feedback occurs when a supernovae goes off and sends shock waves and energy to the intergalactic medium (IGM). This can lead to growth (positive feedback) when the shock waves triggers a collapse of a cloud in the IGM and it can also lead to negative feedback when the energy released heats up the IGM, suppressing star formation (e.g. Best [2007]). AGN feedback is in the form of radio jets. Negative feedback is when the IGM is heated by the radiation from jets and gas is expelled from the galaxy (the expelled gas could have fuelled the AGN (e.g. Morganti et al. [2013]) or collapsed to form stars is expelled and the heated gas suppresses star formation). Silk [2013] claiming that jets can initiate SF by stimulating the collapse of a molecular cloud (positive feedback). Further observational evidence of positive feedback in high-redshift quasars is shown by Kalfountzou et al. [2014].

### 1.2.4 Synchrotron radiation

Synchrotron radiation is the emission produced when charged particles gyrate in a magnetic field with relativistic velocities (Elder et al. [1947]). The frequency of the radiation depends on the strength of the magnetic field and the velocity of the charged particles. The spectrum from charged particles is due to those electrons gyrating at the fundamental frequency as well as its harmonics (which are closely spaced), making the emission continuous (Grishanin et al. [1991]). The radiation is observed to be linearly polarized when the line-of-sight is perpendicular to the magnetic field, circularly polarized the line-of-sight parallel to the magnetic field and elliptically polarized when the line-of-side is in between perpendicular and parallel. This process is common in astronomical environments and is responsible for radio emission from jets in AGN, galaxies and supernova remnants.

Synchrotron emission is the dominant source of radiation in star-forming galaxies from the supernova shock of young high-mass stars, which amplifies the magnetic fields and accelerates electrons to relativistic velocities. It is also the main source of radio emission in AGN.

### 1.2.5 Far-Infrared Radio correlation

There is a known correlation between far-infrared (FIR) emission and radio emission found in local star-forming galaxies (Helou et al. [1985]), which holds over four orders of magnitude in luminosity (Condon et al. [1992]). The FIR radiation is produced when dust absorbs ultraviolet (UV) photons from young massive stars (that ends their lives with a supernovae explosion) and thermally re-emits

in the FIR. The supernova emits both UV radiation and synchrotron radiation, thus, they both trace the SFR of massive stars. The advantage of this correlation is that radio, unlike optical and UV, is not obscured by dust and has higher angular resolution reducing confusion. The correlation holds to high redshifts ($z > 2$) without evolving (e.g. Carilli et al. [2000], Sargent et al. [2010]). However, like with many tracers, there is contamination from synchrotron emission produced by AGN.

## 1.3    Radio sources

Extragalactic radio sources can be divided into two populations as mentioned earlier; radio-loud and radio-quiet. Radio-loud sources are defined to have radio luminosities above a chosen boundary (e.g. $\log_{10}[L_{8.4\text{GHz}} \text{ WHz}^{-1}] > 25$ (Hooper et al. [1996]). A better measure of radio loudness is defined by the ratio of the optical and radio luminosities (Schmidt [1970]). Kellermann et al. [1989] used luminosity from 5 GHz in the radio and from B-band (4400Å) in the optical, defining radio-loudness as an radio-to-optical ratio $> 10$. At a frequency of 1.4 GHz, radio-loud sources mostly have flux densities above 1 mJy, below which radio-quiet sources start to dominate. Some authors argue that the division between radio-loud and radio-quiet is a result from optical selections, claiming that the radio luminosity of AGN to be continuous (Lacy et al. [2001]).

### 1.3.1    Radio-loud

Radio-loud sources consist of mostly all the radio-loud AGN; Quasars, FRI, FRII, radio galaxies and blazars, making up only $\approx 10\%$ of the known sample of AGNs. These are all extremely luminous AGNs with typical luminosities $\log_{10}[L_{1.4\text{GHz}} \text{ WHz}^{-1}] \approx 24$, spanning several orders of magnitude. Fig. 1.6 shows that these sources dominate counts from flux densities $> 1$ mJy and peak at 1 Jy at 1.4 GHz (e.g Mitchell and Condon [1985]; Condon et al. [2012]). Numerous multi-wavelength studies of these objects have been conducted since their discovery in the 1940s, but there is a great deal of the processes that are not well understood (e.g. how jets are formed or why certain AGN do not have them).

### 1.3.2    Radio-quiet

Radio-quiet sources have fainter radio luminosities (and smaller radio-to-optical ratio $< 10$) than the radio-loud sources. At 1.4 GHz, radio-quiet sources dominate the counts at $< 1$ mJy (Fig. 1.6). These sources are mainly powered by synchrotron emission from SF; in fact until recently it was thought that SF was the only source of radiation at these fluxes. However, authors argued that (both radio-loud and radio-quiet) AGN have an important contribution to the $< 1$ mJy flux densities ( e.g. Gruppioni et al. [2003], Jarvis and Rawlings [2004], Padovani et al. [2011], [2014], Norris et al. [2013]). Observations
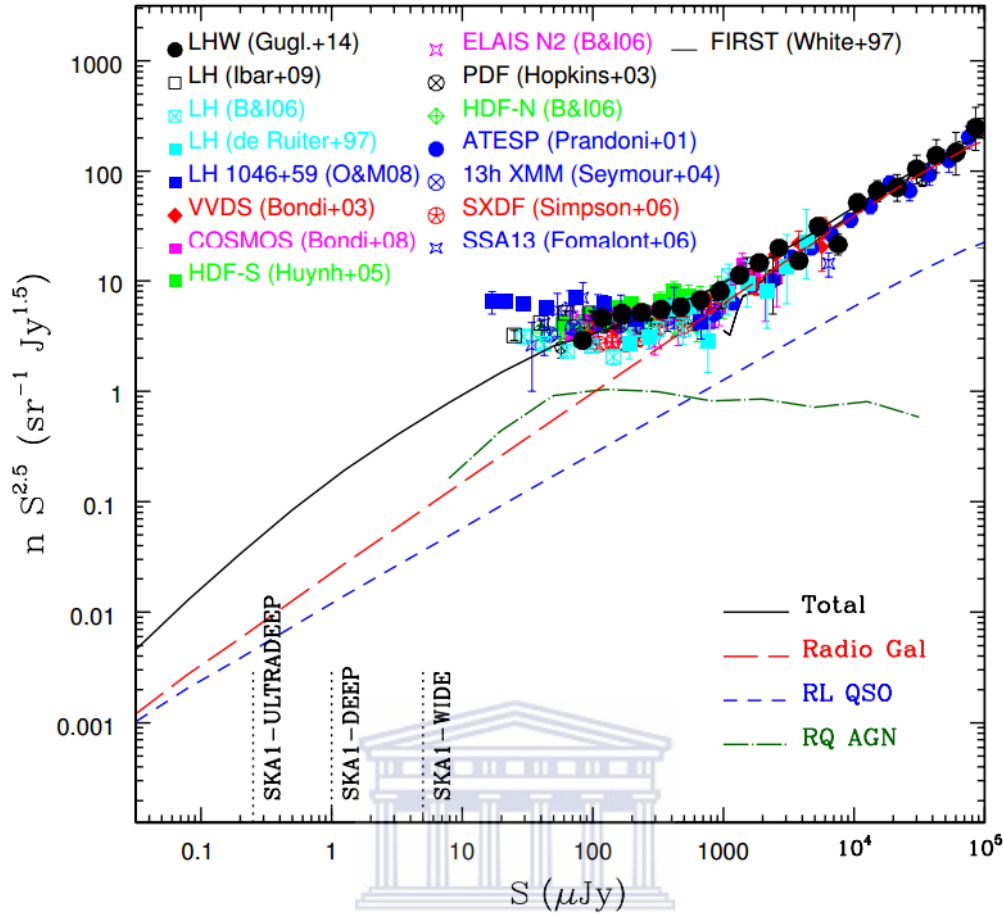
FIGURE 1.6: The observed 1.4 GHz source counts and simulated counts from various authors (de Ruiter et al. [1997]; White et al. [1997]; Prandoni et al. [2001]; Hopkins et al. [2003]; Bondi et al. [2003]; 2008; Seymour et al. [2004]; Huynh et al. [2005]; Biggs and Ivison [2006]; Fomalont et al. [2006]; Simpson et al. [2006]; Owen and Morrison [2008]; Ibar et al. [2009]; Guglielmino et al. [2014]). The simulated counts are taken from the SKADS model (Wilman et al. [2008];2010) and are divided into Radio galaxies, radio-loud quasars and radio-quiet AGN. The $5\sigma$ limits of SKA1 wide, deep and ultradeep surveys are also shown.

(e.g. Padovani et al. [2014]) show that AGN make up $\approx 40\%$ and radio-quiet AGN make up $\approx 25\%$.

Studying radio-quiet AGNs is rather important as they make up a large fraction of the AGN population. They can, therefore, help shed light on the mysteries of AGN and galaxy evolution; for example understanding the interaction between AGN feedback and SF (plus they are associated with SF galaxies).

## 1.4   Quasars

Quasi-stellar radio sources (quasars) are a subset of the AGN population, discovered (Hazard et al. [1963]; Schmidt [1963], Oke [1963]) in the radio as bright point sources with star-like counterparts in

the optical. Their star-like appearance made them indistinguishable from stars, but they have a broad emission spectrum different from any star (Schmidt [1963]). They were found to be galaxies at high redshifts (assuming their redshifts are cosmological).

Quasars are one of the best sources for studying the evolution of the Universe, SF history and AGNs. This is because they are among the brightest objects in the Universe, they are a member of the AGN family, and they span a large redshift range to $z \approx 7$ (e.g. Momjian et al. [2014]). Another interesting property of quasars is the unique emission that ranges from UV to x-ray which has been observed at all redshifts (Fan et al. [2004]; Shemmer et al. [2006]; De Rosa et al. [2011]), suggesting that quasars established their nature in the early Universe (Momjian et al. [2014]). However there are a few changes in quasar characteristics with redshift; (i) emission from hot dust ($\approx 1000$ K) has been observed in low-redshift quasars (Jiang et al. [2010]), (ii) there is a possible decrease in the relative fraction between radio-loud and radio-quiet AGN at high redshifts, which could mean a change in the accretion modes and BH spin of the first quasars (e.g. Dotti et al. [2013]).

Quasars, being AGNs, inherit the uncertainty in their dominant source of radio emission for $< 1$ mJy sources (Fig. 1.6). Recent studies of optically-selected quasars suggest that these sources are dominated by SF (Kimball et al. [2011a] and Condon et al. [2013]). However, White et al. [2015] used deeper optical and near-infrared selection of quasars and they suggest that the radio emission is dominated by AGN accretion. The investigation was extended to infrared where Rosario et al. [2013]; showed that infrared emission from radio-quiet low luminosity AGN correlates with star formation and hence the radio emission as well (FIR-radio correlation; Section 1.2.5) (Bonzini et al. [2015]; Padovani et al. [2015]). However, Zakamska et al. [2016] extended the analysis of Rosario et al. [2013] to two orders of magnitude of luminosity and found the emission is more likely associated with accretion (Lal and Ho [2010]; Harrison et al. [2014]).

Although quasars were first discovered in the radio, Sandage [1965] found that quasars can be identified solely through their optical emission as they have a unique spectrum that is different from stars. Since then quasar were mostly discovered through the use of optical surveys.

A large sample of quasars is needed to resolve the ongoing debates about AGN and quasar emissions. However, quasars are hard to find and thus require large surveys like the Large Bright Quasar Survey (LBQS; Morris et al. [1991]) the 2dF Quasar Redshift Survey (2QZ; Boyle et al. [2000]) and the successive releases of the Sloan Digital Sky Survey (SDSS; York et al. [2000]) quasar catalogues are needed to representative samples. Optically selected quasars suffer from various selection effects: (i) misses reddened quasars which are observed in radio (e.g. Webster et al. [1995];Gregg et al. [2002];Holt et al. [2004]; Glikman et al. [2007]Urrutia et al. [2009] thought to be heavily obscured by dust (e.g.

Richards et al. [2003]; Young et al. [2008]). (ii) Quasars in the redshift range $2 < z < 3.5$ have similar optical colours to stars (e.g. Fan [1999]).

## 1.5   Large radio surveys

Radio surveys are crucial for studying quasars; because, although AGN typically radiate in a large range of frequencies (including UV, X-ray and optical), radio is where most of the characteristics of AGN are seen (jets and lobes) and where the types of AGN differ the most. Furthermore, the radio does not suffer from obscuration so it is sensitive to all types of AGN irrespective of their orientation. The current regime of large-area radio surveys e.g. the Sydney University Molonglo Sky Survey (SUMSS; Bock et al. [1999]), the NRAO VLA Sky Survey (NVSS; Condon et al. [1998]) and Faint Images of the Radio Sky at Twenty-centimeters (FIRST; Becker et al. [1995]) mostly detect radio-loud sources.

There is a great deal of activity in the development and upgrades of radio telescopes in preparation for the Square Kilometre Array (SKA), which is expected to reach nJy flux levels. The Low-Frequency Radio Array (LOFAR) is complete and in operation. Telescopes that have been upgraded include; the VLA (to the Jansky Very Large Array; JVLA) and MERLIN to e-MERLIN. The telescopes being built include SKA pathfinders like the More Karoo Array Telescope (MeerKAT) and the Australian Square Kilometre Array Pathfinder (ASKAP). These telescopes will survey the sky to fainter fluxes faster than existing telescope (Norris et al. [2013]; Fig. 1.7).

## 1.6   Outline

This thesis is structured in the following way: In Chapter 2, I discuss the optical data from the SDSS and radio data from FIRST. In Chapter 3, I use the detected sources to construct source counts and quasar radio luminosity functions and compare to literature. In Chapter 4, I explore the fluxes of the sources below the detection using median stacking, which returns a single statistic for a given bin. I take it a step further by constructing the sources counts of the sources below the detection threshold based on fitting a model to the data using a Bayesian approach. In Chapter 5 I summarise the results found and give future aspects of the work.

Throughout the work unless state otherwise, I use AB magnitudes. All the positions are in J2000 epoch, spectral index $\alpha = -0.7$ and $\Lambda$CDM cosmology, with $H_0 = 70$ km$^{-1}$ Mpc$^{-1}$, $\Omega_\Lambda = 0.7$ and $\Omega_m = 0.3$.
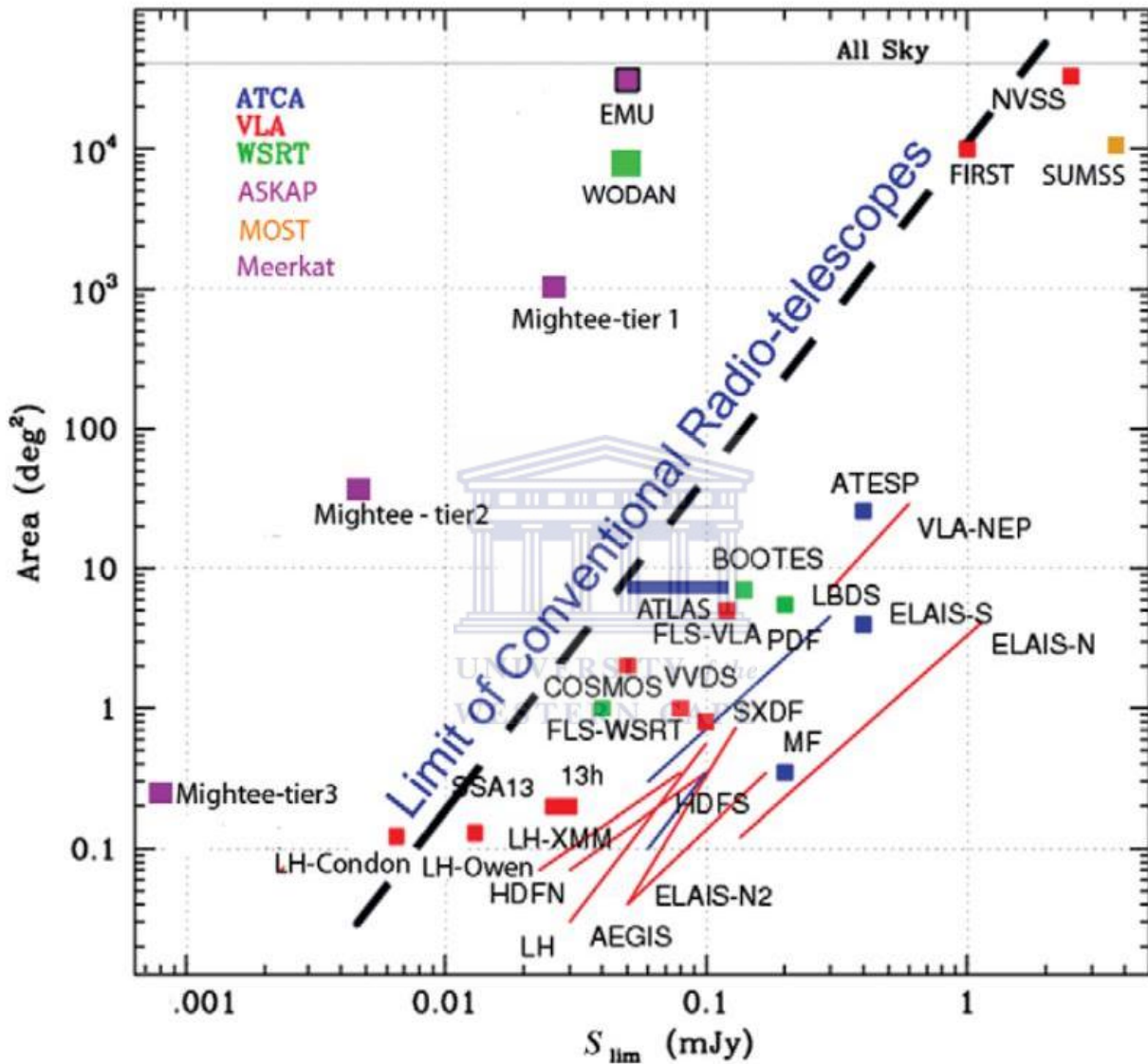
FIGURE 1.7: Next-generation and current radio-continuum surveys at 1.4 GHz. The $x$-axis is the $5\sigma$ flux limit, sensitivity increases to the left, and the $y$-axis is the survey area. The diagonal line shows the limit of current telescopes (before upgrades); this is of course mostly limited by telescope observation time, however, in 2016 it would take an unrealistic integration time to cross the line. Credit:,Norris et al. [2013]

# Chapter 2

# Data

For an experiment of this nature where one tries to obtain useful information from sources below the detection limit of a survey, one needs auxiliary data from another survey. I use FIRST radio data with deeper optical data from SDSS that contains fainter sources than First.

## 2.1 SDSS

The optical sample is drawn from the quasar catalogues of both the twelfth and final data release (DR12) of SDSS III's BOSS (Eisenstein et al. [2011]) and DR7 of SDSS II's Legacy (Shen et al. [2011]). SDSS is a spectroscopic redshift survey observed with a dedicated 2.5 metre wide-field (Gunn et al. [2006]) telescope equipped with an multi-band imaging (*ugriz* (Fukugita et al. [1996]) camera and spectrograph. SDSS started observations in 2000, covering over a third of the sky in various phases with different goals. The survey has gone through three phases, SDSS I, SDSS II, SDSS III and, currently commencing SDSS IV.

### 2.1.1 SDSS I

SDSS I (York et al. [2000]) was operational until 2005 and imaged over 8,000 square degrees of the sky in five optical bands along with spectroscopic observations of galaxies (Strauss et al. [2002],Eisenstein et al. [2001]) and quasars (Richards et al. [2002]) in what is called the Legacy survey. The quasar targets were observed in a 5,700 square degrees subset of the SDSS I imaging data (top panel of Fig 2.1 shows the footprint of these quasars). Legacy found a total of 670,000 galaxies 77,000 quasars.
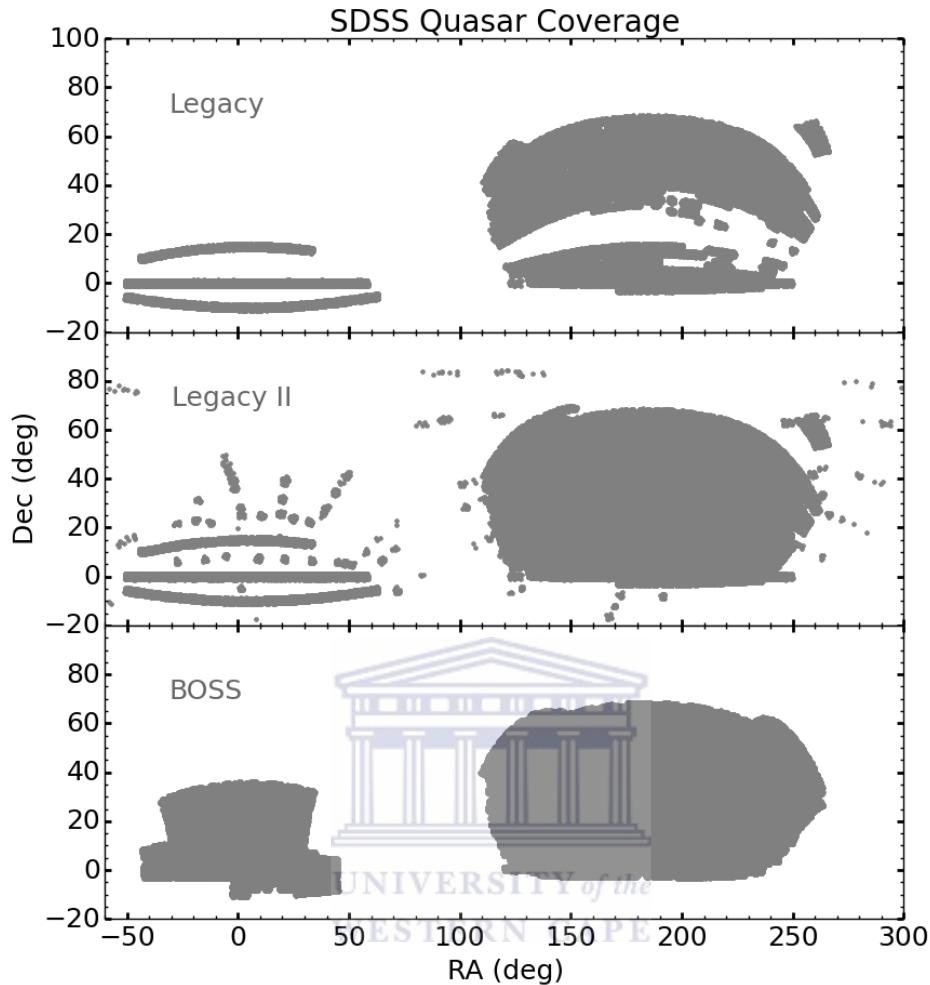
FIGURE 2.1: The quasar coverage of all the three phases of the SDSS. The top panel is SDSS I with 77,000 quasars covering an area of 5,700 square degrees, the middle panel is the SDSS II 105,000 quasars found in an area covering 7,500 square degrees. The bottom panel contains 297,301 SDSS III's BOSS quasars observed in area covering 10,000 square degrees.q

### 2.1.2  SDSS II

SDSS II was carried out between 2005 to 2008, completing the Legacy survey and starting both the SEGUE and the Sloan Supernova surveys.

(i) **Legacy Survey** provided uniform coverage in five bands of over 7,500 square degrees of the sky in the North Galactic cap (NGC) and 740 square degrees in the South Galactic cap (SGC). Most of the survey footprint was covered in SDSSI, SDSSI only observed a small part. The complete coverage of Legacy is shown in panel 2 of Fig. 2.1. It containes $\approx$ 2 million objects, $\approx$ million galaxy spectra and more than 105,000 quasar spectra.  panel 1 of Fig 2.2 shows the redshift distribution (green lines) of the Legacy quasars (Legacy II).
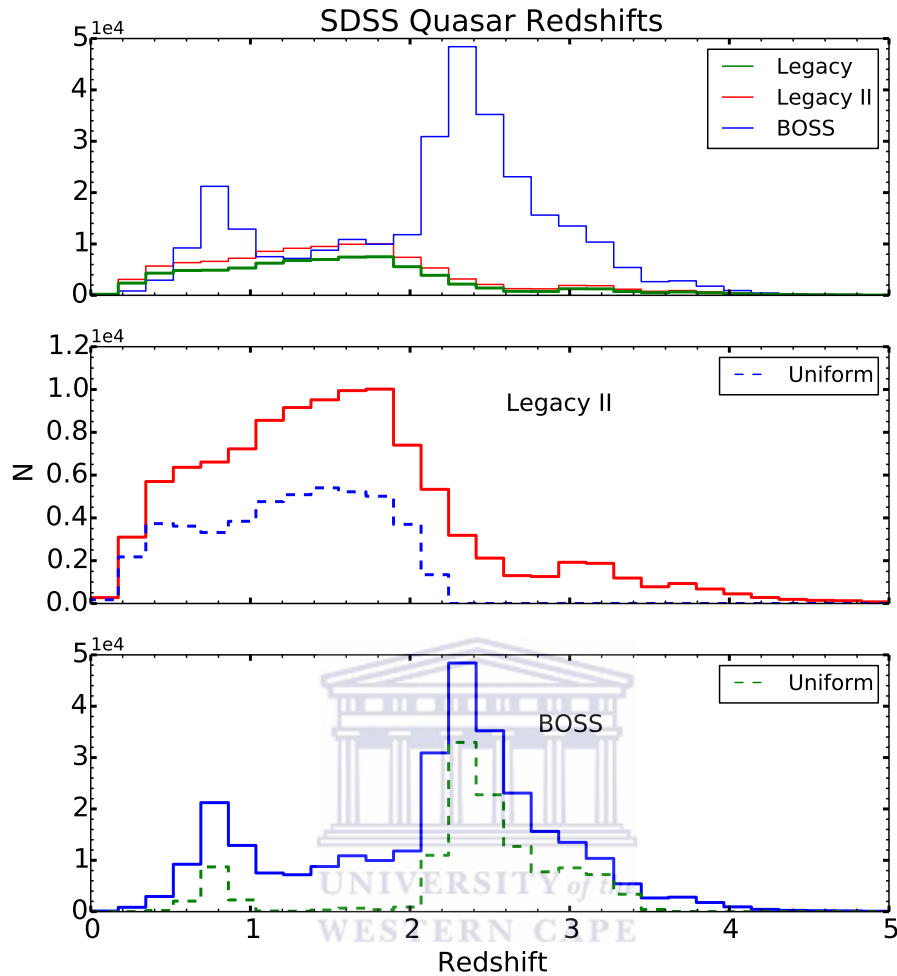
FIGURE 2.2: The redshift distribution of the SDSS quasars. The top panel is redshift distribution for the three complete phases of the SDSS, SDSS I (Legacy, green line), SDSS II (Legacy II, red line) and SDSS III (BOSS blue line). The redshift distribution of the full Legacy survey (Legacy II, red line) and the uniform subsample (blue dotted lines) are shown in the second panel. The third panel shows the uniform (green dotted lines) and full BOSS quasars (blue dotted line).

(ii) **Sloan Extension for Galactic Understanding and Exploration** (SEGUE) was a spectroscopic survey of 240,000 stars to study the structure, formation and evolution of the Milky Way (Yanny et al. [2009]).

(iii) **The Sloan Supernova survey** is a repeated imaging survey over a 300 square degree area on the Celestial Equator to search for supernovae Ia (Frieman et al. [2008]). The survey ran from 2005 to 2007 and confirmed a total of 327 type Ia supernovae events (Sako [2007]).

### 2.1.3   SDSS III

SDSS III (Eisenstein et al. [2011]) began operations in 2008 and was completed in 2014. This phase was divided into four different surveys; SEGUE-2, BOSS, APOGEE and MARVELS all conducted with the same 2.5 wide-field Sloan telescope (Gunn et al. [2006]) with the new improvements since SDSS III will observe fainter targets. The improvements include: (i) a multi-object fibre-fed optical spectrographs with new fibres; 1000 fibres with $2''$ apertures per plate instead of the previous 630 fibres with 3" apertures, (ii) new gratings CCDs and optics and (iii) a new near-infrared high-resolution spectrograph and an optical interferometer.

(i) **The Sloan Exploration of Galactic Understanding and Evolution 2** (SEGUE-2; Rockosi et al. [2015] in prep.) builds on the work from SEGUE 1. SEGUE 2 spectroscopically observed close to 119,000 unique stars in the halo of the galaxy with distances of 10 to 60 Kpc from the galactic centre. The observations were done over 1317 square degrees from 2008 to 2009.

(ii) **Multi-object APO Radial Velocity Exoplanet Large-area Survey** (MARVELS; Ge et al. [2015] in prep.) used two 60-fibre interferometric spectrographs to observe radial properties (e.g velocity) of 11,000 stars in search for exoplanets and brown dwarfs that have orbital periods from several hours to two years. MARVELS operated from 2008 to 2012.

(iii) **APO Galactic Evolution Experiment** (APOGEE; Majewski et al. [2015] in prep. ) uses a 300-fibre high resolution, high signal-to-noise infrared (H-band) spectrograph to penetrate through the dust that obscures stars, in the galactic disk, bar and bulge and halo, to investigate their dynamics and composition. The data was observed from 2011 to 2014 using stars selected from the 2MASS database.

(iv) **Baryon Oscillation Spectroscopic survey** (BOSS; Dawson et al. [2013]) used the same imaging data as SDSS I and SDSS II, with an additional area in the South Galactic Cap, to a limiting magnitude of r $\simeq$ 22.5. BOSS surveyed 7578 deg$^2$ in the NGG and 2663 deg$^2$ in the SGG, a total of 10269 deg$^2$ shown in panel 3 of Fig. 2.1. One of BOSS's key goals is to measure the baryon acoustic oscillation (BAO) scale in (i) the distribution of galaxies and neutral hydrogen (Anderson et al. [2014]) and (ii) the Lyman-$\alpha$ forest (Busca et al. [2013]). This is done using spectral information of 1.5 million luminous galaxies brighter than $i = 19.9$ with $z < 0.7$ and observations of high-redshift ($z > 2$) quasars (Busca et al. [2013]; Slosar et al. [2013]; Kirkby and BOSS Collaboration [2013]).
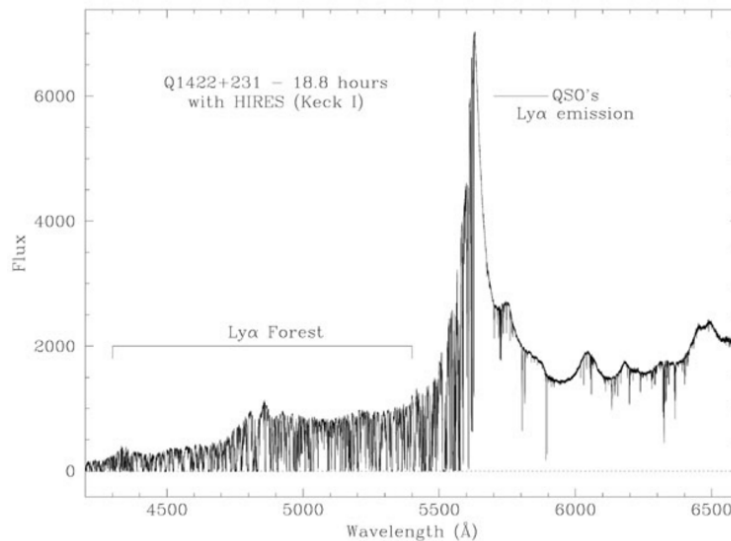
FIGURE 2.3: A spectrum of a gravitationally-lensed quasar Q1422+231 observed with the HIRES spectrograph (Vogt [1992]) on the the Keck I telescope. The high redshift quasar is observed at $z = 3.625$ and the Ly$\alpha$ forest is located around $\lambda \sim 5000$ Å, 'eating every' (line) feature of the quasar below the Ly$\alpha$ emission, (from Ellison et al. [2000]).

### 2.1.4    Quasar target selection: SDSS I and II

SDSS I and II targeted objects classified as point-like in the magnitude range $15 < i < 19.1$ (Richards et al. [2002]; 2006). This target selection catches both quasars and stars. Quasars are then differentiated from stars by their unique colours in multi-dimensional color-colour space (Fan [1999]). The colours of quasars are reduced by absorption from a phenomenon called Ly$\alpha$ forest (Lynds [1971]). The Ly$\alpha$ forest is a series of Ly$\alpha$ absorption lines, corresponding to the neutral hydrogen transition from $n = 1$ to $n = 2$, from foreground intergalactic gas. Due to their large distances, the light from a quasar passes through this intergalactic gas from different redshifts with each leaving its 'mark' in the spectra of the quasar, resulting in the absorption lines being observed at a range of wavelengths. This phenomenon has a significant effect on $z \geq 2.2$ quasars; Fig 2.3 shows the Ly$\alpha$ forest for a $z = 3.625$ quasar. However, the quasars become reddened with increasing redshift making their colours distinct from stars (Fan [1999], Richards et al. [2001b]). Quasar models by Fan [1999] show that on average quasars are well separated from the stars, with the exception to $2.7 < z < 2.8$, where quasars are indistinguishable from A stars and blue horizontal branch (BHB) stars in the $u - g$, $g - r$ colour-colour space (Fig 2.4). Quasar candidates in SDSS I and II are primary the outliers from the stellar regions in colour-colour space (Richards et al. [2001a]) (as seen in Fig 2.4) and the regions with large stellar contamination were avoided.

As mentioned earlier, one of the main goals of BOSS is to observe BAO scale in the Lyman $\alpha$ forest (Dawson et al. [2013]). This requires spectroscopic detections of $15 \geq$ per quasars deg$^{-2}$ at $z > 2.2$. To achieve this, they apply a magnitude limit of $g < 22$ giving a surface density of 20 quasars deg$^{-2}$ at
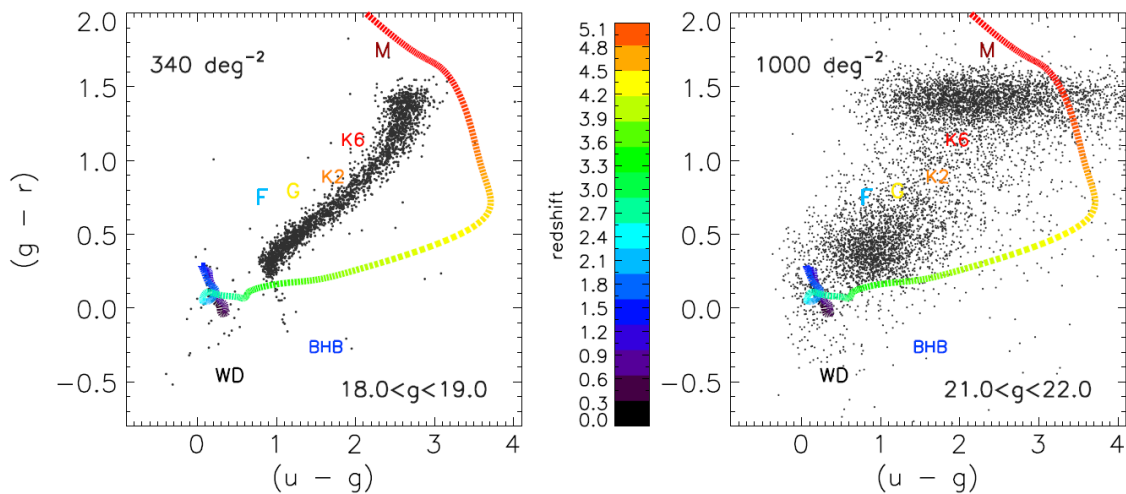
FIGURE 2.4: The colour-colour plot $(u-g)$, $(g-r)$ used to identify quasars from various stars. Quasars (models, Fan [1999]) are shown in different colours according to their redshift, blue representing low redshifts and red high redshifts, and star are represented by black points. The left panel is a subset of the brightest $(18 < g < 19)$ objects targeted by SDSS I and II, were its one can easily distinction quasars from stars except at $2.7 < z < 2.8$. The right panel is a sample of brighter objects $(21 < g < 22)$ targeted by BOSS, which has a lot of contamination from stars due to the large uncertainties in magnitudes because the their are close to SDSS's photometry limit, (taken from Ross et al. [2012]).

$z > 2.2$. The magnitude limit is very close to the detection limit of SDSS photometry (Abazajian et al. [2004]), as a result, it broadens (scatter) the stellar range in colour-colour space (Fig 2.4) therefore increasing contamination. Using the traditional colour-colour space selection will be very challenging as there is contamination from metal-poor A and F stars, faint low redshift quasars ($z \approx 0.8$) and compact galaxies which all have the same colours as the target quasars (Richards et al. [2001b]). Therefore, new quasar target selection algorithms had to be developed for BOSS to achieve its goals.

### 2.1.5   Quasar target selection: SDSS III

Since traditional colour-colour space selection of quasars can not be used, four distinct targeting algorithms are used in SDSS III; the Kernel Density Estimation (KDE; Richards et al. [2004],Richards et al. [2009a]), Likelihoods (Kirkpatrick et al. [2011]), neural network method (Yèche et al. [2010]) and the Extreme Deconvolution XD (Bovy et al. [2011a], Bovy et al. [2011b]).

(i) **Kernel Density**(KD) classification scheme was introduced by Gray and Moore [2003], and Richards et al. [2010] applied the method to SDSS imaging data. The method uses a set of (known) stellar and quasar densities in multi-dimensional colour-colour space, (similar to the left panel of Fig 2.4), as a trained sample. Objects are then given probabilities of being a quasar based on their position colour-colour space with respect to the trained sample.

(ii) **The Likelihood method** (Kirkpatrick et al. [2011]) uses a similar approach as the KDE method in that it uses a trained set (a model, using all the photometric data and their uncertainties).

The likelihood of an object being a quasar, given its photometric data and errors is the sum of the distance to all the quasars and stars in the trained set in colour-colour space.

(iii) **The artificial neural network method** (Yèche et al. [2010]) like the other methods uses a trained set and computes the probability of an object, given all the photometric magnitudes and their uncertainties, is a quasar in the desired redshift ($2.15 < z < 3.5$) using four neurons.

(iv) **The Extreme Deconvolution** (XD; Bovy et al. [2011a], Bovy et al. [2011b]) method is a variation of the Likelihood method that properly accounts for the errors in the magnitudes. XDQSO is an application of XD method to assign a probability of an object being a quasar.

BOSS quasars are divided into several sets; CORE, BONUS, KNOWN, and FIRST with each set having different imaging cuts and flux limits. The cuts and limits were applied to single epoch data except for FIRST targets were co-added, multi-epoch data were used if available (Ross et al. [2012]). Objects with a FIRST flag are thus generally not in the CORE sample.

(i) The **CORE** quasars are uniformly selected across the BOSS footprint. From the second year to the end of the survey the CORE quasars were identified using the XDQSO target selection method (Bovy et al. [2011b]). During year one, a test year, the KDE selection method (Richards et al. [2004], Richards et al. [2009b]) was used to identify CORE quasars.

(ii) **BONUS** quasars are selected to maximize the surface density in such that the survey requirements of $20 \geq$ quasars per $\text{deg}^{-2}$ are met. These were selected using a combination of all the target selection methods (KDE Richards et al. [2004], Richards et al. [2009b]; likelihood method: Kirkpatrick et al. [2011], neural network, and the XDQSO method (Bovy-2011a) with lower likelihood than in the CORE sample) as well as additional data if needed.

(iii) Objects that have $g \leq 22$ or $r \leq 21.85$ with **FIRST** (Becker et al. [1995]) a match within $1''$ are considered as targets. A additional cut $(u - g) > 0.4$ is applied to exclude low redshift quasars.

(iv) **Known** quasars with $z > 2.15$ found in existing catalogues such as DR7 (Schneider et al. [2010]); the 2dF quasar redshift survey (2QZ; Croom et al. [2004]; the 2dF-SDSS LRG, quasar survey (2SLAQ; Croom et al. [2009])); the AAT-UKIDSS-DSS (AUS) survey, the MMT-BOSS pilot survey (Fabricant et al. [2005]) and quasars observed by VLT and KECK, that fall within $1.5''$ of a point source are considered targets. These are then re-observed to take advantage of the upgraded SDSS spectrograph (Ross et al. [2012]).

### 2.1.6   Spectroscopy

All the targets from the various selection methods are spectroscopically observed with the BOSS spectrograph. The spectrograph has a metal plate with holes were fibre-optic cables are attached and
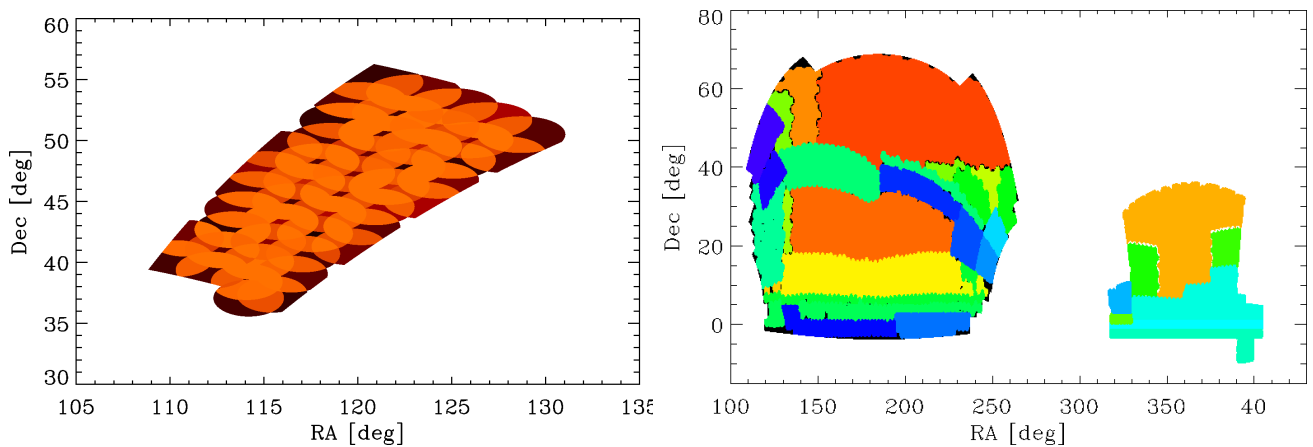
FIGURE 2.5: The left panel shows the geometry of a chunk that contains 47 plates and covers 144 deg$^2$ . The right panel shows the different chunks (each with its own colour coding) that make up the full BOSS footprint Ross et al. [2012]

.

light from a target enters the fibres and are directed to a grism or grating which splits the light to get the spectrum. The holes are distributed such that to maximize the number of the targets observed this is called tilling (the full details of SDSS tiling are found in Blanton et al. [2003]). Due to nature of large-scale and galactic structure, the targets have an inhomogeneous angular density distribution in the sky. Therefore, tilling completeness would mean a non-uniform distribution of the fibre holes. BOSS has a tiling completeness of 93%, this is due to the unobservable regions called masked regions [1]. The are four types of masked regions, bright star mask, central mask, bad field mask and collision priority mask (White et al. [2011]).

(i) **Bright star mask**

This is the mask that blocks regions around bright stars. The size of the mask depends on the apparent brightness and angular diameter of the star.

(ii) **Central mask**

The central part of all the plate has a hole for centerpost as a result, targets within a $92''$ radius of the central position are removed from the target list.

(iii) **Bad field mask**

This placed over regions that have bad photometric data.

(iv) **Collision priority mask**

Two holes in the plate cannot be closer than $62''$ in BOSS, this is because fibre optics can not be placed so close to each other and this is known as fibre collision. Collision priority mask is placed around objects that have high priority, so any object that lies within $62''$ is removed from

---

[1] `www.sdss3.org/dr9/algorithms/boss_tiling.php|`

the target list.

The survey is divided into several tilling chunk. A chunk is a set of tiles (might be from a different plate) covering a spatially continuous area observed at the same time and with the same target selection method. Fig 2.5a shows the geometry of a chunk within the survey which contains 47 plates and covers 144 square degrees. Fig 2.5b shows the chunks that make up the BOSS survey. Up to 1000 objects can be observed on each plate, with at least three 15 minute exposures or until the required signal to noise is achieved (Pâris et al. [2014]).

The geometry of the tilling of BOSS data is expressed in the form of spherical polygons created using the software package Mangle[2] (Swanson et al. [2008]). The whole survey is made up of 32,561 polygons of different sizes, to minimize the number of polygons used and to accurately follow the observed regions and avoid the masked regions.

### 2.1.7   Quasar catalogue

All the spectra of the quasars are visually inspected to ensure that the objects are indeed quasars. Further more identify features in the spectra to confirm or if needed correct the redshift provided by the pipeline (e.g in case a line is misidentified) (Paris et al. [2012]). About 300,000 (297,301) BOSS quasars were spectroscopically identified and released in the twelfth data release (DR12) quasar catalogue of the SDSS III(Pâris et al. 2015 in prep).

## 2.2   Sample

A magnitude limited survey may suffer from various selection effects, for example, Malmquist bias (see Hendry and Simmons [1990]) whereby luminous sources are detected at all redshifts whereas the less luminous sources at high redshifts are not detected. Our quasar sample is taken from the SDSS which has an apparent magnitude limit of $r \approx 22.5$ (Dawson et al. [2013]), therefore suffers from the bias. Statistical measurements such as source counts and luminosity functions require uniform and complete data or data that is corrected for biases. I select two samples from the SDSS quasar catalogue to study sources above the FIRST noise (Chapter 3) and a third sample to study sources below FIRST's detection threshold (Chapter 4). Sample 1 and sample 2 were chosen purely so that the results (source counts and luminosity functions) can be compared with literature (Condon et al. [2013], Kimball et al. [2011a]).

---

[2]`http://space.mit.edu/ molly/mangle/|`

### 2.2.1   Sample 1: Volume-limited sample

The first sample considered is a volume-limited sample. This is a sample where all the sources have an intrinsic brightness above a set minimum. The minimum brightness is chosen such that all the sources that meet these criteria are observed. The sample is chosen in the range $0.2 < z < 0.45$ and define the volume limit by $M_i < -23$. Only 162 BOSS quasars fell in the volume-limited sample. I ran into a problem using BOSS data at these redshifts (because BOSS focused on high redshift quasars, see 2.2.3), so I used SDSS II quasar sample which has 1,313 sources in the redshift range and applied the absolute magnitude limit.

### 2.2.2   Sample 2: Magnitude-limited sample

The second sample is a magnitude-limited sample. This is a sample where sources have apparent magnitudes above a set value. This kind of sample suffers from Malmquist bias as the sources at different redshifts have different brightness limit. I chose a magnitude limited sample from the redshift range $1.8 < z < 2.5$, favoured in optical quasar samples (e.g Condon et al. [2013]; Miller et al. [1990]) because the Ly$\alpha$ line is redshifted into the blue band. The magnitude limited sample is defined by $m_r < 18$, from the 11,613 (29.37%) quasars in this redshift range only 2,419 have the required magnitudes.

### 2.2.3   Sample 3: Uniform sample

The third sample is a uniform selection of sources across the survey area (CORE sample). The sample was initially taken solely from BOSS. However, BOSS quasars are not uniformly selected in redshift as it focused on high redshift(and ignored the known low redshift quasars Dawson et al. [2013]).Fig. 2.2's bottom panel shows the redshift distribution of these (BOSS) quasars. The redshift distribution has two peaks, one at $z \approx 2.2$ and another at $z \approx 0.8$ (Fig 2.2). The quasars around $z = 0.8$ have the same colours as targeted high redshift quasars (Fig 2.4) and the peak around $z = 2.2$ is a really one showing the underlying distribution of quasars .

The third sample is a combination of Legacy and BOSS. The low redshift part of the sample $z < 2.15$ is from SDSS II's Legacy quasar catalogue (Shen et al. [2011]) which has an absolute magnitude limit $M_i < -22$. Legacy observations from the first data release (DR1) are excluded from the uniform sample because they were selected using a different algorithm (Shen et al. [2011]). The higher redshift $z > 2.15$ sources are from BOSS's uniform sample defined by Ross et al. [2012], which includes quasars that have the UNIFORM flag equal one (CORE sample for year 2 onwards) or equal two (CORE sample from year 1). I also apply Legacy's absolute magnitude cut to the BOSS data so that the whole sample has the same brightness cut. The uniform BOSS sample contains around 122,000
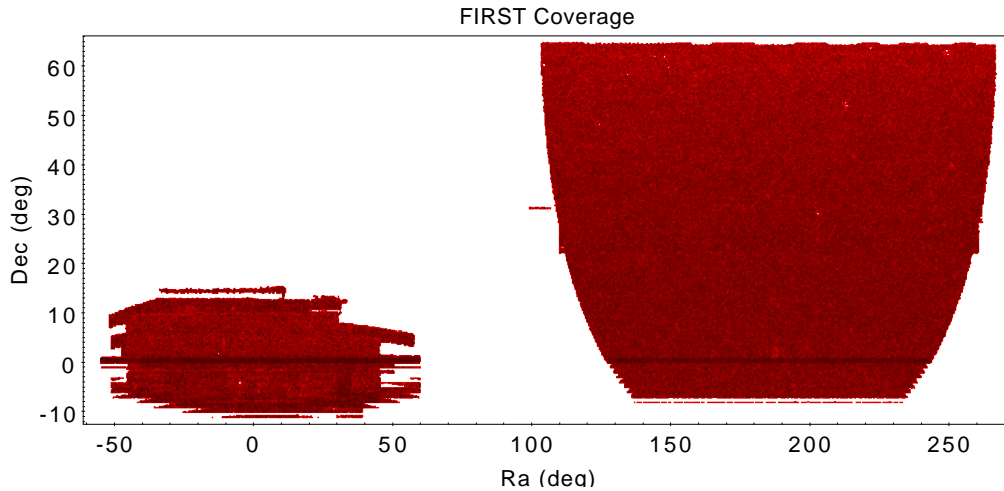
FIGURE 2.6: The full 10,575 deg$^2$ footprint of the FIRST maps, divided in two 8,444 deg$^2$ in the North Galactic Cap (NGC, on the right) and 2,131 deg$^2$ in the South Galactic cap (SGC). The SGG has rages (holes in the data) due to bad weather and faulty instruments.

sources and the Legacy uniform sample contains around 48,000 sources. Fig. 2.8 shows the footprint of the uniform samples.

### 2.2.4   Completeness

When conducting a survey, one aims to observe all the sources in footprint, however due to certain obstacles, it is not possible. Completeness is a measure of how close the observed sources are to the 'true' distribution of the sources (Johnston [2011]). For statistical measurements like source counts and luminosity functions, it is essential to know how many objects are missing. Accurately measuring the completeness is not easy because there are many obstacles to account for. I will divide the sources of incompleteness into two, instrumental obstacles and astronomical obstacles.

(i) **Instrumental incompleteness**

This is when objects are missed due to technicalities or limitations of the instruments used. This includes sources that missed because they lie in any of the masked regions (Section 2.1.6). This source of incompleteness can accounted for by computing the ratio of the sources observed and the target list.

(ii) **Astronomical incompleteness**

This is when objects are missed because of misclassification or high extinct(McGreer et al. [2009]) or observational biases such as Malmquist bias (Section 2.2). It is not trivial to find objects that are misclassified or those that suffer heavy extinction. I correct for Malmquist bias by using volume-limited data.
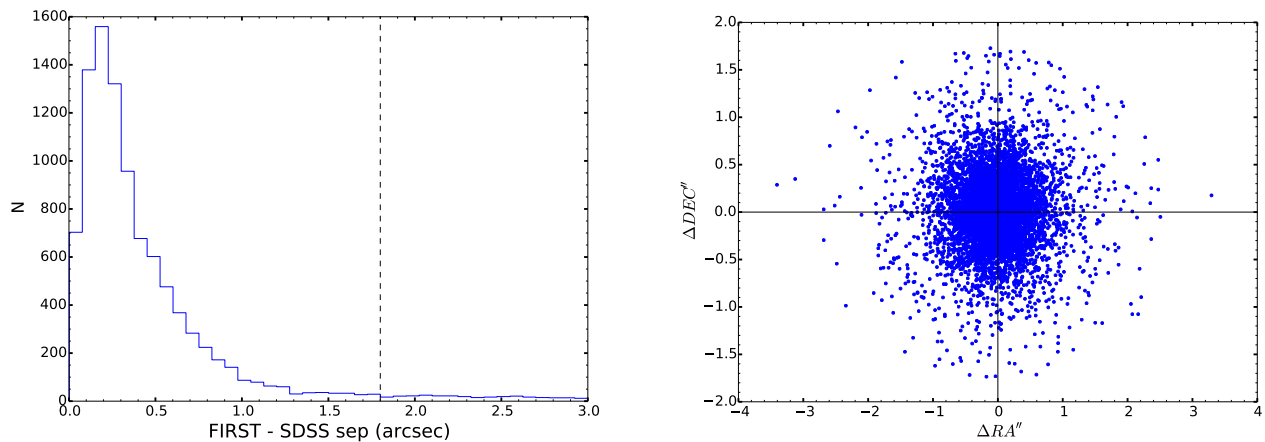
FIGURE 2.7: The left panel shows the distribution of the separation between FIRST and SDSS quasar positions. The vertical dashed line is the cut-off separation between FIRST and SDSS detected sources used in this work. The right panel shows the 2-D scatter of the difference in Right Ascension and Declination between SDSS and FIRST positions.

## 2.3   FIRST

The Faint Images of the Radio Sky at Twenty centimeters (FIRST) survey (Becker et al. [1995]) is a high angular resolution survey carried out with the Very large Array (VLA) telescope in its B-configuration at 20 cm (1.4 GHz, L-band). The survey was designed to match the 10,000 deg$^2$ survey area that the SDSS (York et al. [2000]) has covered. Observations started in 1993 and where completed in 2004, additional observations were made in SGC from 2009 to 2011 [3] to observe the ragged portions that were missed due to bad weather or faulty instrumentation. The survey covered a total coverage of 10 575 deg$^2$ with 8 444 deg$^2$ in NGC and 2,131 deg$^2$ in the SGC shown in Fig 2.6. The data is obtained by integrating for 3 min over a pointing on the sky in 7 pair frequency channels centered at 1365 and 1435 MHz. The pointings are designed to produce a uniform sensitivity over the whole survey footprint when all the pointings are co-added (Becker et al. [1995]). Each pointing is reduced (calibrated, self-calibrated, mapped and CLEANed) using an automated AIPS script. The final FIRST maps (Fig 2.6) are obtained by co-adding the individually reduced (weighted) pointings next to each other and stored in binary format as FITS images with $1.8''$ per pixels having a mean rms of about $150\mu$Jy/beam and a $5''$ resolution (White et al. [1997]).

Sources are identified from the co-added map using HAPPY, a AIPS script (full details are in White et al. [1997]). In brief, HAPPY identifies pixels above a set threshold, appropriately grouping them into 'islands' and fitting a two-dimensional Gaussian to each island. Basic properties like peak flux densities, integrated flux densities, right ascension and declination are obtained from this fit. Islands with fitted peak fluxes below $750\mu$Jy are removed, the remaining islands are classified and corrected

---

[3]http://sundog.stsci.edu/first/obsstatus.html

for the CLEAN bias (White et al. [2007],Condon et al. [1994]) explained in Section 2.5.1.

The survey catalogue contains more than 946,000 sources, over the 10,575 deg$^2$ sky coverage. All sources are above the detection limit, 1 mJy, with an exception of a region in the equatorial strip which contains data from two epochs. As a result, the detection limit is 750$\mu$Jy, there are $\approx$ 4,500 sources in this region were the flux densities are below 1 mJy. The catalogue sources have positional accuracies $\leq 1''$ (White et al. [1997]).

## 2.4 Matching SDSS with FIRST

### 2.4.1 Catalogue sources

I am interested in the radio luminosity function of optically selected quasars so I match the SDSS quasars to the FIRST catalogue. A quasar has a match when an object in the FIRST catalogue is found within a certain separation of the SDSS positions. The separation should be as small as possible to avoid random matching with other sources in the FIRST catalogue and it should also be large enough to ensure real matches are not omitted because of slight mismatches in position between the optical and radio data. Fig 2.7 shows the results of the matched sources, the right panel is the distribution of the separation between the matched SDSS and FIRST quasar catalogue positions. The right panel shows the 2-D scatter of the difference in Right Ascension and Declination between SDSS and FIRST positions. The difference in Right Ascension shows a larger scatter compared to the difference in Dec of the sources, this may suggest that the Right Ascension in one or both catalogues is less accurate than the Declination. Fig 2.7 suggest a systematic offset on the euclidean separation between FIRST and SDSS catalogues as the peak separation is at $0.2''$. I choose a limiting separation of $1.8''$ based on the right panel of Fig 2.7. From the 295,305 quasars, 9,253 (3.13%) matches were found within the limiting separation, $1.8''$; this is consistent with the low number of optical to radio matches (SDSS to FIRST; Paris et al. [2012]) found.

### 2.4.2 FIRST cutouts

In the previous section, I matched SDSS quasars to FIRST catalogue sources. However, the catalogue only has sources above the 1 mJy detection limit, which is about 0.02% of the FIRST data (White et al. [2007]) and 3% of the SDSS quasars. Ultimately I am interested in pushing the quasar RLF below the FIRST detection limit to the $\mu$Jy levels. To do this, I extract a 10-pixel cutout around the SDSS positions From the FIRST maps.
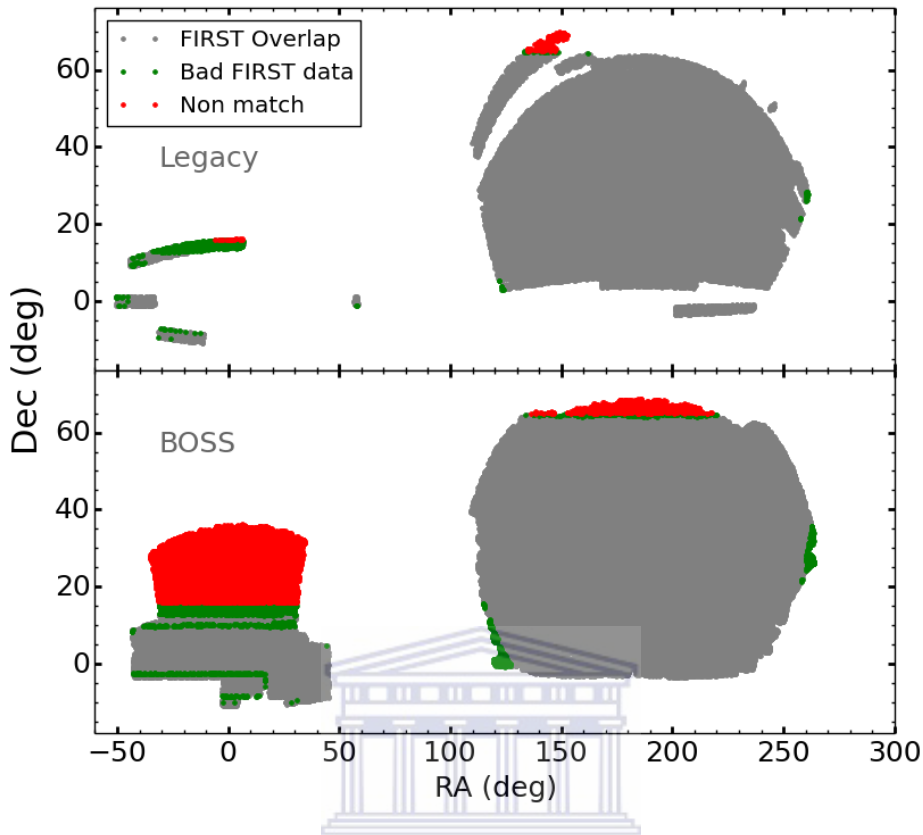
FIGURE 2.8: The survey footprint of BOSS and Legacy. The area is divided into three regions grey, green and red. The grey region is the part of the sample that falls within the FIRST footprint. The green region is the part of the sample that falls within the FIRST footprint but has zero fluxes and the red region is the part of the sample that does not fall within FIRST.

265,446 of the BOSS and 101,748 Legacy quasars fall within the FIRST area with a non-zero radio flux (i.e. the data in the region is not corrupted or missing). These sources are represented by the grey region in Fig. 2.8. The quasars in the red region either fall in a region where FIRST has not observed or were observed in bad weather conditions such that the data is corrupted. The quasars in the blue region have zero flux values due to bad data.

## 2.5   Catalogue and extracted fluxes

The extracted flux density of each quasar is the value of the central pixel of each cutout. The FIRST cutouts contain sources that are detected and sources where there is just noise. It is then important to investigate the difference between the catalogue and extracted fluxes of the detected sources and extrapolate the factors to the sources below the detection threshold that will be used for stacking. The left top panel of Fig 2.9 is the log-log plot of the peak catalogue fluxes versus the extracted flux. There seems to be a lot of scattering below 10 mJy were the extracted fluxes fall above and below

however most of the extracted fluxes fall below the peak fluxes. Above 10 mJy most of the extracted fluxes are less than the peak fluxes, very few are equal to and even fewer are greater than the peak fluxes. The button left panel shows the fractional difference between the extracted and peak fluxes given by,

$$\mathrm{frac}_D = 100 \times \frac{S_X - S_P}{S_P}, \tag{2.1}$$

where $\mathrm{frac}_D$ is the fractional difference, $S_X$ is the extracted flux and $S_P$ is the peak flux. There is clearly a significant difference between the extracted fluxes and peak fluxes ($\approx 20\%$) which will have an effect on the results and, therefore, needs to be accounted for or understood. The are two effects considered, the snapshot bias and extraction position.

### 2.5.1   Snapshot bias

The snapshot bias is an effect that decreases the peak flux densities of detected sources and redistributes it around the field. This phenomenon affects large area radio surveys such as FIRST and NVSS and it is associated with the non-linear CLEAN process (Condon et al. [1994]). The bias is additive and generally constant but the magnitude of the bias depends on (i) the rms of the snapshot (the magnitude increases with noise), (ii) the position with respect to primary beam pattern and (iii) the size of the source (extended sources are affected more) (Condon et al. [1998], Becker et al. [1995]). Furthermore White et al. [2007] discovered that the bias affects sub-threshold sources (which are not CLEANed), suggesting it is associated with the side-lobes of the beam pattern. However, this bias behaves differently from the one associated with CLEAN algorithm as it is multiplicative (the higher the flux the higher the bias). White et al. [2007]'s correction to the snapshot bias (which works for both flavours) is given by

$$S_X = \min(1.40 S_X, S_X + 0.25 \mathrm{mJy}), \tag{2.2}$$

where $S_X$ is the extracted flux. The correction was applied to the extracted fluxes and the right panel of Fig 2.9 shows the results. This correction has a significant effect on the low flux sources and little effect on the high-flux sources. The correction is used for all our extracted data from here on.

### 2.5.2   Extraction position

The extracted flux densities are from the central pixel of the 10 by 10 FIRST cutout which is centred on the optical position. If the source is not directly at the centre of the cutout, the extracted flux is lower than the detected flux density. The difference in optical and radio positions might be due to the difference the source of radio and optical emission in galaxies. However, because the sources are so far way, this difference is negligible so can not be the source of the difference in radio and optical positions. This difference must be due to astrometry errors between the two surveys.

(A) Extracted fluxes.

(B) bias-corrected fluxes.



(C) Extracted fluxes.

(D) bias-corrected fluxes.
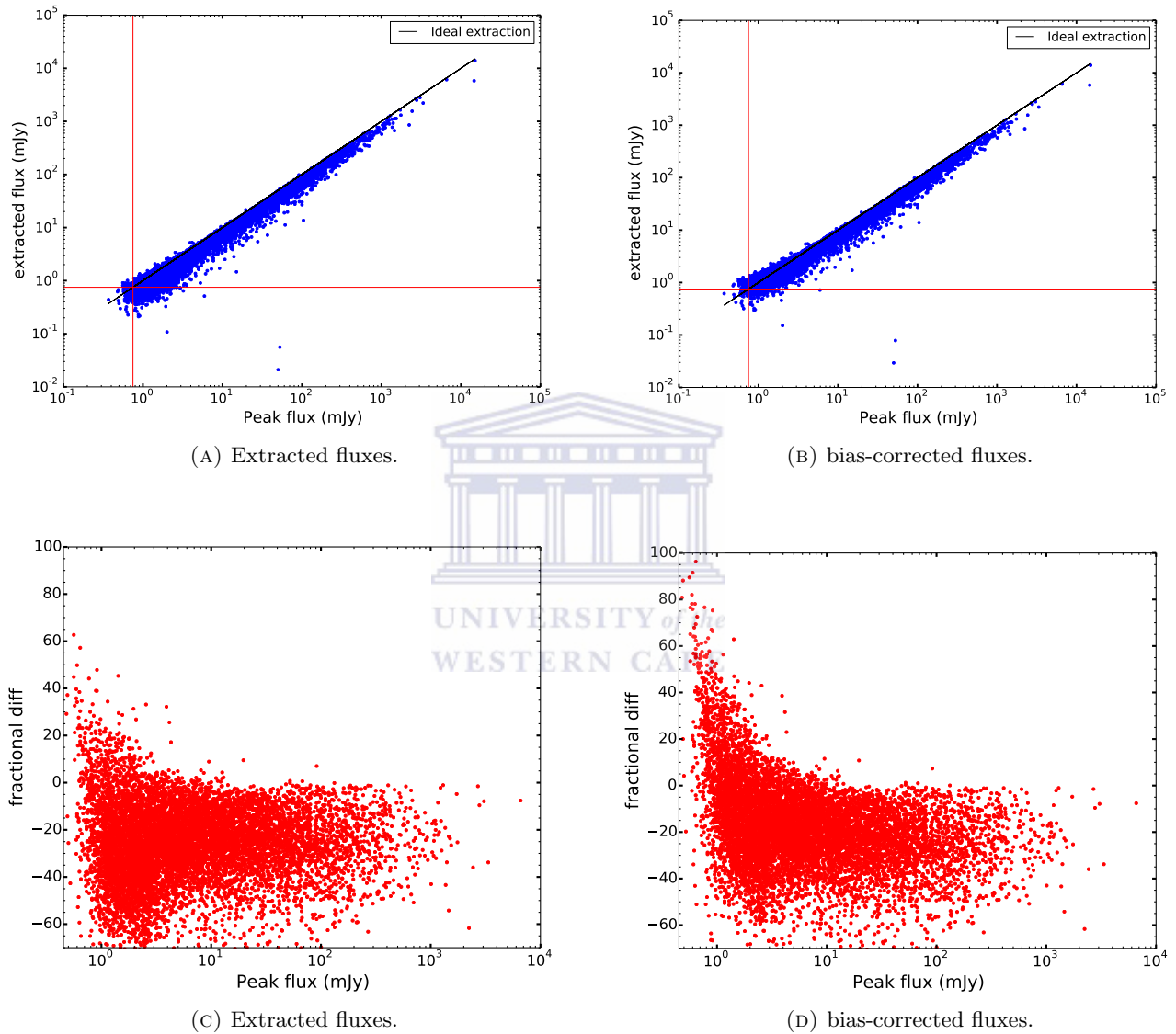
FIGURE 2.9: The difference between FIRST extracted and catalogue fluxes. The top panels is the plots of the catalogue fluxes versus the extracted fluxes, the solid line represents a case where the extracted flux is equal to the catalogue flux and the red lines are the $5\sigma$. The bottom panels show the fractional difference between the extracted and peak fluxes, described by Eq 2.1. The right panels are corrected for snapshot bias.

## 2.6    Sample area

Measuring statistical quantities such as source counts and luminosity functions (LFs) one needs to take into account the sky area in which the sources were observed. Computing this area is not as straightforward as one might think as one cannot simply take the total survey areas of BOSS or Legacy. The area that is required is the overlap between optical and radio surveys shown in Fig 2.8, bottom panel for BOSS and middle panel for Legacy.

### 2.6.1    BOSS overlap

In calculating the overlapping region between BOSS and FIRST I consider the geometry of the BOSS described by different sizes of polygons (see Section 2.1.6). I extracted the central coordinates of each of the 32,561 polygons and checked whether it fell in the FIRST coverage. There was one of three situations:

 (i) The centre lies within the FIRST maps, then add the area subtended by the polygon to the overlap area. A possible problem arises, does size (of the polygon) matter? I address this below. These fall in the grey regions in Fig 2.8.

 (ii) The centre lies within the FIRST maps but the flux is zero. The situation arises when the are no observations in the field but due to the (rectangular) shape of the fits file this region is included or the data is corrupted from bad observing conditions or instrument failure. These fall in the green regions in Fig 2.8.

 (iii) The last scenario is when the centre does not lie within the FIRST maps. This is when the area was not observed by FIRST and falls in the red regions in Fig 2.8. The results are shown in Fig.5 and Table 2.1.

The major flaw of this method is when the size of a polygon is bigger than a $1.8''$ FIRST pixel. This would mean that there will be an overestimate the area when only a part of the polygon is in FIRST maps (with the centre included) and under-estimate when again a part of the polygon is in FIRST but the centre is not. The polygons are designed to accurately follow the SDSS footprint, so errors are only found in FIRST.

The polygons size ranges from $3.28 \times 10^{-12}$ deg$^2$ to 4.11 deg$^2$ and with a median of 0.128 deg$^2$. The FIRST maps have size $1.8''$ per pixel which corresponds to an area of $2.5 \times 10^{-7}$. More than half of the polygons are bigger than the area of a FIRST map pixel

|            | BOSS deg$^2$ | Legacy deg$^2$ |
|------------|--------------|----------------|
| Total      | 10269.00     | 6672.0         |
| Overlap    | 8609.67      | 6558.0         |
| Zero flux  | 304.58       | 90.0           |
| No-matched | 1354.75      | 24.0           |

TABLE 2.1: A summary of the overlap between the two optical samples from BOSS and Legacy surveys and FIRST maps. Zero flux is the regions of the FIRST maps were no observations were made and the No-matched is the regions that FIRST does not cover.

### 2.6.2   Legacy overlap

The overlapping area covered by the Legacy is a bigger challenge because unlike with BOSS, polygons describing the geometry are not provided. Legacy only provided coordinates of the spectroscopic plates which project a $\approx 7$ deg$^2$ on the sky and unlike polygons, plates overlap with each other. The overlap area is estimated by using a flat sky approximation with 1 deg$^2$ pixels. Then the area is estimated by summing the unique area covered by the projection of the plates that fall in FIRST maps. This method has a lot more uncertainties because the size of the projections is larger than a FIRST pixel. The overlap area between FIRST and Legacy is 6,391.0 deg$^2$; the results are shown in Table 2.1.

# Chapter 3

# Above the detection threshold: Radio-loud quasars

Before I dive below the detection threshold ($\approx 1$ mJy), I investigate methods of computing radio source counts and luminosity functions for optically selected quasars detected in FIRST. I will do this for the two samples described in Section 2.2, the volume-limited and magnitude samples, and compare my results to the literature.
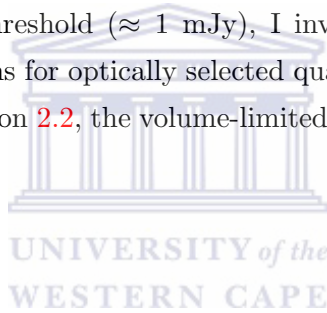
## 3.1    Source counts

The simplest and most fundamental experiment one can undertake with objects from a survey is to count their number as a function of flux. Source counts became popular in astronomy when Ryle [1955] and Ryle and Scheuer [1955] found that the 2C survey counts were surprisingly steeper than those of a static uniformly filled Euclidean universe and suggested the radio stars were extragalactic. Longair [1966] then showed the steepening of the counts can be explained by differential cosmic evolution of sources and since then source counts have been used to study extragalactic populations and galaxy evolution (e.g. Rowan-Robinson [1970]; Whittam et al. [2013]).

Source counts are usually presented in differential form $n(S)dS$, defined as the number of objects per steradian with flux density $S$ between $S$ and $S + dS$. The integral form of the source counts is defined as the number of sources brighter than flux density $S$. The integral form is however not favoured as it smoothes out rapid changes of source density with flux density, furthermore, the numbers in each flux density bin are not statistically independent (Jauncey [1967], Crawford et al. [1970]). Even on a logarithmic scale, source counts can be so steep that most of the interesting features are obscured.

33

Weights are introduced to normalize the source counts; I consider two weighting schemes used in radio studies, brightness-weighted and Euclidean-weighted.

(i) **Brightness-weighted counts**

The radio source counts are related to the sky brightness by the Rayleigh-Jeans' long-wavelength approximation,

$$n(S)dS = \frac{2k_B dT_b \nu^2}{c^2}, \tag{3.1}$$

where $k_B$ is the Boltzmann constant, $dT_b$ is the brightness temperature from $n(S)$ sources between $S$ and $S + dS$, $c$ is the speed of light and $\nu$ is the observed frequency. Knowing that the fluxes span a few orders of magnitude one can substitute $d\log_{10}(S) = dS/S$ and change bases to give

$$\left[\frac{dT_b}{d\log_{10}(S)}\right] = \left[\frac{\ln(10)c^2}{2k_B \nu^2}\right] S^2 n(S). \tag{3.2}$$

The brightness-weighted counts are thus proportional to the brightness temperature in each logarithmic flux range (Condon [1988]).

(ii) **Euclidean-weighted counts**

The Euclidean weights are obtained by assuming a Euclidean universe (i.e a static uniformly-filled universe). For sources with luminosities $L$ in the range L + $LdL$ with a luminosity function $\rho(L)$ (3.8). The observed flux $S$ at distance $R$ from the source is given by

$$S = \frac{L}{4\pi R^2}. \tag{3.3}$$

Then $R_{\max}$, the maximum radius at which an object with luminosity $L$ will have flux $> S$, is

$$R = \left(\frac{L}{4\pi S}\right)^{1/2} \quad \Rightarrow dR = -\frac{L^{3/2}}{(4\pi)^{3/2} S^{5/2}} dS. \tag{3.4}$$

The number of sources with luminosity $L$ that have fluxes $> S$ in a shell $R$ to $R + dR$ is,

$$\begin{aligned} N(S) &= \rho(L)dV(R) \\ &= \rho(L)4\pi R^2 dR \\ &= -\rho(L)L^{3/2}(4\pi)^{-1/2} S^{-5/2} dS. \\ \Rightarrow n(S)S^{5/2} &= -\rho(L)L^{3/2}(4\pi)^{-1/2} \end{aligned} \tag{3.5}$$

The right side is constant because the $N(S)$ is independent of the luminosity function (e.g. Krolik [1999]). The differential source counts of objects normalized by $S^{5/2}$ are expected to be constant in a Euclidean universe, this was one of the earliest evidence of a non-static universe (e.g Ryle and Clarke [1961]). I adopt the Euclidean weighting in this work.

FIGURE 3.1: The Euclidean normalized source counts of the volume-limited sample defined by $M_i <$ $-23$ in the redshift range $0.2 < z < 0.45$ in the top panel and the button panel is of the magnitude-limited sample defined by $m_r < 18.5$ in the redshift range $1.8 < z < 2.5$. The blue dots are the BOSS source with FIRST catalogue matches, the red triangles are Condon et al. [2013]'s sample taken from Legacy with NVSS catalogue matches. The green squares are Legacy sources with FIRST counterparts and the purple diamonds are also Legacy-FIRST sources with the NVSS flux cut of 2.4 mJy. The red and blue dotted lines represent the NVSS and FIRST detection limits respectively.
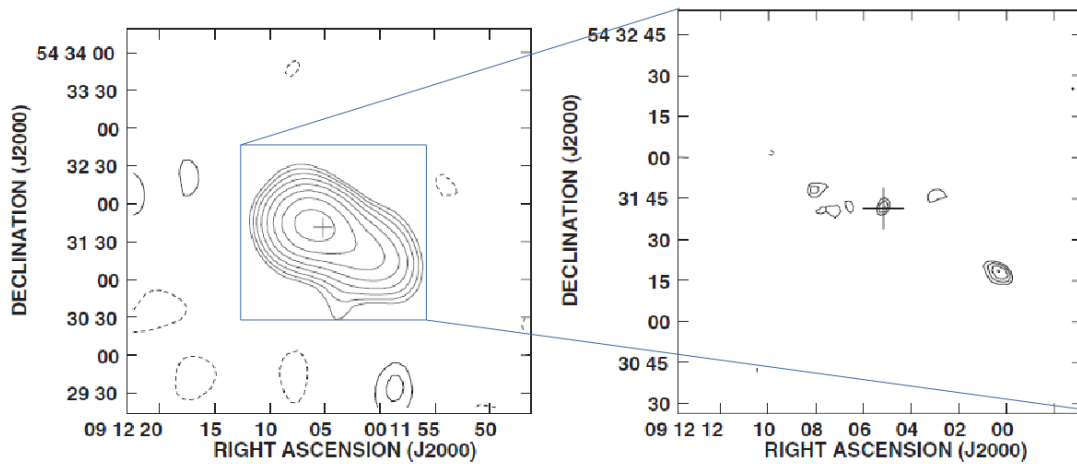
FIGURE 3.2: The 1.4GHz images of SDSS J091205.16+543141.2; the left panel shows the NVSS image and the right panel shows a higher resolution with lower surface brightness FIRST image. The contours have a $\pm\sqrt{2}$ separation with FIRST starting at 0.5 mJy beam$^{-1}$ and NVSS at 1 mJy beam$^{-1}$ (taken from Condon et al. [2013])
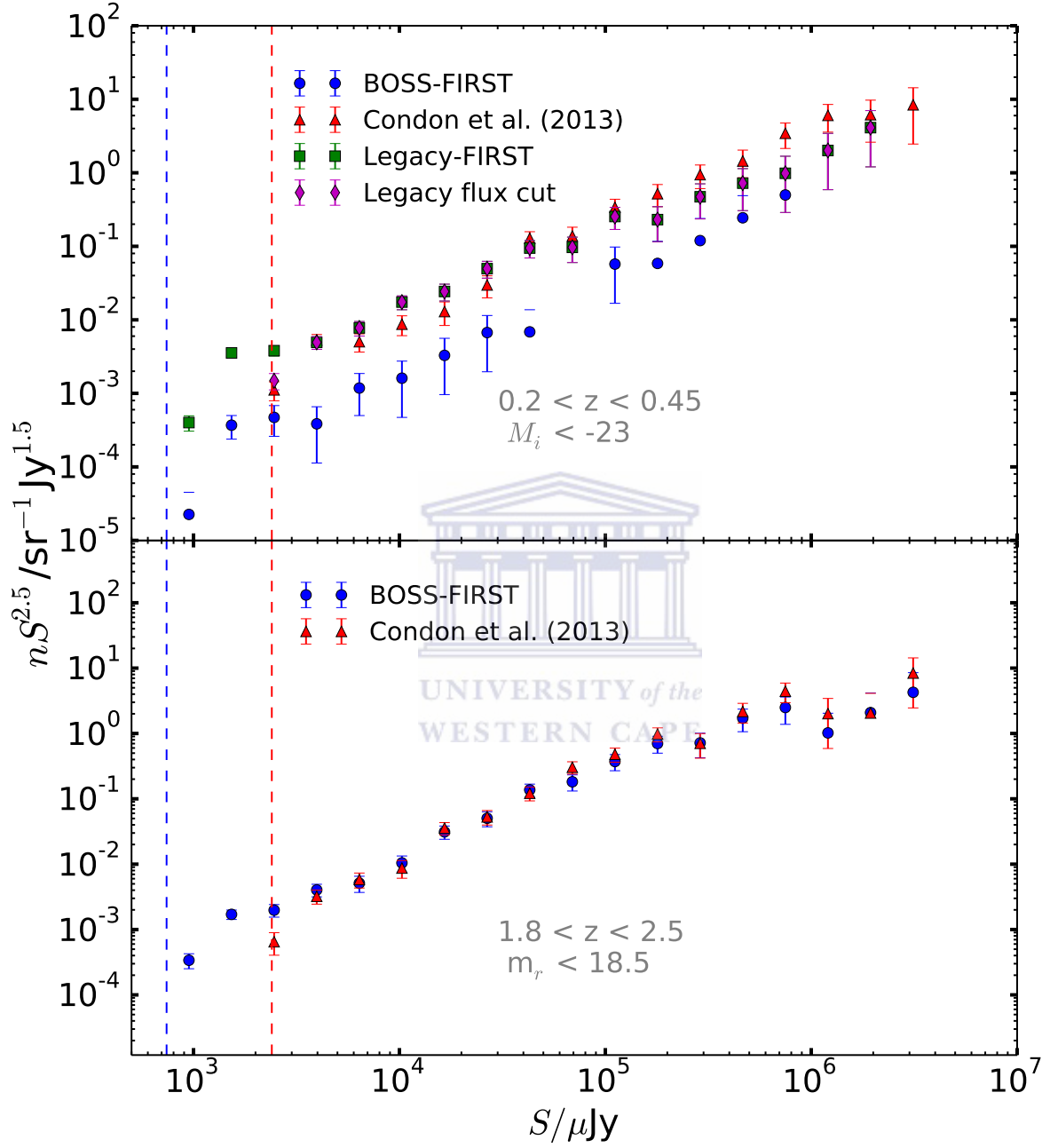
### 3.1.1 Sample 1

The top panel of Fig. 3.1 shows the quasar radio source counts of the volume-limited sample defined by $M_i < -23$ in the redshift range $0.2 < z < 0.45$ (2.2.1). The BOSS data points do not agree with Condon et al. [2013]'s sample (Legacy-NVSS); this is due to the fact that BOSS ignored all the known low-redshift quasars identified by Legacy (and other low redshift quasar surveys) and observed new ones from the area not observed by Legacy (2.1.5). There are 282 quasars in the Legacy and FIRST catalogues with fluxes ranging from 0.95 mJy to 2,260 mJy. The data (Legacy-FIRST) are consistent with Condon's (Legacy-NVSS) data as shown in the top panel of Fig. 3.1. Although FIRST counts are mostly below the NVSS fluxes and at the faint FIRST data points lie above those of Condon et al.. This is because when using extended baselines in the VLA like you do for FIRST you miss the extended emission, and, therefore, would underestimate the amount of radio emission. This would move objects to fainter radio fluxes than they actually are. Also, some will disappear from the FIRST survey altogether as they do not have a peak flux above the rms that means that they are detected at $> 5\sigma$. This would decrease the source counts as you get closer to the flux limit ($5\sigma$). However, when using smaller baselines like in NVSS you miss very little extended emission, but the flux-limit is higher (2.5 mJy), therefore you don't get as deep as you do with FIRST (1 mJy). Even with a $5\sigma$ detection threshold you still probably only detect $\approx 80\%$ of the objects in both surveys. Fig. 3.2 illustrates the difference between FIRST and NVSS with a multicomponent quasar, FIRST resolved the core and the two lobes with flux densities that add up to 6.6 mJy while NVSS resolved it as a single object with a flux density of 23.8 mJy (Condon et al. [2013]). This shows how FIRST and NVSS complement each other.

### 3.1.2 Sample 2

The Euclidean weighted source counts for the magnitude-limited sample is shown in the bottom panel of Fig. 3.1. There are 233 detected sources in both BOSS and FIRST that satisfy this sample definition. I obtained the source counts in Fig. 3.1 by: (i) selecting all the sources in the redshift slice, (ii) bin the fluxes (I used the same bins as Condon et al.), (iii) and normalize the counts in each bin by $S_{\mathrm{med}}^{2.5}$ (Euclidean normalization), where $S_{\mathrm{med}}$ is the median flux of the bin. The results are consistent with Condon et al.'s Legacy and NVSS results with the same issue at the low flux end as the volume-limited sample (see 3.1.1) that FIRST has more data because it has a lower detection limit. The FIRST data points are mostly below the NVSS points.

## 3.2 Radio luminosity function

Source counts contain rich information about source populations and their evolution. When combined with redshift information they can be used to infer star-formation rates (e.g. Dunne et al. [2009], Karim et al. [2011], Zwart et al. [2014]) and construct luminosity functions (LFs; e.g. Condon et al. [2013]; Roseboom and Best [2014]).

A LF is the distribution of objects luminosities weighted by the comoving volume they are observed in. LFs therefore, encompass more information than counts as the luminosity is an intrinsic property of the source. It is hard to get the Bolometric luminosity of objects as this requires integrating contributions over all frequencies. I instead work with the spectral luminosity function which is the LF defined at a certain frequency (or bandwidth).

Construction of the LF requires the luminosities of the sources at given 1.4 GHz FIRST flux densities, plus their SDSS redshifts. The spectral luminosity $L_\nu$, at frequency $\nu$ in the source frame, for an isotropic source at redshift $z$ is given by

$$L_\nu = 4\pi D^2 (1+z)^{1-\alpha} S_\nu, \tag{3.6}$$

where $S_\nu$ is the spectral flux measured at frequency $\nu$ in the observer's frame, and $\alpha$ is the spectral index between two frequencies $\nu$ and $\nu_0$ in the observer's frame, defined as

$$\alpha \equiv -\ln(S/S_0)/\ln(\nu/\nu_0).$$

The $(1+z)^{1-\alpha}$ term corrects for the fact that the flux $S_0$ has been redshifted from $\nu$ to $\nu_0$. $4\pi D^2$ is the area of a sphere centred at the source with the observer at the circumference. $D$ is the effective

distance or comoving distance (Longair [1978]); for example in Friedman models (where cosmological the constant $\Lambda$ is zero) with zero pressure the comoving distance is given as (Mattig [1958])

$$D = \frac{2c[2 - \Omega_M(1 - z) - (2 - \Omega_M)\sqrt{1 + \Omega_M z}]}{H_0 \Omega_M^2 (1 + z),} \tag{3.7}$$

where $c$ is the speed of light, $\Omega_M$ is the mass density and $H_0$ the Hubble constant. The comoving distance is related to the luminosity distance, defined by $S = L/4\pi D_L^2$, as $D_L = D(1 + z)$.

The spectral LF, $\rho_m$, is (Condon [1984]):

$$\rho_m(L_\nu) = \ln(m)L_\nu\rho(L_\nu), \tag{3.8}$$

where $L_\nu\rho(L_\nu)dL_\nu$ is the comoving number density of sources with spectral luminosities between $L_\nu$ and $L_\nu + dL_\nu$ and $m \equiv 2.5$ (the definition of magnitude i.e. $\Delta m = 2.5 \log_{10}(S)$).

Completeness is one of the major issues one faces when constructing a LF from a flux-limited survey, such as SDSS. Such surveys are affected by Malmquist bias (Section 2.2) whereby brighter objects at higher redshifts and fainter objects at lower redshifts are favoured. Several weighting schemes for LFs were developed over the years to account for such biases, such as the classical approach (Felten [1977]), $C^-$ method (Lynden-Bell [1971]) (see Johnston [2011] for a review).

I use the $1/V_{\max}$ method (Trumpler and Weaver [1953]; Christensen [1975]; Schechter [1976]) to correct for this effect. For $N$ sources in a spectral luminosity bin of logarithmic width $m$, $\rho_m$ is given by

$$\rho_m(L_\nu) = \sum_{i=1}^{N} \left(\frac{1}{V_{max}}\right)_i, \tag{3.9}$$

where $V_{\max}$ (Mpc$^3$) is the comoving volume where the sources could have been detected. In simple terms, I obtain the LF by binning the luminosities (0.4 binwidths) and add the $V_{\max}$ of each source in the bin. The variance associated with $\rho_m(L_\nu)$ is given by,

$$\sigma^2 = \sum_{i=1}^{N} \left(\frac{1}{V_{max}}\right)_i^2. \tag{3.10}$$

Fig. 3.3 shows the quasar radio luminosity function (RLF) of the detected FIRST quasars from Legacy and FIRST catalogues in the redshift $0.2 < z < 0.45$ brighter than $M_i = -23$. This sample is volume-limited and, therefore, contains all the optically selected quasars in this survey area and redshift range. The quasars that are not in this list are those that are missed due to redshift completeness (Section 2.2.4). RLF are known to follow a (broken) power law (Boyle et al. [1988], 2000, Pei [1995]),
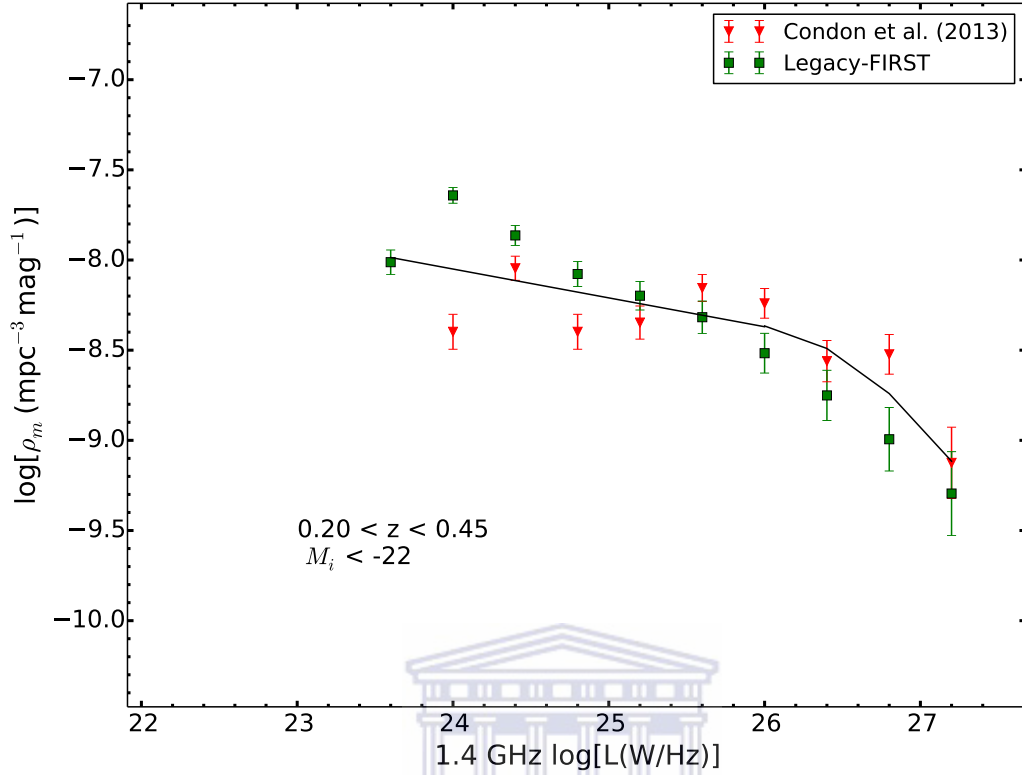
FIGURE 3.3: The 1.4 GHz luminosity function of the volume-limited sample $M_i < -23$ at $0.2 < z < 0.45$. The green squares are obtained from Legacy with matched FIRST fluxes and the red triangles are Condon et al. [2013]'s sample taken from Legacy with NVSS counterparts. The black line follows Eq. 3.11 and Eq. 3.12.

our RLF follows one from $L \approx 10^{26}$ to lower luminosities. Condon et al. [2013] and Kimball et al. [2011a] suggest a fall at around $L \approx 10^{20}$ WHz$^{-1}$, otherwise, the total number of radio sources will exceed the number of quasars. The power law is given by

$$\log_{10}\left(\frac{\rho_m}{\text{mpc}^{-3}\text{mag}^{-1}}\right) = -4.21 - 0.16\log_{10}\left(\frac{L}{1.4\text{GHz}}\right), \tag{3.11}$$

and starts to fall off at the higher luminosities ($\sim 10^{26}$) following an arbitrary quadratic,

$$\log_{10}\left(\frac{\rho_m}{\text{mpc}^{-3}\text{mag}^{-1}}\right) = \left[-8.35 - \log_{10}\left(\frac{L}{1.4GHz}\right) - 25.8/1.6\right]^2. \tag{3.12}$$

The fall-off at high luminosities is because there are no more observed quasars (in the SDSS) at these luminosities (Kimball et al. [2011a]).

Its well know that powerful emission from (radio loud) quasars is dominated by accretion of material into a black hole (Salpeter [1964]) and have luminosities above $\log_{10}(L) \approx 22.5$ (Kimball et al.
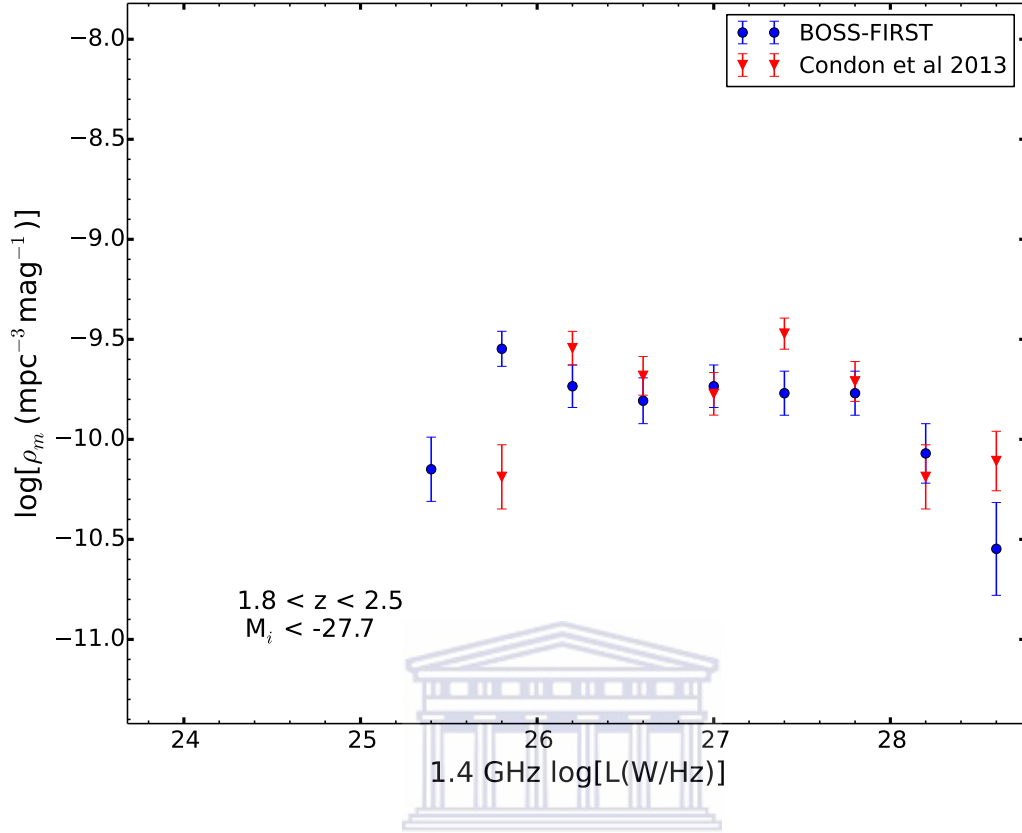
FIGURE 3.4: The 1.4 GHz radio luminosity function of quasars detected in FIRST from the magnitude-limited optical sample defined by $m_r < 18.5$ at $1.8 < z < 2.5$ with an additional absolute magnitude cut of $M_i < -27.7$. The blue dots are obtained from BOSS sources with FIRST matches and the red triangles are Condon et al. [2013]'s sample taken from Legacy with NVSS counterparts.

[2011a]). Radio-quiet quasars have lower luminosities and are believed to be dominantly powered by star-formation and AGN-related emission (Condon [1984], Windhorst et al. [1985], Kron [1985], Wall and Jackson [1997]). Both Kimball et al. [2011a] and Condon et al. [2013] found a bump in the LF peaked $\log_{10}(L/\text{WHz}^{-1}) \approx 22.5$ which deviates from the power-law in Eq. 3.11 for AGN dominated emission. They conclude that radio-quiet quasars are powered by star formation because they behave differently from radio-loud quasars which are known to be powered by AGN.

Fig. 3.4 shows the quasar RLF for the magnitude-limited sample $m_r < 18.5$ with redshifts $1.8 < z < 2.5$. The plot shows a comparison between our luminosity function (BOSS-FIRST) and Condon et al. [2013]'s Legacy-NVSS data. From the 2,419 quasars in the optical sample, 233 have detected FIRST counterparts within a $1.8''$ radius. The quasars have luminosities ranging from $1.43 \times 10^{25}$ to $4.58 \times 10^{28}$ WHz$^{-1}$. The results are consistent with each other except for the difference at the faint end (see Section 3.1.1).

# Chapter 4

# Below the detection threshold: stacking and radio-quiet quasars

The main aim of this thesis is to investigate the nature of the radio-quiet quasars, but they lie below the detection threshold of currently completed large-area radio surveys. In Chapter 3 I explored quasars above the FIRST detection threshold (1 mJy) in the two samples described in Section 2.2. Only radio-loud quasars have FIRST counterparts; currently the deepest large-area radio survey and they make up $\approx 10\%$ of the optically-selected quasars (e.g. Condon et al. [2013], White et al. [2007], Ivezić et al. [2002]). Moreover, 99.98% of the five billion FIRST beams are 'empty' sky (White et al. [2007]). This means that most of the quasar population and radio sources are below the detection threshold of 1 mJy.

This radio-quiet population below the detection threshold of wide-area surveys can be studied through smaller deeper radio surveys such as the First-Look survey (FLS; Condon et al. [2003]) and Cosmic Evolution Survey (COSMOS; Schinnerer et al. [2004]). FLS covers the same 5 deg$^2$ field as Spitzer's First-Look survey (Fadda et al. [2004]) using the VLA in its B-configuration, and reached a mean RMS of 23 $\mu$Jy. COSMOS is a collection of 7 VLA observations in A configuration with an RMS ranging from 36 to 46 $\mu$Jy. These small surveys have a few 100s to 1000s (mostly extragalactic) sources which make them excellent for studying galaxies. However, they have detected very few quasars: Using SDSS DR3 White et al. [2007] found ten counterparts from FLS and four from COSMOS. There recently have been a few deep surveys that have allowed the study of radio-quiet populations, for example, the VLA-Chandra Deep Field South (VLA-CDFS; Kellermann et al. [2008]) covering a 0.11 deg$^2$ area down to a rms of $\approx 8.5\mu$Jy (complemented by data from a variety of other frequencies).

Another way of studying radio-quiet quasars is by observing a selected sample (e.g. Kimball et al. [2011b]). However, this requires a great deal of telescope time. Hence, the most common means of studying sources below the detection threshold in the past decade (Ivezić et al. [2002], White et al.

[2007], Hodge et al. [2008], Mitchell-Wynne et al. [2014], Roseboom and Best [2014]), is to use some form of 'stacking'.

## 4.1  Stacking

There are a number of different versions and definitions of stacking seen in the literature (see Zwart et al. [2015a] for an overview). In its simplest form, stacking is using positional information of a source population selected (and classified) from an auxiliary survey and extracting the flux density in the survey of interest (where they are above or below the detection threshold; typically radio). In most cases stacking is used to explore the average properties of sources below the detection threshold, typically $3\sigma - 5\sigma$. For example, stacking to infer average SFR (e.g. Dunne et al. [2009]; Karim et al. [2011], Zwart et al. [2014]), where they extracted 1.4 GHz radio fluxes from positions of sources selected by stellar mass in the near infrared (taking advantage of the FIR-radio correlation, Section 1.2.5).

Average stacking techniques have added a great deal to our understanding of $\mu$Jy source populations. However, they only return a single statistic and lose all the other information. Mitchell-Wynne et al. [2014] developed a maximum-likelihood based stacking technique that returns a model of the source counts and Roseboom and Best [2014] adopted a similar approach to model the LF and its evolution. Zwart et al. [2015b] then extended Mitchell-Wynne et al.'s technique to a fully-Bayesian framework (Bayestack) that allows different source models to be fitted and compared.

I will stack all the SDSS quasars that are below the FIRST detection threshold using two approaches; simple average stacking and a full Bayestack approach where I follow the work of Zwart et al. [2015b]. Before I discuss the stacking methods, I will explain the main sample below the FIRST detection limit.

## 4.2  Sample 3: Uniform sample

I use sample 3, the uniformly selected optical quasar sample (Section 2.2.3). The low-redshift part of the sample ($z < 2.15$) is taken from Legacy and the higher redshift sample ($2.15 < z < 3.5$) from BOSS. I extracted the pixel fluxes from FIRST cutouts nearest to the optical position. I divided the sources into 12 redshift slices, kept as small as possible to avoid in-bin evolution, but making sure they are wide enough to have statistically sufficient data. Table 4.1 and Fig. 4.1a show the redshift slices, the number of objects in each slice and the median stacked fluxes. Fig. 4.2 shows the flux distributions of the sources overs the 12 redshift slices. The distributions are Gaussian on the negative side but have positive tails in the $\sigma - 5\sigma$ regime that contain the buried sources whose fluxes I will use to fit source count models after Zwart et al. [2015b]. There are negative fluxes because the interferometer

| z bin | N | Median flux ($\mu$Jy) | z bin | N | Median flux ($\mu$Jy) |
|---|---|---|---|---|---|
| $0.20 < z < 0.45$ | 4381 | $182 \pm 14$ | $1.85 < z < 2.15$ | 6319 | $84 \pm 14$ |
| $0.45 < z < 0.70$ | 5508 | $168 \pm 14$ | $2.15 < z < 2.35$ | 27256 | $34 \pm 4.2$ |
| $0.70 < z < 1.00$ | 6106 | $126 \pm 14$ | $2.35 < z < 2.55$ | 27088 | $35 \pm 4.2$ |
| $1.00 < z < 1.30$ | 8423 | $112 \pm 14$ | $2.55 < z < 2.85$ | 18613 | $39 \pm 4.2$ |
| $1.30 < z < 1.60$ | 9225 | $98 \pm 14$ | $2.85 < z < 3.15$ | 12744 | $35 \pm 4.2$ |
| $1.60 < z < 1.85$ | 7421 | $98 \pm 14$ | $3.15 < z < 3.50$ | 7775 | $39 \pm 5.6$ |

TABLE 4.1: The redshift slices used for sources below $5\sigma$. The lower redshifts ($z < 2.15$) are taken from Legacy and the higher redshifts are taken from BOSS.

does not measure the constant background of the sky, the mean background brightness is subtracted from noise-only/source free observations and rejected where there are sources.

## 4.3   Simple averaging

In this approach, I summarized each of the flux distributions (Fig. 4.2) with a single statistic, the average (mean or median) flux. White et al. [2007] fully explores the advantages the two statistics, the mean and median:

(i) The **mean** is straightforward to compute and can be easily interpreted. The problem with this average is that it is sensitive to outliers, i.e. a bright source will considerably shift the mean to the positive side.

(ii) The **median** value is a more robust statistic as it is less sensitive to outliers, however, it also has a number of biases including the shape of the population and the map noise (Bourne et al. [2012]). The problem with the median is interpreting it. At a low signal-to-noise; White et al. [2007]'s median stack approaches the mean, so they interpret their medians as means.

I use the median stack to obtain the average flux of each redshift slice (Table 4.1 and Fig. 4.1b). The median fluxes are all below the detection threshold and they decrease with redshift and decrease exponentially with increasing redshift (which is expected, White et al. [2007]) from 182 $\mu$Jy at $0.2 < z < 0.45$ to 39 $\mu$Jy at $3.15 < z < 3.5$. This decrease is due to the optical selection imposed on the sample. The flux decreases because galaxies are further away, and if radio emission is correlated with optical emission (which there is up to a point, see Serjeant et al. [1998]) then the higher radio fluxes are low from the fact that they are more distant (in spite the fact that they are intrinsically more luminous). There was a discontinuity between the median flux from Legacy and BOSS. This discontinuity is from the fact that BOSS reaches fainter apparent magnitudes within the $M_i = 22$ absolute magnitude cut introduced, hence there a lot more (fainter) objects in BOSS and with the radio-optical correlation (Serjeant et al. [1998]) they will also have lower radio fluxes.
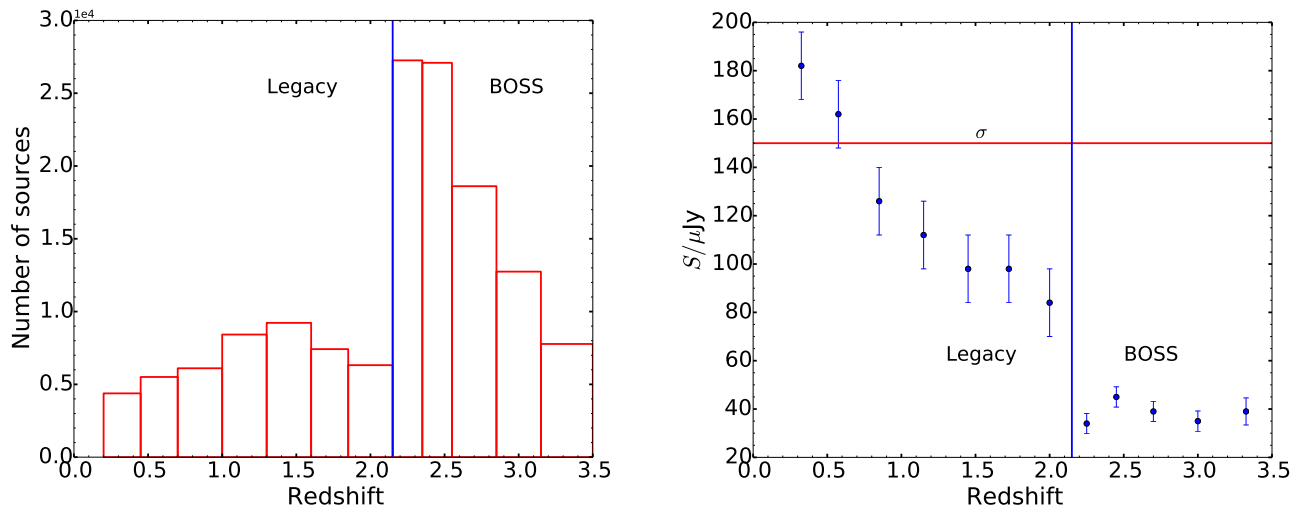
FIGURE 4.1: The left panel is the histogram of the number of sources in the 12 redshift bins in sample 3. The right panel show the stacked median fluxes from the 12 redshift slices and the red horizontal line shows the average rms $(1\sigma)$ for FIRST. The blue vertical line at redshifts $z = 2.15$ splits the data, $z < 2.15$ sources are taken from Legacy and $z > 2.15$ sources are taken from BOSS.

## 4.4 Bayesian framework

The median stacking method gives a single statistic representing a distribution of noise-dominated fluxes. Some authors have used this one-point statistic to compute average quantities such as star-formation rates (SFR) (e.g. Zwart et al. [2014], Karim et al. [2011], Dunne et al. [2009]). However, there is only so much one can do with stacked median flux. I follow the work of Zwart et al. [2015b], modelling source counts in a fully Bayesian framework, in order to constrain source counts and the RLF to values below the detection threshold.

### 4.4.1 Bayes' theorem

The use of Bayesian analysis methods has been increasing in astrophysics and cosmology over the past 20 years. This is because they provide a consistent way of estimating a set of parameters $\theta$ and in determining a model (or hypothesis) $H$ that best describes the data $D$. Bayes' theorem states:

$$P(\theta|D, H) = \frac{P(D|\theta, H)P(\theta|H)}{P(D|H)}, \tag{4.1}$$

where $P(\theta|D, H)$ is the target posterior probability distribution given the data and model, $P(D|\theta, H)$ is the likelihood $(\mathcal{L})$ the probability of the data given the model and parameters, $P(\theta|H)$ the prior, $\Pi$ and $P(D|H)$ is the Bayesian evidence $(\mathcal{Z})$. The Bayesian evidence normalizes the posterior and can be considered to be the average of the likelihood over the prior, written as an integral over the
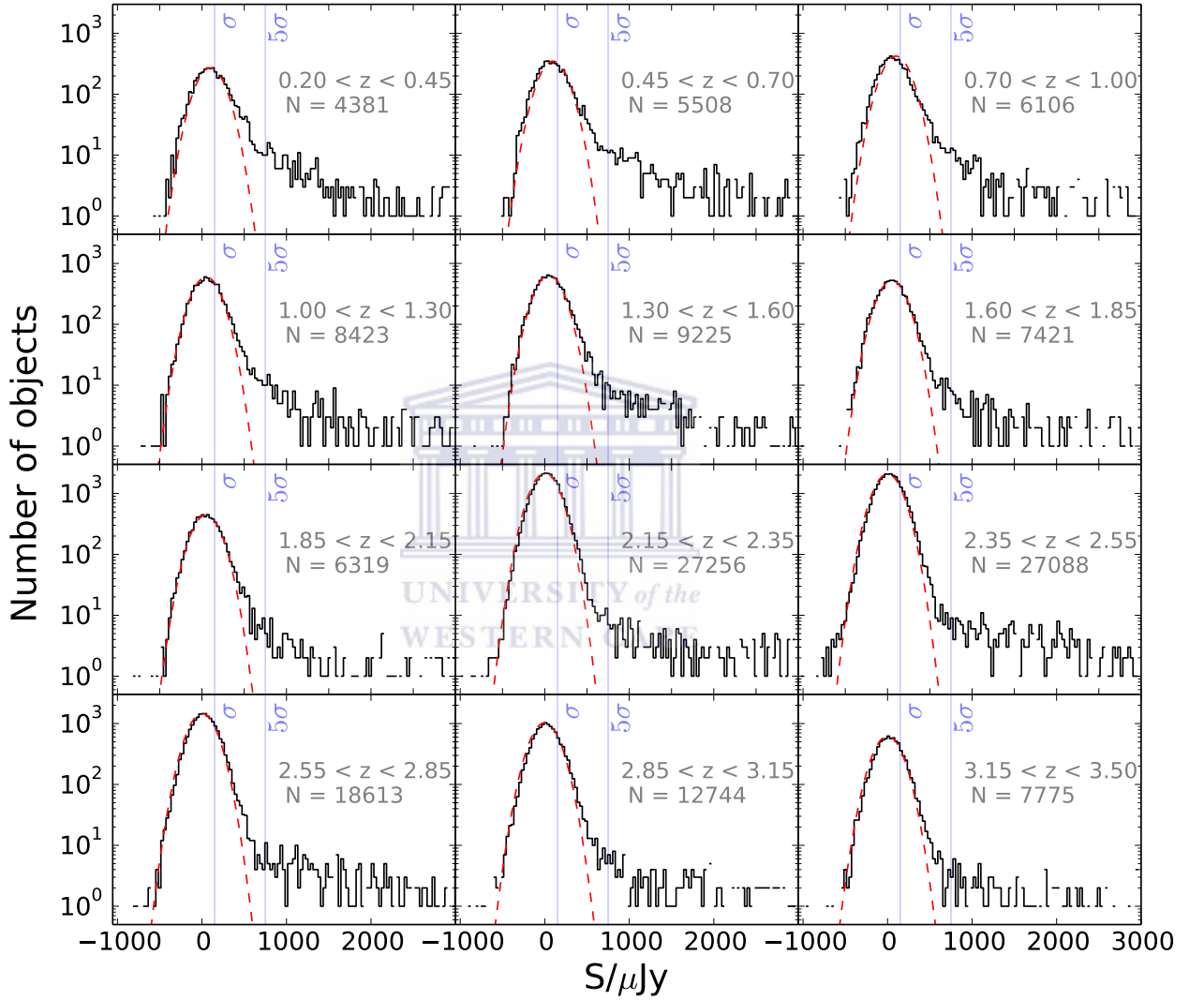
FIGURE 4.2: The flux distributions of the extracted FIRST fluxes from cut-outs centered at the SDSS quasar positions. The quasars are divided into 12 redshift slices, with those in the first seven redshift bins from Legacy and the rest from BOSS. The two blue lines in each bin represent the FIRST the RMS $\sigma = 150$ $\mu$Jy and $5\sigma = 750$ $\mu$Jy. The red dashed curve is a Gaussian with a width equal to the survey noise and the mean equal to the peak flux each slice.

$n$-dimensional parameter space,

$$\mathcal{Z} = \int \mathcal{L}\Pi d^n. \tag{4.2}$$

A model has a high evidence when a large portion of its prior parameter space is likely (large likelihood), and small evidence when a large portion of its parameters space has a small likelihood irrespective of how peaked the likelihood function is. This automatically adopts Occam's razor, i.e "a simpler theory with compact parameter space will have a larger evidence than a more complicated one unless the latter is significantly better at explaining the data." (Feroz et al. [2009b]).

In Bayesian model selection one would compare the evidence of two models A and B. This is computed by considering the ratio of their evidence $\mathcal{Z}_A/\mathcal{Z}_B$ (equivalent to the difference of their log-evidence $\ln[\mathcal{Z}_A - \mathcal{Z}_B]$), known as the Bayes factor. The Bayes factor effectively determines how model A better fits the data than model B. Jeffreys [1961] introduced a way to conclude on how significantly better Model A is compared to B based on the Bayes factor: $\Delta \ln \mathcal{Z} < 1$ is not significant, $1 < \Delta \ln \mathcal{Z} < 2.5$ significant, $2.5 < \Delta \ln \mathcal{Z} < 5$ strong and $\Delta \ln \mathcal{Z} > 5$ decisive.

### 4.4.2  Nested sampling

In order to compute the posterior distribution, one needs to sample from it normally using typical MCMC sampling. Sampling has always been one of the most computationally expensive parts of model selection because it involves solving the multidimensional integral in Eq 4.2. Nested sampling (Skilling [2004]) was created for efficient calculation of the evidence and has the added bonus of producing posterior inferences as a by-product.

MULTINEST(Feroz et al. [2009b]; Feroz et al. [2009a]; Buchner et al. [2014]), is a robust implementation of nested sampling. It gives out the full posterior distribution instead of a maximum, from which the uncertainty analysis can correctly be done with having assumed distribution for the data uncertainties.

### 4.4.3  Models considered here

Source counts usually have a power-law nature; Mitchell-Wynne et al. [2014] used a single power law fit to their data and Zwart et al. [2015b] had a variety of models from a single power-law (model A) to piecewise power laws with multiple slopes (Model B, C, D). The models are not limited to power laws; one can fit other models such as polynomials and poles/nodes (e.g Vernstrom et al. [2014]) or modified power laws. I follow Zwart et al. and use piecewise power laws, comparing them using the relative evidence to select the best model.

(i) **Model $A$**

The first model is a simple power law;

$$\frac{dN}{dS}(C, \alpha, S_{min}, S_{max}) = \begin{cases} CS^{\alpha} & S_{min} < S < S_{max} \\ 0 & \text{otherwise} \end{cases}, \tag{4.3}$$

where $\frac{dN}{dS}$ are the differential source counts, the number of sources $N$ with flux in the interval $[S, S + dS]$, $C$ is the normalization constant, $\alpha$ is the slope and $S_{min} < S < S_{max}$ are the lower and upper bounds of the model respectively.

(ii) **Model $B, C$ and $D$**

The next model is an extension of the previous model; with an extra power law that introduces two new parameters, a second slope $a_1$ and a break at $S_0$,

$$\frac{dN}{dS}(C, \alpha, \beta, S_{min}, S_0, S_{max}) = \begin{cases} CS^{\alpha} & S_{min} < S < S_0 \\ CS_0^{\alpha-\beta}S^{\beta} & S_0 < S < S_{max} \\ 0 & \text{otherwise.} \end{cases} \tag{4.4}$$

Model $C$ and Model $D$ have more breaks and slopes; Model is described by $\frac{dN}{dS}(C, \alpha, \beta, \gamma, S_{min}, S_0, S_1, S_{max})$ with one more break from Model $B$ and Model D is described by, $\frac{dN}{dS}(C, \alpha, \beta, \gamma, \delta, S_{min}, S_0, S_1, S_2, S_{max})$.

(iii) *Model $A', B', C'$, and $D'$*

I also consider the models $A', B', C'$, and $D'$ where I fit the radio noise $\sigma_n$ as a free parameter (see next Section 4.4.4). These models otherwise have the same expressions as their fixed noise counterparts $A, B, C, D$.

### 4.4.4   Likelihood

I now define the likelihood function of the binned fluxed data. I first consider the likelihood of finding $k_i$ objects in the $i^{th}$ bin. Since these are binned data, I assume that they follow a Poisson distribution with the mean number per flux interval given by $\frac{dN}{dS}(S)$ (normalized by the sky area). Therefore (ignoring the noise) the likelihood is,

$$\mathcal{L}_i(k_i|\boldsymbol{\theta}) = \frac{\lambda_i^{k_i}e^{-\lambda_i}}{k_i!}, \tag{4.5}$$

where $\lambda = \frac{dN}{dS}(S_i)\Delta S_i$ is the mean number in each bin and the mean number per flux bin $\frac{dN}{dS}(S_i)$ is assumed to be constant in the interval $\Delta S_i$. If one considers an infinitesimal interval $dS$, then there

will be zero or at most one object found in each bin with a likelihood given by,

$$\mathcal{L}_i\left(k_i = 1 | \boldsymbol{\theta}\right) = \frac{\lambda_i^{k_i} \mathrm{e}^{-\lambda_i}}{1!} \sim \lambda_i = \frac{dN}{dS}(S_i)dS_i. \tag{4.6}$$

I now consider a more realistic situation where the flux is

$$S_m = S + n, \tag{4.7}$$

where $S$ (Jy) is the 'real' flux from objects and $n$ (Jy) is the noise. The noise is assumed to follow a Gaussian distribution centered at zero with a variance $\sigma_n^2$. This is a good assumption considering Fig. 4.2. The likelihood is then,

$$\mathcal{L}_i\left(k_i | \boldsymbol{\theta}\right) = \frac{I_i^{k_i} \mathrm{e}^{-I_i}}{k_i!}, \tag{4.8}$$

where $I_i$ the theoretical expected value in each bin given by,

$$I_i = \int_{S_{min}}^{S_{max}} dS \frac{\mathrm{d}N(S)}{\mathrm{d}S} \int_{S_{m_i}}^{S_{m_i} + \Delta S_{m_i}} dS_m \frac{1}{\sigma_n \sqrt{2\pi}} \mathrm{e}^{-\frac{(S - S_m)^2}{2\sigma_n^2}}. \tag{4.9}$$

Solving the second integral in Eq. 4.9,

$$I_i = \int_{S_{min}}^{S_{max}} dS \frac{\mathrm{d}N(S)}{\mathrm{d}S} \frac{1}{2} \left\{ \mathrm{erf}\left(\frac{S - S_{m_i}}{\sigma_n \sqrt{2}}\right) - \mathrm{erf}\left(\frac{S - (S_{m_i} + \Delta S_{m_i})}{\sigma_n \sqrt{2}}\right) \right\}. \tag{4.10}$$

The total likelihood from the $n_{bins}$ bins is given by the product of the likelihood in each bin, assuming the bins are independent,

$$\mathcal{L}\left(\mathbf{k} | \boldsymbol{\theta}\right) = \prod_{i=1}^{n_{bins}} \mathcal{L}_i\left(k_i | \boldsymbol{\theta}\right). \tag{4.11}$$

### 4.4.5   Priors

Priors are the prior knowledge or limits of a parameter/data. They play an important role in Bayesian inference as they define the sampling parameter space. A uniform prior is the simplest form, providing an equal weighting of the parameter space. Most of the parameters were given uniform priors (Table 4.2) with the exception being the normalization $C$ which is a scale parameter and thus has a logarithmic uniform prior.

TABLE 4.2: Priors $\Pi(\theta|H)$.

| Parameter | Prior |
| --- | --- |
| $C/\mathrm{sr}^{-1}\mathrm{Jy}^{-1}$ | log-uniform $\in \left[10^{-3}, 10^{5}\right]$ |
| $\alpha, \beta, \gamma, \delta$ | uniform $\in [-2.5, -0.1]$ |
| $S_{min}/\mu\mathrm{Jy}$ | uniform $\in [0.01, 150.0]$ |
| $S_{max}/\mu\mathrm{Jy}$ | uniform $\in [150.0, 2000.0]$ |
| $S_{0,1,2}$ | uniform $\in [S_{min}, S_{max}]$ |
| $S_{0,1,2}$ | further require $S_0 < S_1 < S_2$ |
| $\sigma_n$ | $\delta\left(\sigma_{\mathrm{survey}}\right)$, or |
|  | uniform $\in [0.5, 2.0]\,\sigma_{\mathrm{survey}}$ |

Combining Eq. 4.11 with the priors in Table 4.2 and substituting into Eq. 4.1 one can determine the posterior probability distribution as well as the evidence. I use a Python implementation (Buchner et al. [2014]) of MULTINEST(PyMULTINEST) on a cluster with 48 cores. The code does not use much memory or disk space, but the number of parallel processors roughly determined the overall runtime.

### 4.4.6   Tests and simulations

I did not explicitly run any tests or simulations for the technique as this was already done by both Mitchell-Wynne et al. [2014] and Zwart et al. [2015b]. Mitchell-Wynne et al. ran a Markov Chain Monti-Carlo (MCMC) simulation using a $dN/dS$ model, from which they simulated fluxes and noise (drawn from a Gaussian). They then binned the data, which was found to be consistent with the theoretical expectations (Eq. 4.11). They then accurately recovered the model parameters by running the fit. Zwart et al. applied the technique to the Square Kilometre Array Design Studies SKA Simulated Skies (SKADS-S$^3$) simulations by Wilman et al. [2008]; 2010. SKADS is a semi-empirical simulation of the extragalactic radio continuum sky, covering a sky area of $20 \times 20$ deg$^2$ with $\approx 320$ million sources out to a redshift of $z = 20$ and flux density of 10 nJy. The sources have flux densities at 151 MHz, 610 MHz, 1.4 GHz, 4.86 GHz and 18 GHz, divided into six types: radio-quiet AGN (13%), radio-loud AGN FRI (9%), radio-loud AGN FRII, quiescent star-forming galaxies (76%) and starburst galaxies (2%). Zwart et al. fitted models $A, B, C$ and $D$ to extracted sources from a 1 deg$^2$ of SKADS and added random noise sampled from a Gaussian to each source. They ran the code on the SKADS noisy data and were able to successfully reconstruct the true source counts out to a known limit ($S_{\mathrm{min}}$).

## 4.5   Results

With the mathematical foundations of the method laid out, described and tested, I applied it to the data. I start by applying the method to samples 1 and 2, the two samples used in Chapter 3, and then to sample 3, the uniform sample (Section 2.2.3 and 4.2).
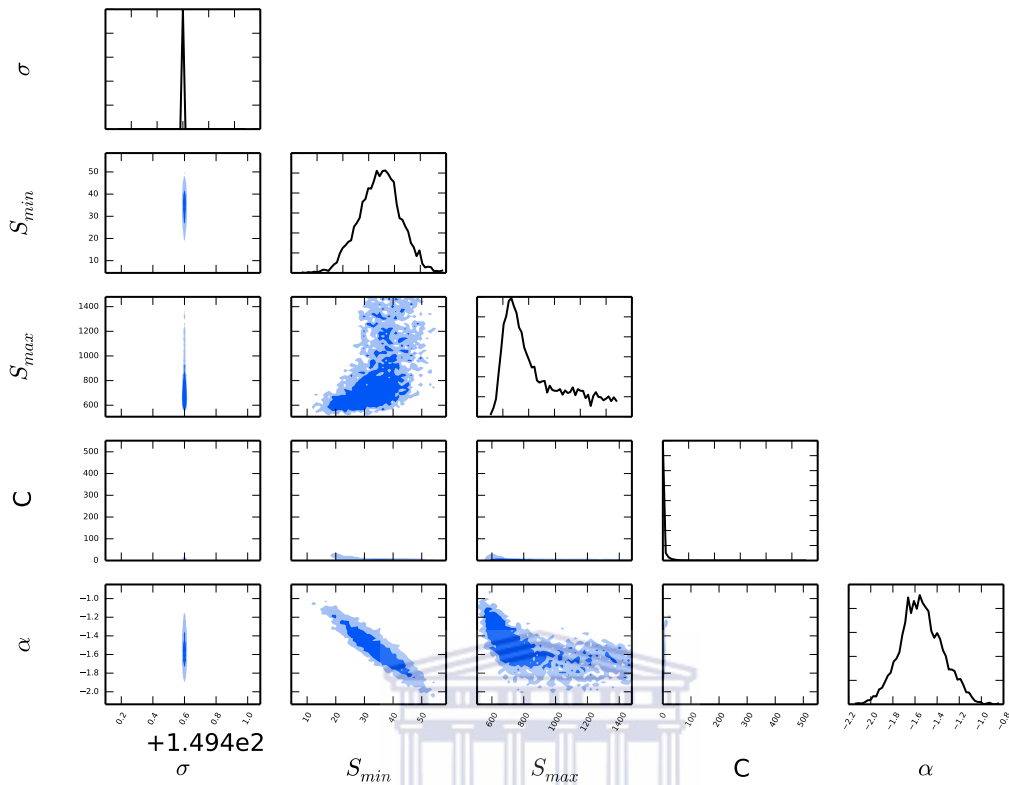
(A) Model A
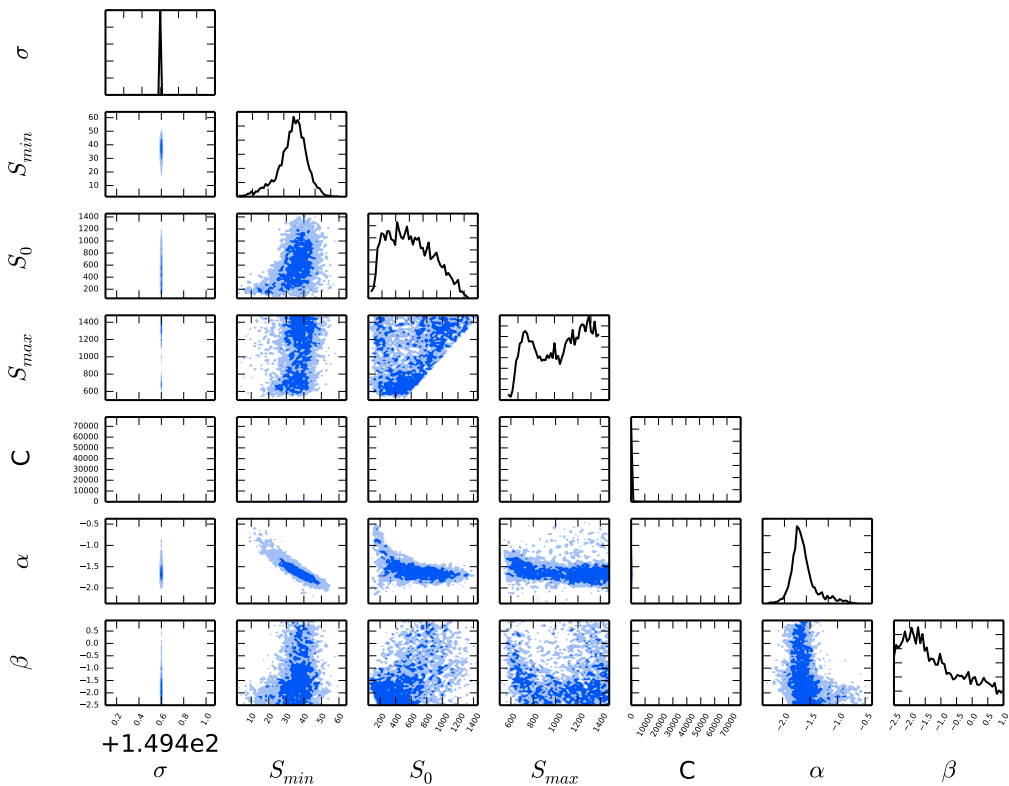


(B) Model B

FIGURE 4.3: The posterior distribution of the models $A, B, C$ and $D$d. The dark blue region are the 68% and the light region the 95% confidence levels. Model $A$ is the wining model with the highest evidence for sample 1.

(A) Model C



(B) Model D

FIGURE 4.4: Continuation of Fig. 4.3

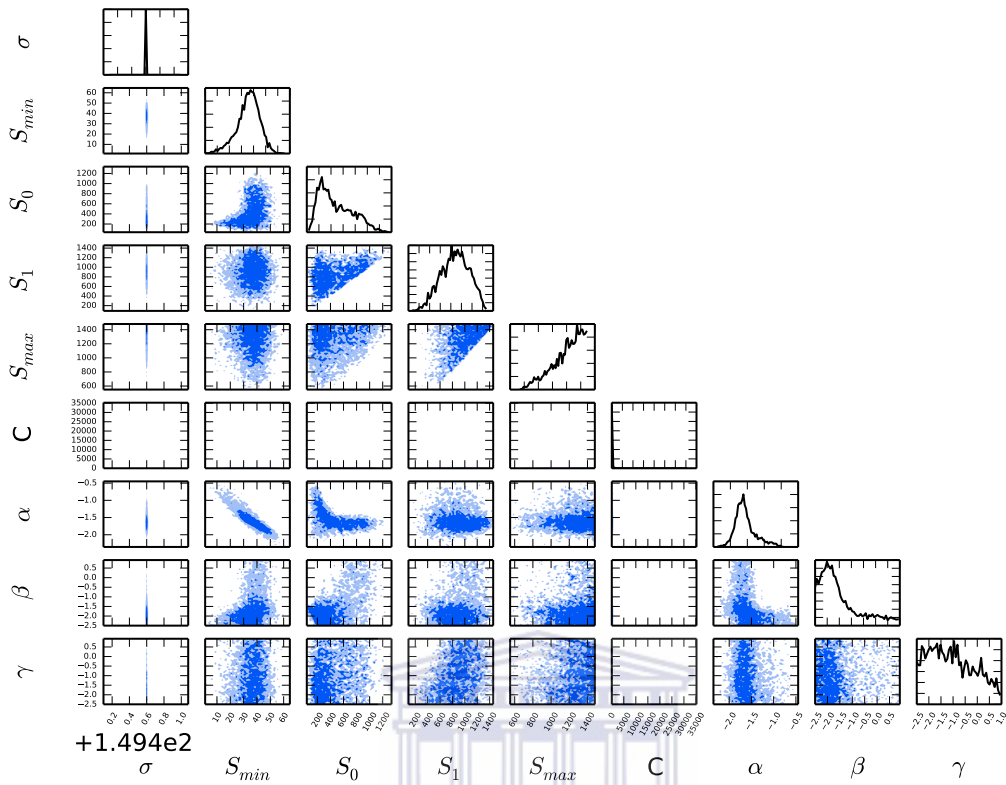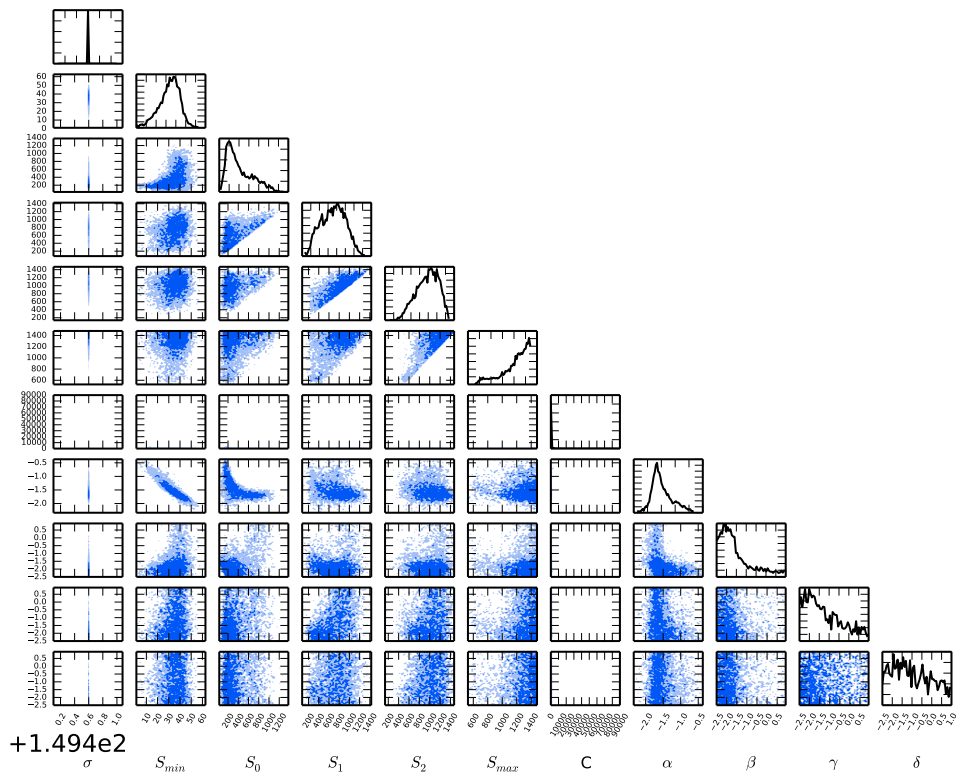| Slopes | Model | $\Delta \log \mathcal{Z}$ | Model | $\Delta \log \mathcal{Z}$ |
|--------|-------|-----------|--------|-----------|
| 1 | $A$ | $3.2 \pm 0.14$ | $A'$ | $1.4 \pm 0.15$ |
| 2 | $B$ | $3.0 \pm 0.14$ | $B'$ | $1.1 \pm 0.14$ |
| 3 | $C$ | $2.1 \pm 0.14$ | $C'$ | $0.5 \pm 0.15$ |
| 4 | $D$ | $1.9 \pm 0.15$ | $D'$ | $0.0 \pm 0.0$ |

TABLE 4.3: The relative evidence of the different source count models for sample 1 in the redshift range $0.25 < z < 0.45$ with $M_i < -23$. Model $D'$ is the reference evidence with the lowest log-evidence $\log_e \mathcal{Z} = -59.2 \pm 0.11$ and model $A$ is the winning model.

### 4.5.1 Posterior distributions

The Bayestack method returns the Bayesian evidence and the posterior for a given model. Fig. 4.3 and Fig. 4.4 show the triangle plots of the posterior for the Models $A, B, C$ and $D$. The posterior plots of Model A show that a single power law fits the data well, all the fitted parameters have a peak and the posteriors of $S_{min}$, $\alpha$ and $C$ are to a good approximation Gaussian. However, $S_{max}$ is not Gaussian, it is more Poisson-like and spans the whole prior range. The posterior plots of Model $B$ (a broken power law with two slopes) have one or two peaks and are highly non-Gaussian with the exception to the posterior of the first slope $\alpha$ and $S_{min}$. With these kinds of posteriors the assumption of a Gaussian posterior and Gaussian uncertainties made when using a $\chi^2$ estimator fail, showing why a fully Bayesian approach is necessary for this work. The posterior plots of Model $C$ and $D$ are very similar to that of Model $B$ with more slopes and breaks. In both models the marginalization of $S_{max}$ is cut off at the end, this is one of the priors of this parameter (Table 4.2) where we only explore fluxes below 1.5 mJy.

The winning model is found by comparing the evidence of the various models, using the Bayes factor. Table 4.3 shows the evidence (normalized to minimum evidence) of all the models (including the prime models of which the triangle plots are not shown) applied to sample 1. The model with the highest evidence for sample 1 is Model $A$ (simple power law). This procedure is done for sample 2 and the 12 redshift slices of sample 3 but I will not show the triangle plots or evidence tables.

Obtaining the best fit parameters from the posterior plot is not an easy task. This because of the (non-Gaussian) shape of posteriors as seen in Fig. 4.3 and Fig. 4.4. The Bayestack code returns three summaries or best fit values: the mean parameters, maximum likelihood parameters and maximum-a-posteriori (MAP) parameters. I use the MAP parameters because the mean is sensitive to outliers and the maximum likelihood assumes the posterior is Gaussian. Although MAP is the best statistic for this situation, it still does not fully describe the complex nature of the posterior.
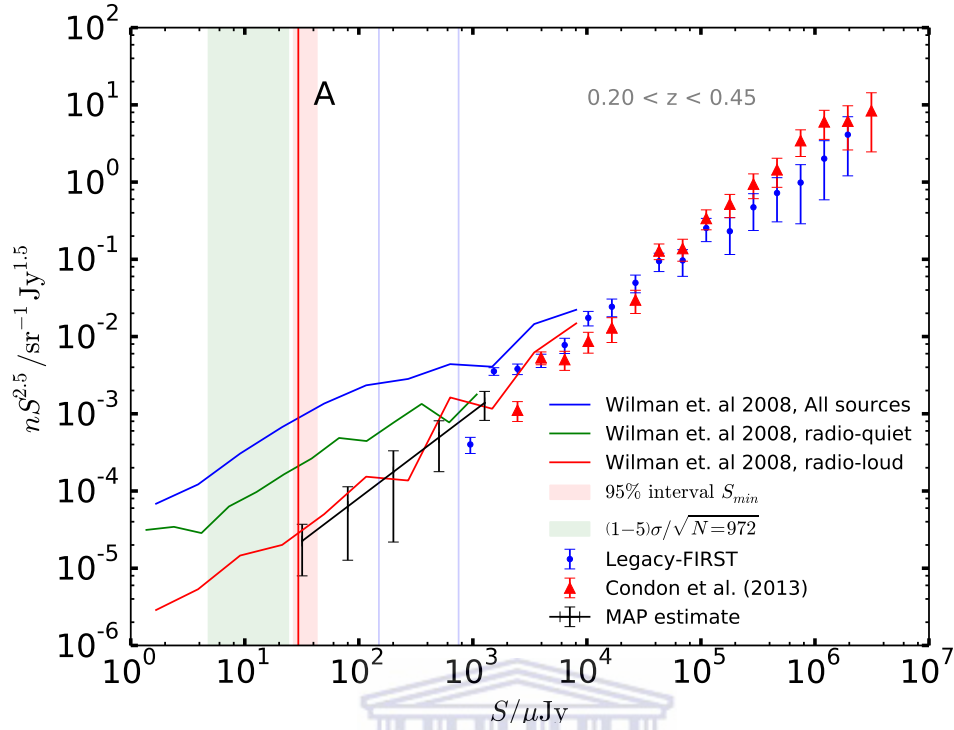
### 4.5.2   Source counts

Source counts are reconstructed by evaluating MAP parameters of winning models at each bin and the uncertainty is given by the 95% region around the median (re-centered on the MAP). The reconstructed source counts of samples 1 and 2 are shown in Fig. 4.5a and 4.5b respectively along with the detected sources. I use SKADS data at 1.4 GHz to compare the radio-quiet and radio-loud AGN with the quasars in our sample. Comparing the SKADS galaxies with the quasars in this work, I note that the (SDSS) quasars are optically selected and there is no way to impose this selection on the SKADS data. So I simply normalize the SKADS source counts because I am only interested in the shape (White et al. [2015]). I chose a normalization for each slice which is different for each sample (optical absolute magnitude cut), and each redshift (comoving volume cut). All the reconstructions are valid to a certain $S_{min}$ (one of the parameters) because the fit is mostly driven by the bright end which has a high SNR compared to the faint end. The depth also has a $1/\sqrt{N}$ (where $N$ is the number of sources in the fit) behavior so in general, the fit can be valid to a factor $\approx \sqrt{N}$ below the threshold (Zwart et al. [2015b]). The reconstruction of sample 1, which is best fitted by model $A$ (the simple power law), has the same slope as the counts of the detected sources. The SKADS counts are consistent with the detected sources with a slope similar to the reconstructed source below $5\sigma$. Sample 2 is best fitted by three slopes (model $C$); the SKADS counts are consistent with the detected counts until they fall off at $\approx 10^4 \mu$Jy. The reconstructed slope at the faint end has a similar slope to the SKADS counts.

In what follows I apply the fitting algorithm to the 12 redshift slices of sample 3. The reconstructions of the source counts are shown in Fig. 4.6 and 4.7, where they are compared with the SKADS sources (radio-quiet and radio-loud sources) and the detected sources in each bin. In general, the reconstructed counts are continuous from the detected counts and follow the SKADS counts, more so the radio-quiet AGN. There are a number of changes in the counts as a function of redshift. Below $z = 0.7$ the reconstructed counts and SKADS counts follow a power law. Above $z = 0.7$ the SKADS counts have a 'bump' at $S \approx 100$ mJy and the reconstructed counts are mostly best-fitted by a power-law with two slopes (model $B$). There is also an apparent evolution of $S_{min}$ as it seem to be going to lower fluxes with redshift. This is mostly due to the sample selection, at low redshifts I use Legacy and BOSS sources at higher redshifts. BOSS has significantly more sources than Legacy and will therefore having better fits at low fluxes.

### 4.5.3   Luminosity functions

My main goal is to investigate the nature of radio-quiet quasars and their emission as well as the processes behind it. The source counts in Section 4.5.2 shed light on the nature of these sources, but LFs are more fundamental as luminosity is an intrinsic property of the source. In this section, I construct LFs using the reconstructed counts. This is not a trivial objective because to generate LFs one needs

(A) Sample 1
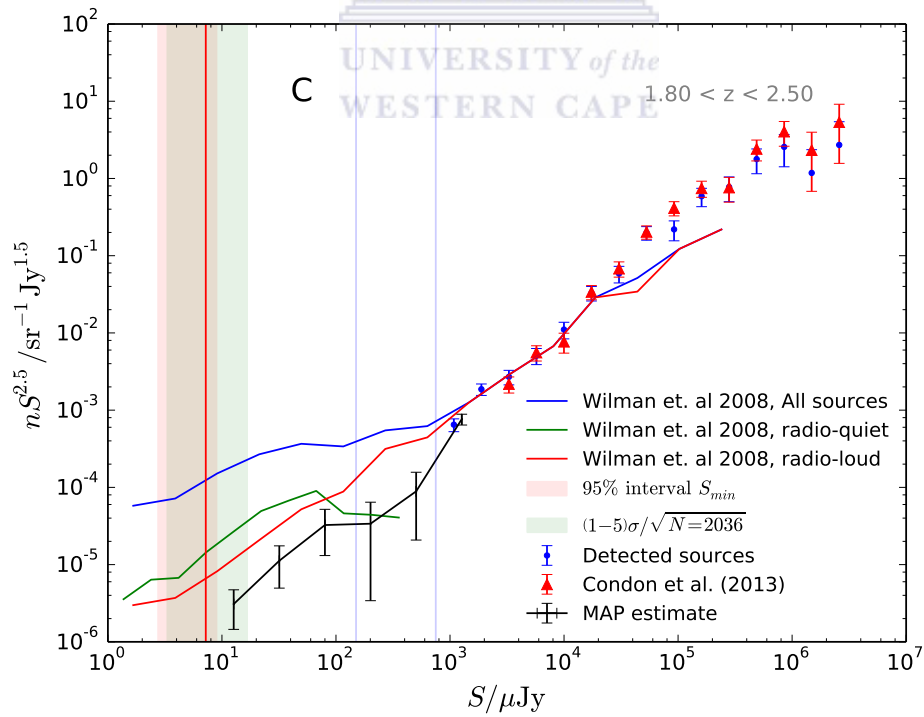


(B) Sample 2

FIGURE 4.5: The reconstructed source counts of the quasars in sample 1 and sample 2 using the best-fit model $A$ and $C$ respectively (shown at the bottom right of each plot). The black line is the maximum-a-posterior (MAP) reconstructed model with a 95% confidence level uncertainties. The red and blue points are the detected sources from Condon and this work. The blue, red and green lines represent all the extragalactic sources, radio-loud AGN and radio quiet AGN in SKADS. The red region is the 95% interval of $S_{\min}$ and the light blue region is the theoretically expected region for the value of $S_{\min}$. The two light blue lines represent $1\sigma$ and $5\sigma$ for FIRST and the red line marks $S_{\min}$.
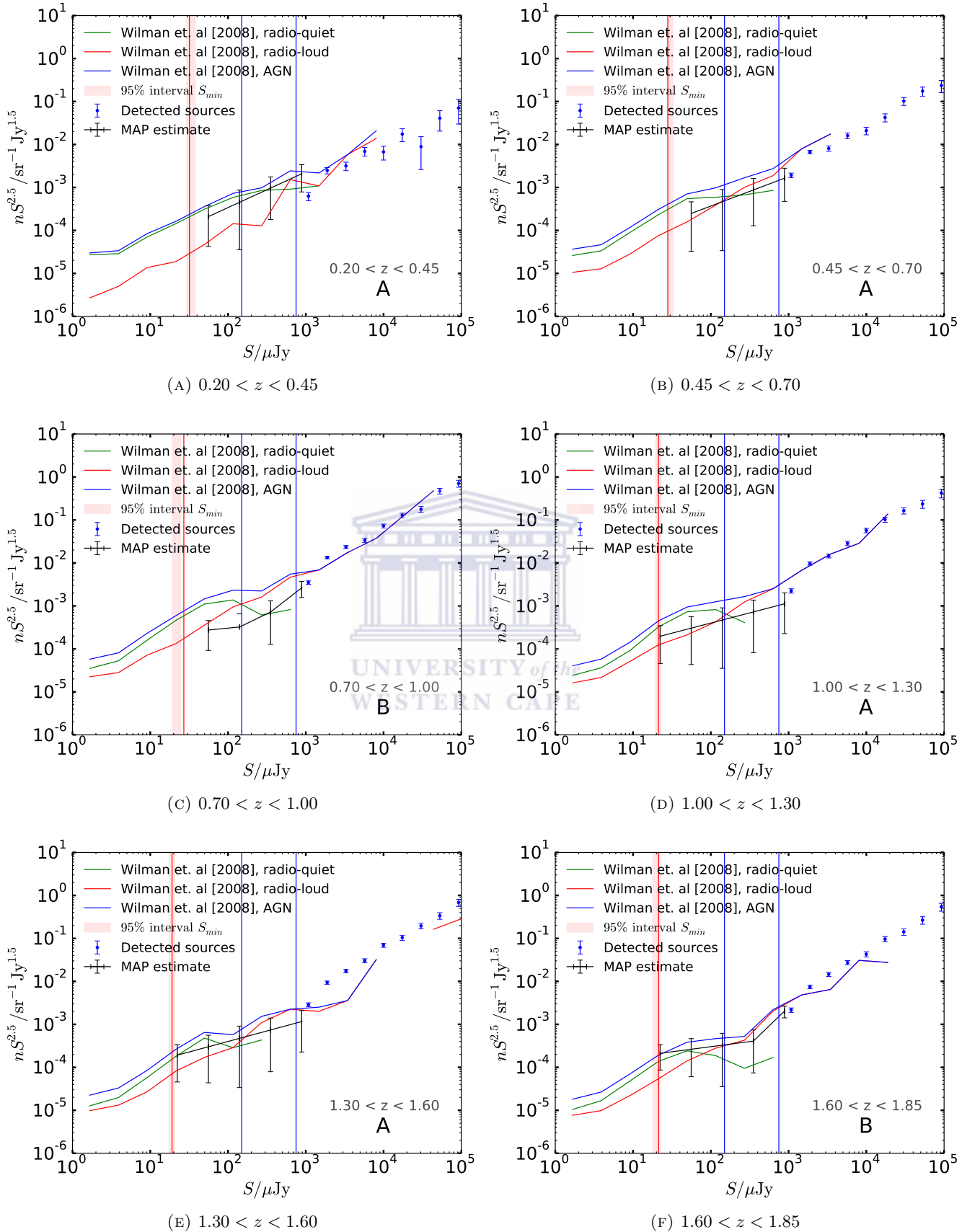
FIGURE 4.6: The reconstructed source counts of the quasars from sample 3. The best fit model to represent these sources is indicated at the bottom right of each panel. The black line is the maximum-a-posterior (MAP) reconstructed model with 95% confidence level uncertainties. The red and blue points are the detected sources from Condon and this work. The blue, red and green lines represent all the extragalactic sources, radio-loud AGN and radio-quiet AGN in SKADS. The two light blue lines represent $1\sigma$ and $5\sigma$ for FIRST. The red line marks $S_{\min}$ and the shaded red region is the 95% interval of $S_{\min}$.

(A) $1.85 < z < 2.15$

(B) $2.15 < z < 2.35$

(C) $2.35 < z < 2.55$

(D) $2.55 < z < 2.85$

(E) $2.85 < z < 3.15$

(F) $3.15 < z < 3.50$

FIGURE 4.7: Continuation of Fig. 4.6

luminosities or fluxes with redshift information. In this case, I have the reconstructed counts which contain flux information but no individual redshift for each flux (from the reconstruction). The only redshift information is the upper and lower bounds of each slice.

In order to convert the reconstructed counts from each redshift slice to LF, I assume that all the sources in each redshift slice are at the same redshift $z$ corresponding to the mean redshift of the slice. The Euclidean counts, $n\mathcal{S}^{2.5}$ ($\mathrm{sr}^{-1}\mathrm{Jy}^{1.5}$) (I use $\mathcal{S}$ to distinguish between the flux $S$ and Euclidean counts $n(\mathcal{S})$), of a bin with median flux $S$ ($\mu\mathrm{Jy}$) are given by,

$$n\mathcal{S}^{2.5} = \frac{1}{A}\frac{dN}{dS}S^{2.5}, \tag{4.12}$$

where $A$ (sr) is the survey area and $dN/dS$ is the number of sources in the flux bin. The first step is to convert the reconstructed Euclidean source counts $n\mathcal{S}^{2.5}$ to just $dN/dS$,

$$\frac{dN}{dS} = \frac{n\mathcal{S}^{2.5} \times A}{S^{2.5}}. \tag{4.13}$$

Consider the number of sources in a luminosity bin $dN/dL$ ($\mathrm{WHz}^{-1}$), which can be given by converting the flux bins into luminosity bins;

$$\frac{dN}{dL} = \frac{dS}{dL}\frac{dN}{dS}, \tag{4.14}$$

where $dS/dL$ is given by

$$\frac{dS}{dL} = \frac{1}{4\pi D_L^2(1+z)^{1+\alpha}}. \tag{4.15}$$

where $D_L$ is the luminosity distance and $\alpha$ is the spectral index. The mean $z$ is used to compute the luminosity distance for each slice (meaning all the sources in each slice are assumed to be at the same distance). The redshift bins should therefore be as small as possible to avoid large distance errors. From $dN/dL$ the LFs $\rho_m$ ($\mathrm{Mpc}^{-3}$ $\mathrm{mag}^{-1}$) can be computed by,
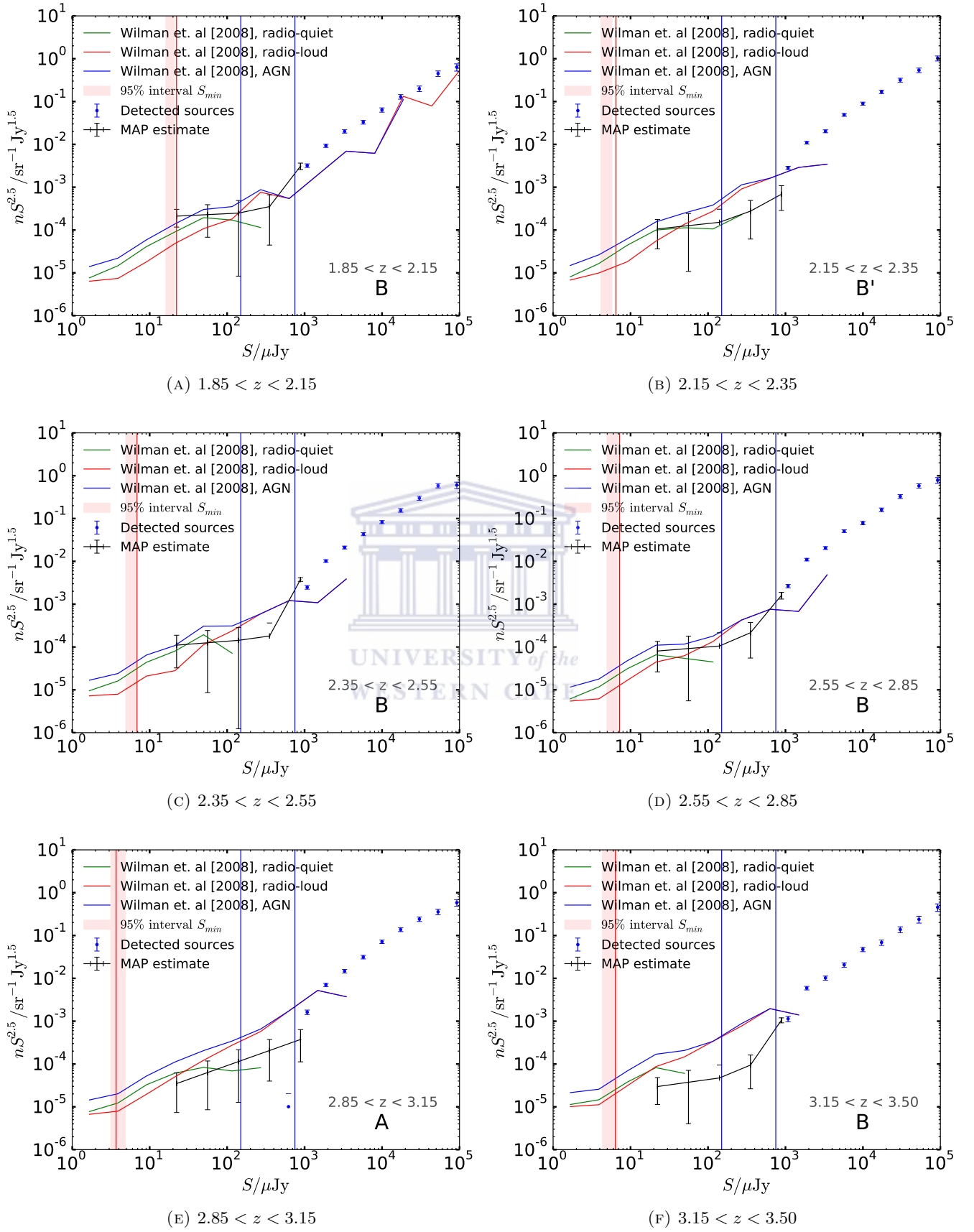
$$\rho_m = \frac{dN}{dL}\frac{1}{V_{\max}}\frac{1}{m}, \tag{4.16}$$

where $V_{\max}$ ($\mathrm{Mpc}^3$) is the comoving volume where the sources could have been detected, $m = 2.5$ The issue with the method is that defining $V_{\max}$ for undetected sources does not make much sense. However, I use $V_{\max}$ as the maximum volume in the redshift slice (e.i the comoving volume between minimum and maximum $z$) to normalize the LF.

I use this technique to construct the quasar radio LFs from the reconstructed quasars radio counts. Fig. 4.8 shows the reconstructed LFs for sample 1 and sample 2 along with the LF of the detected sources. The reconstructed LFs for Sample 1 is from a source count model of a power law with a single slope, the LFs is also a power law with no breaks and has a slope similar to that of the detected

sources. The continuous slope suggests that the emission processes governing the detected LFs and reconstructed LFs are the same. The reconstructed LFs for Sample 2 is based on a source counts model with three slopes. The LFs drops from the detected sources to the reconstructed LFs and rises to a slope similar to that of the detected sources.

This technique was applied to all the redshift slices of sample 3 (Fig. 4.9 and 4.10). The reconstructed LFs are consistent with SKADS radio-quiet although there are deviations at the bright end. At low redshifts ($z < 1$) the detected LFs follow a power-law and the reconstructed LFs have similar slopes to the detected LFs. This suggests that the dominant emission below and above the detection threshold is the same, i.e the quasars are dominated by AGN-related emission. Above $z = 1$ The detected LFs develop a 'knee' at $\log_{10}(L \ \mathrm{WHz}^{-1}) = 27$. The reconstruct LF appears to be steepening with redshift, deviating more and more from the slope of the detected LFs (still continuous in most cases). The steepening of the reconstructed LFs at fainter luminosities suggests that there are disproportionately more radio emission per unit optical luminosity for low-luminosity quasars, particularly at high redshift. This suggests that the strong link between optical luminosity and radio luminosity that is seen in brighter quasars (e.g. Serjeant et al. [1998]), that is generally attributed to a link between the accretion rate and the radio jet-power (Rawlings and Saunders [1991]), gradually breaking down towards fainter optical luminosities at high redshift. A possible explanation for this might be that this faint radio emission may actually be from star formation in the host galaxy, rather than related to the accretion process. This might also be expected to evolve with redshift as it is known that the star-formation rate density of the Universe strongly evolves from $z = 0$ out to $z \sim 2$. If this increase in star formation is mirrored in the host galaxies of the quasars in my sample, then I would expect to observe an enhanced amount of radio emission, that would be disproportionately evident for the faintest objects.

(A) Sample 1



(B) Sample 2

FIGURE 4.8: The quasar radio luminosity functions of sample 1 and sample 2. The black points are the constructed LF function from the MAP source counts and the grey region is the uncertainty. The blue points are the LF of the detected sources constructed from source counts using the same method as the MAP source count. The red triangles are from Condon et al. [2013]
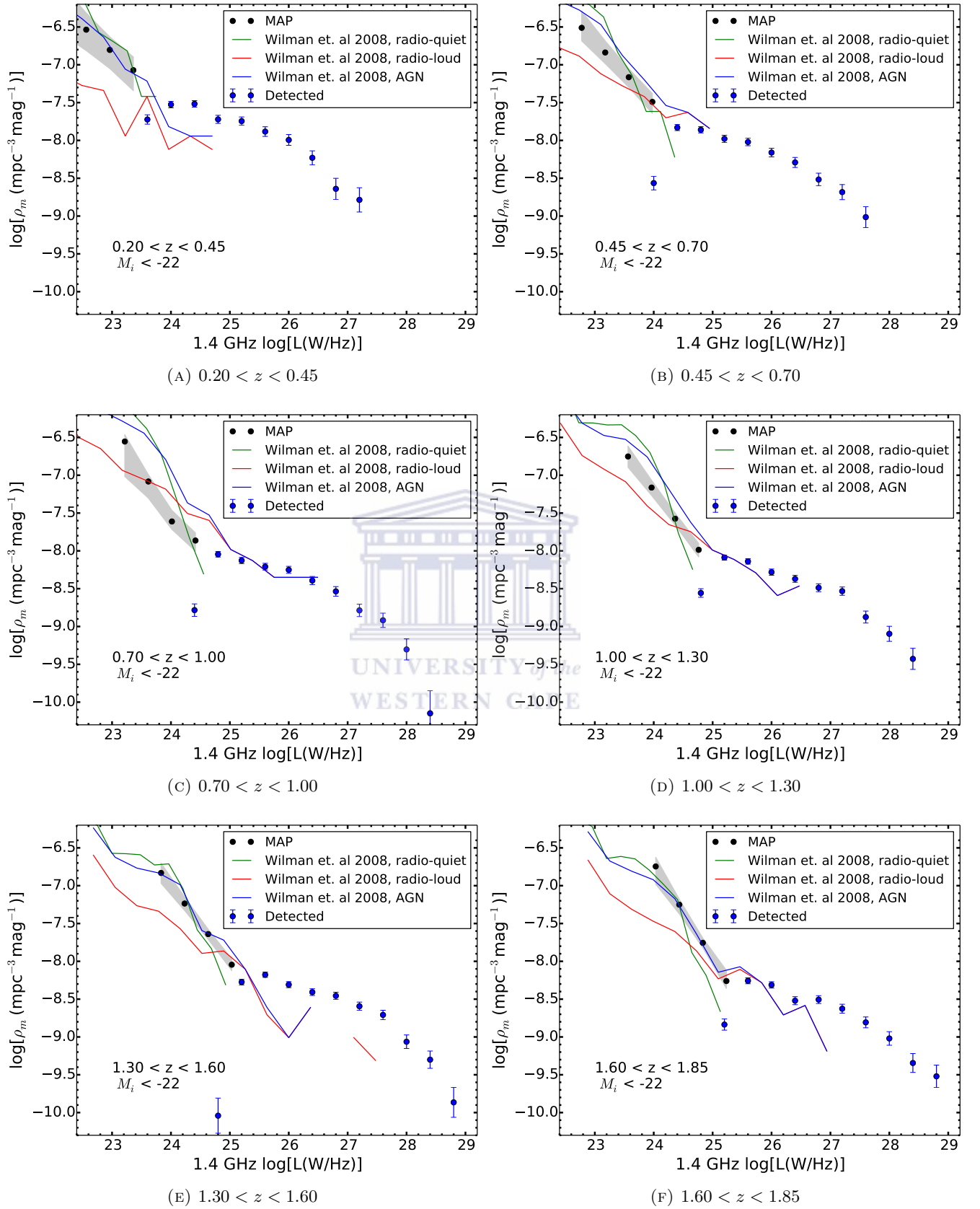
FIGURE 4.9: The luminosity function of the 12 redshift slices in the sample 3. The back points and gray region are the reconstructed LF created using the reconstructed counts. The blue points are the LFs from detected sources in Sample 1 and Sample 2 and the red triangles are the LFs from Condon's data. The blue, red and green lines represent all the extragalactic sources, radio-loud AGN and radio-quiet AGN in SKADS.

(A) $1.85 < z < 2.15$



(B) $2.15 < z < 2.35$



(C) $2.35 < z < 2.55$



(D) $2.55 < z < 2.85$



(E) $2.85 < z < 3.15$



(F) $3.15 < z < 3.50$
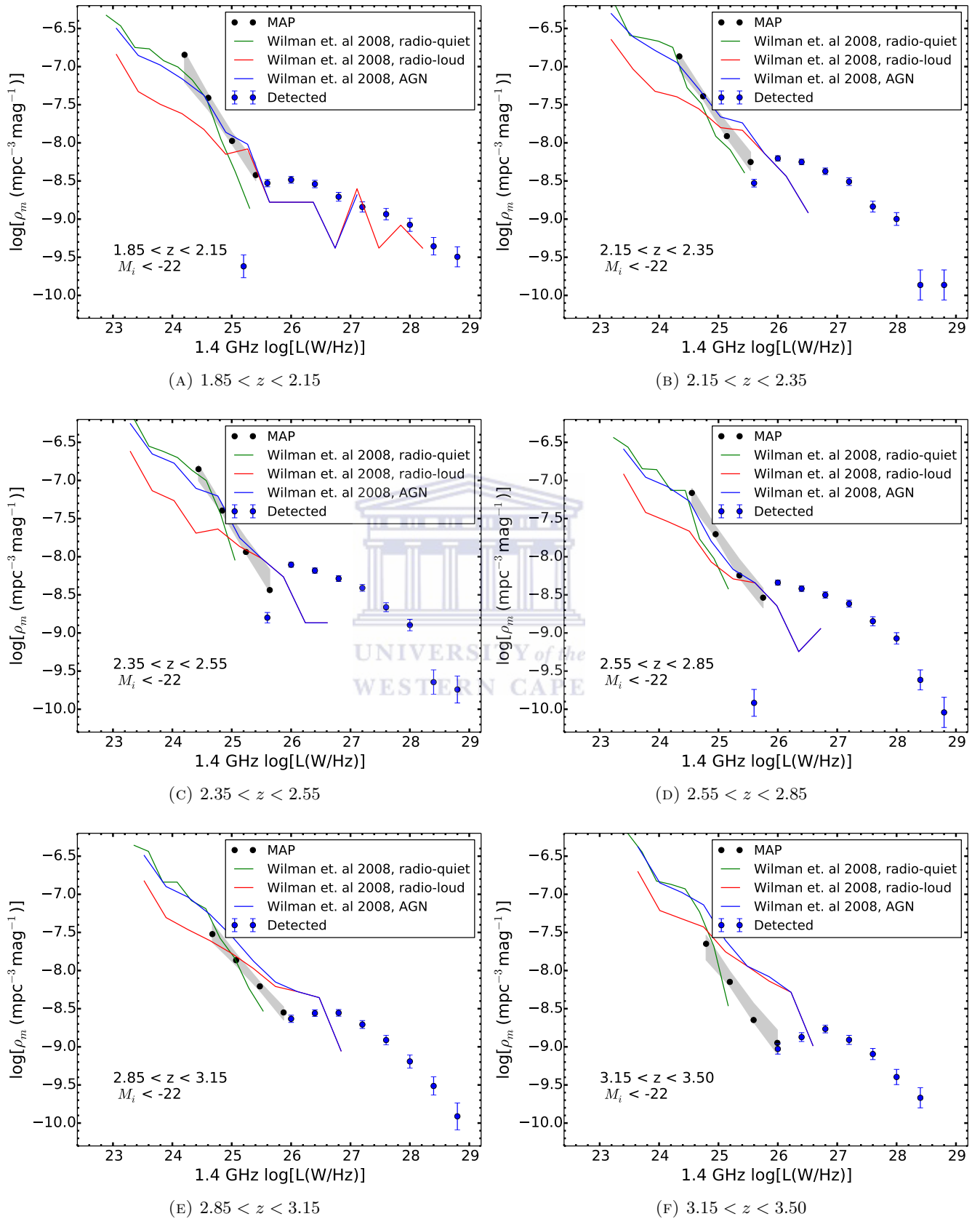
FIGURE 4.10: Continues from Fig. 4.9

# Chapter 5

# Conclusions and future work

Understanding the nature of the emission of radio-quiet AGN is very important, whether it is dominated by SF or related to AGN accretion, to galaxy formation and evolution. They make up $\approx 90\%$ of the total quasar population and many lie below the detection threshold of completed large-area radio surveys (e.g. Ivezić et al. [2002]). I use optical quasars from SDSS's BOSS (Eisenstein et al. [2011]) and Legacy (Richards et al. [2002]) along with radio data from FIRST (Becker et al. [1995]) to investigate the radio emission from radio-quiet AGN.

I matched SDSS samples with detected radio-loud quasars in the FIRST catalogue. I constructed quasar radio source counts and QRLF and found that they are consistent with the work of Condon et al. [2013], who used SDSS and NVSS data. There are inconsistencies at the faint end of the source counts due to the difference in resolutions and detection limits. This is because when using extended baselines in the VLA like for FIRST extended emission is resolved out, and therefore, the amount of radio emission would be underestimated. This would move objects to fainter radio fluxes than they actually are and some will disappear from the FIRST survey altogether. This would decrease the source counts as you get closer to the flux limit ($5\sigma$). However, when using smaller baselines like in NVSS you miss very little extended emission, but the flux-limit is higher, therefore you don't get as deep as you do with FIRST. Even with a $5\sigma$ detection threshold you still probably only detect $\approx 80\%$ of the objects in both surveys.

In Chapter 4, I used two stacking techniques to make measurements of the radio emission from radio-quiet quasars. The first technique is a simple average stacking approach, that gave a median radio flux of the sources below the threshold. The median flux was found to decrease exponentially with increasing redshift (which is expected, White et al. [2007]) from 182 $\mu$Jy at $0.2 < z < 0.45$ to 39 $\mu$Jy at $3.15 < z < 3.5$. This decreases is due to the fact that at higher redshift quasars are generally fainter, but this is slightly counteracted by the optical selection imposed which means that the higher redshift

sources are generally more luminous. However, given that the correlation between optical luminosity and radio luminosity in radio-quiet quasars is not linear and has a broad scatter, it is not surprising that the median radio flux decreases with redshift. I also find a discontinuity between the median flux from Legacy and BOSS. This discontinuity is from the fact that BOSS reaches fainter apparent magnitudes within the $M_i = 22$ absolute magnitude cut introduced, hence there a lot more (fainter) objects in BOSS and with the radio-optical correlation Serjeant et al. [1998]) they will also have lower radio fluxes.

The second approach is a fully Bayesian technique, where radio source count models were fitted to the sources below the detection threshold (Zwart et al. [2015b]). I considered piece-wise power-law models with different breaks and slopes, which I fitted to the data and obtained the reconstructed counts. The reconstructed counts were compared to SKADS simulated counts (Wilman et al. [2008]; 2010) which were normalized (White et al. [2015]) to fit the counts (because optical magnitudes cannot reliably be applied to SKADS). The reconstruction in most cases follows the shape of the source counts from the SKADS radio-quiet AGN population.

The reconstructed counts were converted into LFs, by assuming that all sources in a redshift slice have the same redshift. The reconstructed LFs are consistent with the shape of the SKADS radio-quiet although there are deviations at the bright end, where the SKADS radio-quiet population rapidly drops off compared to the reconstructed LFS. This is purely due to the way the SKADS sources separated into radio-loud and radio-quiet (Wilman et al. [2008]). At low redshifts ($z < 1$) the detected LFs follow a power-law and the reconstructed LFs have similar slopes to the detected LFs. This suggests that the dominant emission below and above the detection threshold is the same, i.e. the quasars are dominated by AGN-related emission. Above $z = 1$ The detected LFs develop a 'knee' at $\log_{10}(L$ WHz$^{-1}) = 27$. The reconstructed LFs appears to be steepening with redshift, deviating more and more from the slope of the detected LFs (but still continuous in most cases). The steepening of the reconstructed LFs at fainter luminosities suggests that there are disproportionately more radio emission per unit optical luminosity for low-luminosity quasars, particularly at high redshift. This suggests that the strong link between optical luminosity and radio luminosity that is seen in brighter quasars (e.g. Serjeant et al. [1998]), that is generally attributed to a link between the accretion rate and the radio jet-power (Rawlings and Saunders [1991]), gradually breaking down towards fainter optical luminosities at high redshift. A possible explanation for this might be that this faint radio emission may actually be from star formation in the host galaxy, rather than related to the accretion process. This might also be expected to evolve with redshift as it is known that the star-formation rate density of the Universe strongly evolves from $z = 0$ out to $z \sim 2$. If this increase in star formation is mirrored in the host galaxies of the quasars in my sample, then I would expect to observe an enhanced amount of radio emission, that would be disproportionately evident for the faintest objects.

## 5.1 Future work

(i) In this work, I only considered piece-wise power-law for fitting the source counts. There are other interesting models one could consider (e.g. polynomials and bins/poles), that might better fit the data.

(ii) The sources at the bright end drive most of the fit as they have a higher SNR than those at the faint end. It would be interesting slice the data into smaller flux bins (i.e. three bins, one at the faint end the second in the middle fluxes and the third at the bright end) and run independent fits and compare the results to the single fit I presented.

(iii) It would be interesting to run the fit directly in luminosity space (and not have to worry about computing $V_{\mathrm{max}}$ for undetected sources) similar to Roseboom and Best [2014] and compare with the technique used in this work.

(iv) Given that I found a steepening at the faint end of the LFs, it would be good to confirm this using a fainter sample, both optically and with deeper radio data. The deeper radio data that will be coming with the upgraded JVLA (data already exists on Stripe 82; Heywood et al. submitted), as well as LOFAR, MeerKAT and eventually the SKA.

The deeper data from the new generation of radio telescopes will allow fainter detections above the threshold but using stacking techniques such as the one presented in this thesis puts one a step ahead to much fainter radio LF. For example, MIGHTEE aims to reach the $1\mu$Jy rms level over 20 deg$^2$. If there are $\sim 2000$ quasars over the area, then one can reach 100 nJy levels using this technique. The new-generation telescopes will reach lower flux levels (down to $\mu$Jy with the SKA pathfinders and nJy with the SKA). This will provide more data to further investigate dominant emission in radio-quiet AGN since most of the population will be detected.

# Bibliography

K. Abazajian, J. K. Adelman-McCarthy, M. A. Agüeros, S. S. Allam, K. Anderson, S. F. Anderson, J. Annis, N. A. Bahcall, I. K. Baldry, S. Bastian, A. Berlind, M. Bernardi, M. R. Blanton, J. J. Bochanski, Jr., W. N. Boroski, J. W. Briggs, J. Brinkmann, R. J. Brunner, T. Budavári, L. N. Carey, S. Carliles, F. J. Castander, A. J. Connolly, I. Csabai, M. Doi, F. Dong, D. J. Eisenstein, M. L. Evans, X. Fan, D. P. Finkbeiner, S. D. Friedman, J. A. Frieman, M. Fukugita, R. R. Gal, B. Gillespie, K. Glazebrook, J. Gray, E. K. Grebel, J. E. Gunn, V. K. Gurbani, P. B. Hall, M. Hamabe, F. H. Harris, H. C. Harris, M. Harvanek, T. M. Heckman, J. S. Hendry, G. S. Hennessy, R. B. Hindsley, C. J. Hogan, D. W. Hogg, D. J. Holmgren, S.-i. Ichikawa, T. Ichikawa, Ž. Ivezić, S. Jester, D. E. Johnston, A. M. Jorgensen, S. M. Kent, S. J. Kleinman, G. R. Knapp, A. Y. Kniazev, R. G. Kron, J. Krzesinski, P. Z. Kunszt, N. Kuropatkin, D. Q. Lamb, H. Lampeitl, B. C. Lee, R. F. Leger, N. Li, H. Lin, Y.-S. Loh, D. C. Long, J. Loveday, R. H. Lupton, T. Malik, B. Margon, T. Matsubara, P. M. McGehee, T. A. McKay, A. Meiksin, J. A. Munn, R. Nakajima, T. Nash, E. H. Neilsen, Jr., H. J. Newberg, P. R. Newman, R. C. Nichol, T. Nicinski, M. Nieto-Santisteban, A. Nitta, S. Okamura, W. O'Mullane, J. P. Ostriker, R. Owen, N. Padmanabhan, J. Peoples, J. R. Pier, A. C. Pope, T. R. Quinn, G. T. Richards, M. W. Richmond, H.-W. Rix, C. M. Rockosi, D. J. Schlegel, D. P. Schneider, R. Scranton, M. Sekiguchi, U. Seljak, G. Sergey, B. Sesar, E. Sheldon, K. Shimasaku, W. A. Siegmund, N. M. Silvestri, J. A. Smith, V. Smolčić, S. A. Snedden, A. Stebbins, C. Stoughton, M. A. Strauss, M. SubbaRao, A. S. Szalay, I. Szapudi, P. Szkody, G. P. Szokoly, M. Tegmark, L. Teodoro, A. R. Thakar, C. Tremonti, D. L. Tucker, A. Uomoto, D. E. Vanden Berk, J. Vandenberg, M. S. Vogeley, W. Voges, N. P. Vogt, L. M. Walkowicz, S.-i. Wang, D. H. Weinberg, A. A. West, S. D. M. White, B. C. Wilhite, Y. Xu, B. Yanny, N. Yasuda, C.-W. Yip, D. R. Yocum, D. G. York, I. Zehavi, S. Zibetti, and D. B. Zucker. The Second Data Release of the Sloan Digital Sky Survey. *A J*, 128:502–512, July 2004. doi: 10.1086/421365.

R. A. Alpher, R. Herman, and G. A. Gamow. Thermonuclear Reactions in the Expanding Universe. *Physical Review*, 74:1198–1199, November 1948. doi: 10.1103/PhysRev.74.1198.2.

L. Anderson, É. Aubourg, S. Bailey, F. Beutler, V. Bhardwaj, M. Blanton, A. S. Bolton, J. Brinkmann, J. R. Brownstein, A. Burden, C.-H. Chuang, A. J. Cuesta, K. S. Dawson, D. J. Eisenstein, S. Escoffier, J. E. Gunn, H. Guo, S. Ho, K. Honscheid, C. Howlett, D. Kirkby, R. H. Lupton,

M. Manera, C. Maraston, C. K. McBride, O. Mena, F. Montesano, R. C. Nichol, S. E. Nuza, M. D. Olmstead, N. Padmanabhan, N. Palanque-Delabrouille, J. Parejko, W. J. Percival, P. Petitjean, F. Prada, A. M. Price-Whelan, B. Reid, N. A. Roe, A. J. Ross, N. P. Ross, C. G. Sabiu, S. Saito, L. Samushia, A. G. Sánchez, D. J. Schlegel, D. P. Schneider, C. G. Scoccola, H.-J. Seo, R. A. Skibba, M. A. Strauss, M. E. C. Swanson, D. Thomas, J. L. Tinker, R. Tojeiro, M. V. Magaña, L. Verde, D. A. Wake, B. A. Weaver, D. H. Weinberg, M. White, X. Xu, C. Yèche, I. Zehavi, and G.-B. Zhao. The clustering of galaxies in the SDSS-III Baryon Oscillation Spectroscopic Survey: baryon acoustic oscillations in the Data Releases 10 and 11 Galaxy samples. *MNRAS*, 441:24–62, June 2014. doi: 10.1093/mnras/stu523.

R. H. Becker, R. L. White, and D. J. Helfand. The FIRST Survey: Faint Images of the Radio Sky at Twenty Centimeters. *Astrophys. J.*, 450:559, September 1995. doi: 10.1086/176166.

P. N. Best. Radio-Loud AGN Heating in Elliptical Galaxies and Clusters. In H. Böhringer, G. W. Pratt, A. Finoguenov, and P. Schuecker, editors, *Heating versus Cooling in Galaxies and Clusters of Galaxies*, page 166, 2007. doi: 10.1007/978-3-540-73484-0_31.

A. D. Biggs and R. J. Ivison. A catalogue of $\mu$Jy radio sources in northern legacy fields. *MNRAS*, 371:963–971, September 2006. doi: 10.1111/j.1365-2966.2006.10730.x.

M. R. Blanton, D. W. Hogg, N. A. Bahcall, J. Brinkmann, M. Britton, A. J. Connolly, I. Csabai, M. Fukugita, J. Loveday, A. Meiksin, J. A. Munn, R. C. Nichol, S. Okamura, T. Quinn, D. P. Schneider, K. Shimasaku, M. A. Strauss, M. Tegmark, M. S. Vogeley, and D. H. Weinberg. The Galaxy Luminosity Function and Luminosity Density at Redshift z = 0.1. *Astrophys. J.*, 592: 819–838, August 2003. doi: 10.1086/375776.

D. C.-J. Bock, M. I. Large, and E. M. Sadler. SUMSS: A Wide-Field Radio Imaging Survey of the Southern Sky. I. Science Goals, Survey Design, and Instrumentation. *A J*, 117:1578–1593, March 1999. doi: 10.1086/300786.

M. Bondi, P. Ciliegi, E. Schinnerer, V. Smolčić, K. Jahnke, C. Carilli, and G. Zamorani. The VLA-COSMOS Survey. III. Further Catalog Analysis and the Radio Source Counts. *Astrophys. J.*, 681: 1129–1135, July 2008. doi: 10.1086/589324.

M. Bondi et al. The VLA-VIRMOS Deep Field. I. Radio observations probing the mu Jy source population. *A&A*, 403:857–867, June 2003. doi: 10.1051/0004-6361:20030382.

M. Bonzini, V. Mainieri, P. Padovani, P. Andreani, S. Berta, M. Bethermin, D. Lutz, G. Rodighiero, D. Rosario, P. Tozzi, and S. Vattakunnel. Star formation properties of sub-mJy radio sources. *MNRAS*, 453:1079–1094, October 2015. doi: 10.1093/mnras/stv1675.

N. Bourne, S. J. Maddox, L. Dunne, R. Auld, M. Baes, I. K. Baldry, D. G. Bonfield, A. Cooray, S. M. Croom, A. Dariush, G. de Zotti, S. P. Driver, S. Dye, S. Eales, H. L. Gomez, J. González-Nuevo, A. M. Hopkins, E. Ibar, M. J. Jarvis, A. Lapi, B. Madore, M. J. Michałowski, M. Pohlen,

C. C. Popescu, E. E. Rigby, M. Seibert, D. J. B. Smith, R. J. Tuffs, P. van der Werf, S. Brough, S. Buttiglione, A. Cava, D. L. Clements, C. J. Conselice, J. Fritz, R. Hopwood, R. J. Ivison, D. H. Jones, L. S. Kelvin, J. Liske, J. Loveday, P. Norberg, A. S. G. Robotham, G. Rodighiero, and P. Temi. Herschel-ATLAS/GAMA: a census of dust in optically selected galaxies from stacking at submillimetre wavelengths. *MNRAS*, 421:3027–3059, April 2012. doi: 10.1111/j.1365-2966.2012. 20528.x.

J. Bovy, J. F. Hennawi, D. W. Hogg, A. D. Myers, J. A. Kirkpatrick, D. J. Schlegel, N. P. Ross, E. S. Sheldon, I. D. McGreer, D. P. Schneider, and B. A. Weaver. Think Outside the Color Box: Probabilistic Target Selection and the SDSS-XDQSO Quasar Targeting Catalog. *Astrophys. J.*, 729:141, March 2011a. doi: 10.1088/0004-637X/729/2/141.

J. Bovy, J. F. Hennawi, D. W. Hogg, A. D. Myers, and N. P. Ross. The SDSS-XDQSO quasar targeting catalog. In *American Astronomical Society Meeting Abstracts #217*, volume 43 of *Bulletin of the American Astronomical Society*, page 222.05, January 2011b.

B. J. Boyle, T. Shanks, and B. A. Peterson. The evolution of optically selected QSOs. II. *MNRAS*, 235:935–948, December 1988. doi: 10.1093/mnras/235.3.935.

B. J. Boyle, T. Shanks, S. M. Croom, R. J. Smith, L. Miller, N. Loaring, and C. Heymans. The 2dF QSO Redshift Survey - I. The optical luminosity function of quasi-stellar objects. *MNRAS*, 317: 1014–1022, October 2000. doi: 10.1046/j.1365-8711.2000.03730.x.

J. Buchner, A. Georgakakis, K. Nandra, L. Hsu, C. Rangel, M. Brightman, A. Merloni, M. Salvato, J. Donley, and D. Kocevski. X-ray spectral modelling of the AGN obscuring region in the CDFS: Bayesian model selection and catalogue. *A&A*, 564:A125, April 2014. doi: 10.1051/0004-6361/ 201322971.

N. G. Busca, T. Delubac, J. Rich, S. Bailey, A. Font-Ribera, D. Kirkby, J.-M. Le Goff, M. M. Pieri, A. Slosar, É. Aubourg, J. E. Bautista, D. Bizyaev, M. Blomqvist, A. S. Bolton, J. Bovy, H. Brewington, A. Borde, J. Brinkmann, B. Carithers, R. A. C. Croft, K. S. Dawson, G. Ebelke, D. J. Eisenstein, J.-C. Hamilton, S. Ho, D. W. Hogg, K. Honscheid, K.-G. Lee, B. Lundgren, E. Malanushenko, V. Malanushenko, D. Margala, C. Maraston, K. Mehta, J. Miralda-Escudé, A. D. Myers, R. C. Nichol, P. Noterdaeme, M. D. Olmstead, D. Oravetz, N. Palanque-Delabrouille, K. Pan, I. Pâris, W. J. Percival, P. Petitjean, N. A. Roe, E. Rollinde, N. P. Ross, G. Rossi, D. J. Schlegel, D. P. Schneider, A. Shelden, E. S. Sheldon, A. Simmons, S. Snedden, J. L. Tinker, M. Viel, B. A. Weaver, D. H. Weinberg, M. White, C. Yèche, and D. G. York. Baryon acoustic oscillations in the Ly$\alpha$ forest of BOSS quasars. *A&A*, 552:A96, April 2013. doi: 10.1051/0004-6361/201220724.

D. J. R. Campbell, C. M. Baugh, P. D. Mitchell, J. C. Helly, V. Gonzalez-Perez, C. G. Lacey, C. d. P. Lagos, V. Simha, and D. J. Farrow. A new methodology to test galaxy formation models

using the dependence of clustering on stellar mass. *MNRAS*, 452:852–871, September 2015. doi: 10.1093/mnras/stv1315.

C. L. Carilli, F. Bertoldi, K. M. Menten, M. P. Rupen, E. Kreysa, X. Fan, M. A. Strauss, D. P. Schneider, A. Bertarini, M. S. Yun, and R. Zylka. Dust Emission from High-Redshift QSOS. *ApJ Lett.*, 533:L13–L16, April 2000. doi: 10.1086/312588.

C.-T. J. Chen, R. C. Hickox, S. Alberts, M. Brodwin, C. Jones, S. S. Murray, D. M. Alexander, R. J. Assef, M. J. I. Brown, A. Dey, W. R. Forman, V. Gorjian, A. D. Goulding, E. Le Floc'h, B. T. Jannuzi, J. R. Mullaney, and A. Pope. A Correlation between Star Formation Rate and Average Black Hole Accretion in Star-forming Galaxies. *Astrophys. J.*, 773:3, August 2013. doi: 10.1088/0004-637X/773/1/3.

C. G. Christensen. Luminosity function of nearby galaxies. *A J*, 80:282, April 1975. doi: 10.1086/111743.

J. J. Condon. Cosmological evolution of radio sources. *Astrophys. J.*, 287:461–474, December 1984. doi: 10.1086/162705.

J. J. Condon, Z.-P. Huang, Q. F. Yin, and T. X. Thuan. Compact Starbursts in Ultraluminous Infrared Galaxies. In A. V. Filippenko, editor, *Relationships Between Active Galactic Nuclei and Starburst Galaxies*, volume 31 of *Astronomical Society of the Pacific Conference Series*, page 79, 1992.

J. J. Condon, W. D. Cotton, E. W. Greisen, Q. F. Yin, R. A. Perley, and J. J. Broderick. The NRAO VLA Sky Survey. In D. R. Crabtree, R. J. Hanisch, and J. Barnes, editors, *Astronomical Data Analysis Software and Systems III*, volume 61 of *Astronomical Society of the Pacific Conference Series*, page 155, 1994.

J. J. Condon, W. D. Cotton, E. W. Greisen, Q. F. Yin, R. A. Perley, G. B. Taylor, and J. J. Broderick. The NRAO VLA Sky Survey. *A J*, 115:1693–1716, May 1998. doi: 10.1086/300337.

J. J. Condon, W. D. Cotton, Q. F. Yin, D. L. Shupe, L. J. Storrie-Lombardi, G. Helou, B. T. Soifer, and M. W. Werner. The SIRTF First-Look Survey. I. VLA Image and Source Catalog. *A J*, 125: 2411–2426, May 2003. doi: 10.1086/374633.

J. J. Condon, W. D. Cotton, E. B. Fomalont, K. I. Kellermann, N. Miller, R. A. Perley, D. Scott, T. Vernstrom, and J. V. Wall. Resolving the Radio Source Background: Deeper Understanding through Confusion. *Astrophys. J.*, 758:23, October 2012. doi: 10.1088/0004-637X/758/1/23.

J. J. Condon, K. I. Kellermann, A. E. Kimball, Ž. Ivezić, and R. A. Perley. Active Galactic Nucleus and Starburst Radio Emission from Optically Selected Quasi-stellar Objects. *Astrophys. J.*, 768: 37, May 2013. doi: 10.1088/0004-637X/768/1/37.

JamesJ. Condon. Radio sources and cosmology. In GerritL. Verschuur and KennethI. Kellermann, editors, *Galactic and Extragalactic Radio Astronomy*, Astronomy and Astrophysics Library, pages 641–678. Springer New York, 1988. doi: 10.1007/978-1-4612-3936-9_15. URL http://dx.doi.org/10.1007/978-1-4612-3936-9_15.

D. F. Crawford, D. L. Jauncey, and H. S. Murdoch. Maximum-Likelihood Estimation of the Slope from Number-Flux Counts of Radio Sources. *Astrophys. J.*, 162:405, November 1970. doi: 10.1086/150672.

S. M. Croom, R. J. Smith, B. J. Boyle, T. Shanks, L. Miller, P. J. Outram, and N. S. Loaring. The 2dF QSO Redshift Survey - XII. The spectroscopic catalogue and luminosity function. *MNRAS*, 349:1397–1418, April 2004. doi: 10.1111/j.1365-2966.2004.07619.x.

S. M. Croom, G. T. Richards, T. Shanks, B. J. Boyle, R. G. Sharp, J. Bland-Hawthorn, T. Bridges, R. J. Brunner, R. Cannon, D. Carson, K. Chiu, M. Colless, W. Couch, R. de Propris, M. J. Drinkwater, A. Edge, S. Fine, J. Loveday, L. Miller, A. D. Myers, R. C. Nichol, P. Outram, K. Pimbblet, I. Roseboom, N. Ross, D. P. Schneider, A. Smith, C. Stoughton, M. A. Strauss, and D. Wake. The 2dF-SDSS LRG and QSO Survey: the spectroscopic QSO catalogue. *MNRAS*, 392:19–44, January 2009. doi: 10.1111/j.1365-2966.2008.14052.x.

K. S. Dawson, D. J. Schlegel, C. P. Ahn, S. F. Anderson, É. Aubourg, S. Bailey, R. H. Barkhouser, J. E. Bautista, A. Beifiori, A. A. Berlind, V. Bhardwaj, D. Bizyaev, C. H. Blake, M. R. Blanton, M. Blomqvist, A. S. Bolton, A. Borde, J. Bovy, W. N. Brandt, H. Brewington, J. Brinkmann, P. J. Brown, J. R. Brownstein, K. Bundy, N. G. Busca, W. Carithers, A. R. Carnero, M. A. Carr, Y. Chen, J. Comparat, N. Connolly, F. Cope, R. A. C. Croft, A. J. Cuesta, L. N. da Costa, J. R. A. Davenport, T. Delubac, R. de Putter, S. Dhital, A. Ealet, G. L. Ebelke, D. J. Eisenstein, S. Escoffier, X. Fan, N. Filiz Ak, H. Finley, A. Font-Ribera, R. Génova-Santos, J. E. Gunn, H. Guo, D. Haggard, P. B. Hall, J.-C. Hamilton, B. Harris, D. W. Harris, S. Ho, D. W. Hogg, D. Holder, K. Honscheid, J. Huehnerhoff, B. Jordan, W. P. Jordan, G. Kauffmann, E. A. Kazin, D. Kirkby, M. A. Klaene, J.-P. Kneib, J.-M. Le Goff, K.-G. Lee, D. C. Long, C. P. Loomis, B. Lundgren, R. H. Lupton, M. A. G. Maia, M. Makler, E. Malanushenko, V. Malanushenko, R. Mandelbaum, M. Manera, C. Maraston, D. Margala, K. L. Masters, C. K. McBride, P. McDonald, I. D. McGreer, R. G. McMahon, O. Mena, J. Miralda-Escudé, A. D. Montero-Dorta, F. Montesano, D. Muna, A. D. Myers, T. Naugle, R. C. Nichol, P. Noterdaeme, S. E. Nuza, M. D. Olmstead, A. Oravetz, D. J. Oravetz, R. Owen, N. Padmanabhan, N. Palanque-Delabrouille, K. Pan, J. K. Parejko, I. Pâris, W. J. Percival, I. Pérez-Fournon, I. Pérez-Ràfols, P. Petitjean, R. Pfaffenberger, J. Pforr, M. M. Pieri, F. Prada, A. M. Price-Whelan, M. J. Raddick, R. Rebolo, J. Rich, G. T. Richards, C. M. Rockosi, N. A. Roe, A. J. Ross, N. P. Ross, G. Rossi, J. A. Rubiño-Martin, L. Samushia, A. G. Sánchez, C. Sayres, S. J. Schmidt, D. P. Schneider, C. G. Scóccola, H.-J. Seo, A. Shelden, E. Sheldon, Y. Shen, Y. Shu, A. Slosar, S. A. Smee, S. A. Snedden, F. Stauffer, O. Steele, M. A. Strauss, A. Streblyanska, N. Suzuki, M. E. C. Swanson, T. Tal, M. Tanaka, D. Thomas,

J. L. Tinker, R. Tojeiro, C. A. Tremonti, M. Vargas Magaña, L. Verde, M. Viel, D. A. Wake, M. Watson, B. A. Weaver, D. H. Weinberg, B. J. Weiner, A. A. West, M. White, W. M. Wood-Vasey, C. Yeche, I. Zehavi, G.-B. Zhao, and Z. Zheng. The Baryon Oscillation Spectroscopic Survey of SDSS-III. *A J*, 145:10, January 2013. doi: 10.1088/0004-6256/145/1/10.

A. De Rosa, F. Panessa, L. Basani, A. Bazzano, A. J. Bird, R. Landi, A. Malizia, M. Molina, and P. Ubertini. Broadband X-ray properties of absorbed AGN observed with INTEGRAL and XMM. In *Extreme and Variable High Energy Sky (Extremesky 2011)*, page 45, 2011.

H. R. de Ruiter, G. Zamorani, P. Parma, G. Hasinger, G. Hartner, J. Truemper, R. Burg, R. Giacconi, and M. Schmidt. Deep radio observations of the "Lockman Hole". *A&A*, 319:7–17, March 1997.

M. Dotti, M. Colpi, S. Pallini, A. Perego, and M. Volonteri. On the Orientation and Magnitude of the Black Hole Spin in Galactic Nuclei. *Astrophys. J.*, 762:68, January 2013. doi: 10.1088/0004-637X/762/2/68.

S. P. Driver, D. T. Hill, L. S. Kelvin, A. S. G. Robotham, J. Liske, P. Norberg, I. K. Baldry, S. P. Bamford, A. M. Hopkins, J. Loveday, J. A. Peacock, E. Andrae, J. Bland-Hawthorn, S. Brough, M. J. I. Brown, E. Cameron, J. H. Y. Ching, M. Colless, C. J. Conselice, S. M. Croom, N. J. G. Cross, R. de Propris, S. Dye, M. J. Drinkwater, S. Ellis, A. W. Graham, M. W. Grootes, M. Gunawardhana, D. H. Jones, E. van Kampen, C. Maraston, R. C. Nichol, H. R. Parkinson, S. Phillipps, K. Pimbblet, C. C. Popescu, M. Prescott, I. G. Roseboom, E. M. Sadler, A. E. Sansom, R. G. Sharp, D. J. B. Smith, E. Taylor, D. Thomas, R. J. Tuffs, D. Wijesinghe, L. Dunne, C. S. Frenk, M. J. Jarvis, B. F. Madore, M. J. Meyer, M. Seibert, L. Staveley-Smith, W. J. Sutherland, and S. J. Warren. Galaxy and Mass Assembly (GAMA): survey diagnostics and core data release. *MNRAS*, 413:971–995, May 2011. doi: 10.1111/j.1365-2966.2010.18188.x.

J. S. Dunlop, R. J. McLure, M. J. Kukula, S. A. Baum, C. P. O'Dea, and D. H. Hughes. Quasars, their host galaxies and their central black holes. *MNRAS*, 340:1095–1135, April 2003. doi: 10.1046/j.1365-8711.2003.06333.x.

L. Dunne, R. J. Ivison, S. Maddox, M. Cirasuolo, A. M. Mortier, S. Foucaud, E. Ibar, O. Almaini, C. Simpson, and R. McLure. The star formation history of K-selected galaxies. *MNRAS*, 394:3–20, March 2009. doi: 10.1111/j.1365-2966.2008.13900.x.

D. J. Eisenstein, J. Annis, J. E. Gunn, A. S. Szalay, A. J. Connolly, R. C. Nichol, N. A. Bahcall, M. Bernardi, S. Burles, F. J. Castander, M. Fukugita, D. W. Hogg, Ž. Ivezić, G. R. Knapp, R. H. Lupton, V. Narayanan, M. Postman, D. E. Reichart, M. Richmond, D. P. Schneider, D. J. Schlegel, M. A. Strauss, M. SubbaRao, D. L. Tucker, D. Vanden Berk, M. S. Vogeley, D. H. Weinberg, and B. Yanny. Spectroscopic Target Selection for the Sloan Digital Sky Survey: The Luminous Red Galaxy Sample. *A J*, 122:2267–2280, November 2001. doi: 10.1086/323717.

D. J. Eisenstein, D. H. Weinberg, E. Agol, H. Aihara, C. Allende Prieto, S. F. Anderson, J. A. Arns, É. Aubourg, S. Bailey, E. Balbinot, and et al. SDSS-III: Massive Spectroscopic Surveys of the Distant Universe, the Milky Way, and Extra-Solar Planetary Systems. *A J*, 142:72, September 2011. doi: 10.1088/0004-6256/142/3/72.

F. R. Elder, A. M. Gurewitsch, R. V. Langmuir, and H. C. Pollock. Radiation from Electrons in a Synchrotron. *Physical Review*, 71:829–830, June 1947. doi: 10.1103/PhysRev.71.829.5.

S. L. Ellison, A. Songaila, J. Schaye, and M. Pettini. The Enrichment History of the Intergalactic Medium-Measuring the C IV/H I Ratio in the Lyα Forest. *A J*, 120:1175–1191, September 2000. doi: 10.1086/301511.

B. G. Elmegreen. The Initial Stellar Mass Function from Random Sampling in a Turbulent Fractal Cloud. *Astrophys. J.*, 486:944–954, September 1997.

D. Fabricant, R. Fata, J. Roll, E. Hertz, N. Caldwell, T. Gauron, J. Geary, B. McLeod, A. Szentgyorgyi, J. Zajac, M. Kurtz, J. Barberis, H. Bergner, W. Brown, M. Conroy, R. Eng, M. Geller, R. Goddard, M. Honsa, M. Mueller, D. Mink, M. Ordway, S. Tokarz, D. Woods, W. Wyatt, H. Epps, and I. Dell'Antonio. Hectospec, the MMT's 300 Optical Fiber-Fed Spectrograph. *PASP*, 117: 1411–1434, December 2005. doi: 10.1086/497385.

D. Fadda, B. T. Jannuzi, A. Ford, and L. J. Storrie-Lombardi. The Spitzer Space Telescope First-Look Survey: KPNO Mosaic-1 R-Band Images and Source Catalogs. *A J*, 128:1–15, July 2004. doi: 10.1086/421366.

X. Fan. Simulation of Stellar Objects in SDSS Color Space. *A J*, 117:2528–2551, May 1999. doi: 10.1086/300848.

X. Fan, J. F. Hennawi, G. T. Richards, M. A. Strauss, D. P. Schneider, J. L. Donley, J. E. Young, J. Annis, H. Lin, H. Lampeitl, R. H. Lupton, J. E. Gunn, G. R. Knapp, W. N. Brandt, S. Anderson, N. A. Bahcall, J. Brinkmann, R. J. Brunner, M. Fukugita, A. S. Szalay, G. P. Szokoly, and D. G. York. A Survey of z5.7 Quasars in the Sloan Digital Sky Survey. III. Discovery of Five Additional Quasars. *A J*, 128:515–522, August 2004. doi: 10.1086/422434.

B. L. Fanaroff and J. M. Riley. The morphology of extragalactic radio sources of high and low luminosity. *MNRAS*, 167:31P–36P, May 1974. doi: 10.1093/mnras/167.1.31P.

N. Fanidakis, C. M. Baugh, A. J. Benson, R. G. Bower, S. Cole, C. Done, and C. S. Frenk. Grand unification of AGN activity in the ΛCDM cosmology. *MNRAS*, 410:53–74, January 2011. doi: 10.1111/j.1365-2966.2010.17427.x.

J. E. Felten. Study of the luminosity function for field galaxies. *A J*, 82:861–878, November 1977. doi: 10.1086/112140.

A. Feoli and L. Mancini. A Hertzsprung-Russell-like Diagram for Galaxies: The M $_{\text{ffl}}$ Versus M $_G\sigma^2$ Relation. *Astrophys. J.*, 703:1502–1510, October 2009. doi: 10.1088/0004-637X/703/2/1502.

F. Feroz, M. P. Hobson, and M. Bridges. MULTINEST: an efficient and robust Bayesian inference tool for cosmology and particle physics. *MNRAS*, 398:1601–1614, October 2009a. doi: 10.1111/j.1365-2966.2009.14548.x.

F. Feroz, M. P. Hobson, J. T. L. Zwart, R. D. E. Saunders, and K. J. B. Grainge. Bayesian modelling of clusters of galaxies from multifrequency-pointed Sunyaev-Zel'dovich observations. *MNRAS*, 398:2049–2060, October 2009b. doi: 10.1111/j.1365-2966.2009.15247.x.

L. Ferrarese and D. Merritt. A Fundamental Relation between Supermassive Black Holes and Their Host Galaxies. *ApJ Lett.*, 539:L9–L12, August 2000. doi: 10.1086/312838.

E. B. Fomalont, K. I. Kellermann, L. L. Cowie, P. Capak, A. J. Barger, R. B. Partridge, R. A. Windhorst, and E. A. Richards. The Radio/Optical Catalog of the SSA 13 Field. *ApJ Suppl.*, 167:103–160, December 2006. doi: 10.1086/508169.

J. A. Frieman, B. Bassett, A. Becker, C. Choi, D. Cinabro, F. DeJongh, D. L. Depoy, B. Dilday, M. Doi, P. M. Garnavich, C. J. Hogan, J. Holtzman, M. Im, S. Jha, R. Kessler, K. Konishi, H. Lampeitl, J. Marriner, J. L. Marshall, D. McGinnis, G. Miknaitis, R. C. Nichol, J. L. Prieto, A. G. Riess, M. W. Richmond, R. Romani, M. Sako, D. P. Schneider, M. Smith, N. Takanashi, K. Tokita, K. van der Heyden, N. Yasuda, C. Zheng, J. Adelman-McCarthy, J. Annis, R. J. Assef, J. Barentine, R. Bender, R. D. Blandford, W. N. Boroski, M. Bremer, H. Brewington, C. A. Collins, A. Crotts, J. Dembicky, J. Eastman, A. Edge, E. Edmondson, E. Elson, M. E. Eyler, A. V. Filippenko, R. J. Foley, S. Frank, A. Goobar, T. Gueth, J. E. Gunn, M. Harvanek, U. Hopp, Y. Ihara, Ž. Ivezić, S. Kahn, J. Kaplan, S. Kent, W. Ketzeback, S. J. Kleinman, W. Kollatschny, R. G. Kron, J. Krzesiński, D. Lamenti, G. Leloudas, H. Lin, D. C. Long, J. Lucey, R. H. Lupton, E. Malanushenko, V. Malanushenko, R. J. McMillan, J. Mendez, C. W. Morgan, T. Morokuma, A. Nitta, L. Ostman, K. Pan, C. M. Rockosi, A. K. Romer, P. Ruiz-Lapuente, G. Saurage, K. Schlesinger, S. A. Snedden, J. Sollerman, C. Stoughton, M. Stritzinger, M. Subba Rao, D. Tucker, P. Vaisanen, L. C. Watson, S. Watters, J. C. Wheeler, B. Yanny, and D. York. The Sloan Digital Sky Survey-II Supernova Survey: Technical Summary. *A J*, 135:338–347, January 2008. doi: 10.1088/0004-6256/135/1/338.

M. Fukugita, T. Ichikawa, J. E. Gunn, M. Doi, K. Shimasaku, and D. P. Schneider. The Sloan Digital Sky Survey Photometric System. *A J*, 111:1748, April 1996. doi: 10.1086/117915.

K. Gebhardt, R. Bender, G. Bower, A. Dressler, S. M. Faber, A. V. Filippenko, R. Green, C. Grillmair, L. C. Ho, J. Kormendy, T. R. Lauer, J. Magorrian, J. Pinkney, D. Richstone, and S. Tremaine. A Relationship between Nuclear Black Hole Mass and Galaxy Velocity Dispersion. *ApJ Lett.*, 539: L13–L16, August 2000. doi: 10.1086/312840.

E. Glikman, D. J. Helfand, R. L. White, R. H. Becker, M. D. Gregg, and M. Lacy. The FIRST-2MASS Red Quasar Survey. *Astrophys. J.*, 667:673–703, October 2007. doi: 10.1086/521073.

A. G. Gray and A. W. Moore. in Proc. Third SIAM International Conf. on Data Mining, ed. D. Barbara & C. Kamath (Philadelphia, PA: SIAM), 203. *Heidelberg:Physica-Verlag*, 845, January 2003. doi: None.

J. E. Greene, L. C. Ho, and A. J. Barth. Black Holes in Pseudobulges and Spheroidals: A Change in the Black Hole-Bulge Scaling Relations at Low Mass. *Astrophys. J.*, 688:159–179, November 2008. doi: 10.1086/592078.

M. D. Gregg, M. Lacy, R. L. White, E. Glikman, D. Helfand, R. H. Becker, and M. S. Brotherton. The Reddest Quasars. *Astrophys. J.*, 564:133–142, January 2002. doi: 10.1086/324145.

A. B. Grishanin, A. V. Titov, and A. S. Yarov. Formation of the synchrotron radiation continuum. *Nuclear Instruments and Methods in Physics Research A*, 308:120–123, October 1991. doi: 10. 1016/0168-9002(91)90607-R.

C. Gruppioni, F. Pozzi, G. Zamorani, P. Ciliegi, C. Lari, E. Calabrese, F. La Franca, and I. Matute. The radio-mid-infrared correlation and the contribution of 15-$\mu$m galaxies to the 1.4-GHz source counts. *MNRAS*, 341:L1–L6, May 2003. doi: 10.1046/j.1365-8711.2003.06601.x.

G. Guglielmino, I. Prandoni, R. Morganti, G. Heald, E. Mahony, and I. van Bemmel. The Lockman Hole Project: A Multi-frequency Study of the Faint Radio Population down to LOFAR bands. In A. M. Mickaelian and D. B. Sanders, editors, *IAU Symposium*, volume 304 of *IAU Symposium*, pages 108–109, July 2014. doi: 10.1017/S1743921314003494.

J. E. Gunn, W. A. Siegmund, E. J. Mannery, R. E. Owen, C. L. Hull, R. F. Leger, L. N. Carey, G. R. Knapp, D. G. York, W. N. Boroski, S. M. Kent, R. H. Lupton, C. M. Rockosi, M. L. Evans, P. Waddell, J. E. Anderson, J. Annis, J. C. Barentine, L. M. Bartoszek, S. Bastian, S. B. Bracker, H. J. Brewington, C. I. Briegel, J. Brinkmann, Y. J. Brown, M. A. Carr, P. C. Czarapata, C. C. Drennan, T. Dombeck, G. R. Federwitz, B. A. Gillespie, C. Gonzales, S. U. Hansen, M. Harvanek, J. Hayes, W. Jordan, E. Kinney, M. Klaene, S. J. Kleinman, R. G. Kron, J. Kresinski, G. Lee, S. Limmongkol, C. W. Lindenmeyer, D. C. Long, C. L. Loomis, P. M. McGehee, P. M. Mantsch, E. H. Neilsen, Jr., R. M. Neswold, P. R. Newman, A. Nitta, J. Peoples, Jr., J. R. Pier, P. S. Prieto, A. Prosapio, C. Rivetta, D. P. Schneider, S. Snedden, and S.-i. Wang. The 2.5 m Telescope of the Sloan Digital Sky Survey. *A J*, 131:2332–2359, April 2006. doi: 10.1086/500975.

A. H. Guth and K. Jagannathan. The Inflationary Universe: The Quest for a New Theory of Cosmic Origins. *American Journal of Physics*, 66:94–95, January 1998. doi: 10.1119/1.18814.

L. Guzzo, M. Scodeggio, B. Garilli, B. R. Granett, A. Fritz, U. Abbas, C. Adami, S. Arnouts, J. Bel, M. Bolzonella, D. Bottini, E. Branchini, A. Cappi, J. Coupon, O. Cucciati, I. Davidzon, G. De

Lucia, S. de la Torre, P. Franzetti, M. Fumana, P. Hudelot, O. Ilbert, A. Iovino, J. Krywult, V. Le Brun, O. Le Fèvre, D. Maccagni, K. Małek, F. Marulli, H. J. McCracken, L. Paioro, J. A. Peacock, M. Polletta, A. Pollo, H. Schlagenhaufer, L. A. M. Tasca, R. Tojeiro, D. Vergani, G. Zamorani, A. Zanichelli, A. Burden, C. Di Porto, A. Marchetti, C. Marinoni, Y. Mellier, L. Moscardini, R. C. Nichol, W. J. Percival, S. Phleps, and M. Wolk. The VIMOS Public Extragalactic Redshift Survey (VIPERS). An unprecedented view of galaxies and large-scale structure at 0.5  z  1.2. *A&A*, 566:A108, June 2014. doi: 10.1051/0004-6361/201321489.

M. J. Hardcastle. Jets, hotspots and lobes: what X-ray observations tell us about extragalactic radio sources. *Philosophical Transactions of the Royal Society of London Series A*, 363:2711–2727, December 2005. doi: 10.1098/rsta.2005.1667.

C. M. Harrison, D. M. Alexander, J. R. Mullaney, and A. M. Swinbank. Kiloparsec-scale outflows are prevalent among luminous AGN: outflows and feedback in the context of the overall AGN population. *MNRAS*, 441:3306–3347, July 2014. doi: 10.1093/mnras/stu515.

S. W. Hawking and G. F. R. Ellis. *The large-scale structure of space-time.* 1973.

C. Hazard, M. B. Mackey, and A. J. Shimmins. Investigation of the Radio Source 3C 273 By The Method of Lunar Occultations. *Nature*, 197:1037–1039, March 1963. doi: 10.1038/1971037a0.

G. Helou, B. T. Soifer, and M. Rowan-Robinson. Thermal infrared and nonthermal radio - Remarkable correlation in disks of galaxies. *ApJ Lett.*, 298:L7–L11, November 1985. doi: 10.1086/184556.

M. A. Hendry and J. F. L. Simmons. Bias of cosmological distance estimators. *A&A*, 237:275–282, October 1990.

J. A. Hodge, R. H. Becker, R. L. White, and W. H. de Vries. Radio Detection of Radio-Quiet Galaxies. *A J*, 136:1097–1109, September 2008. doi: 10.1088/0004-6256/136/3/1097.

J. Holt, C. R. Benn, M. Vigotti, M. Pedani, R. Carballo, J. I. González-Serrano, K.-H. Mack, and B. García. A sample of radio-loud QSOs at redshift ˜ 4. *MNRAS*, 348:857–865, March 2004. doi: 10.1111/j.1365-2966.2004.07423.x.

E. J. Hooper, C. D. Impey, C. B. Foltz, and P. C. Hewett. The Radio Properties of Optically Selected Quasars. III. Comparison between Optical and X-Ray Selected Samples. *Astrophys. J.*, 473:746, December 1996. doi: 10.1086/178186.

A. M. Hopkins, J. Afonso, B. Chan, L. E. Cram, A. Georgakakis, and B. Mobasher. The Phoenix Deep Survey: The 1.4 GHz Microjansky Catalog. *A J*, 125:465–477, February 2003. doi: 10.1086/345974.

E. P. Hubble. NGC 6822, a remote stellar system. *Astrophys. J.*, 62, December 1925. doi: 10.1086/142943.

E. P. Hubble. A spiral nebula as a stellar system, Messier 31. *Astrophys. J.*, 69, March 1929. doi: 10.1086/143167.

Edwin Hubble, S Rosseland, J. M., and R. C. J. A. Astronomy. (Scientific Books: The Realm of the Nebulae; Theoretical Astrophysics). *Science*, 84:509–510, December 1936. doi: 10.1126/science. 84.2188.509.

M. T. Huynh, C. A. Jackson, R. P. Norris, and I. Prandoni. Radio Observations of the Hubble Deep Field-South Region. II. The 1.4 GHz Catalog and Source Counts. *A J*, 130:1373–1388, October 2005. doi: 10.1086/432873.

E. Ibar, R. J. Ivison, A. D. Biggs, D. V. Lal, P. N. Best, and D. A. Green. Deep multi-frequency radio imaging in the Lockman Hole using the GMRT and VLA - I. The nature of the sub-mJy radio population. *MNRAS*, 397:281–298, July 2009. doi: 10.1111/j.1365-2966.2009.14866.x.

Ž. Ivezić, R. H. Becker, M. Blanton, X. Fan, K. Finlator, J. E. Gunn, P. Hall, R. S. J. Kim, G. R. Knapp, J. Loveday, R. H. Lupton, K. Menou, V. Narayanan, G. R. Richards, C. M. Rockosi, D. Schlegel, D. P. Schneider, I. Strateva, M. A. Strauss, D. vanden Berk, W. Voges, B. Yanny, and SDSS Collaboration. The Optical, Infrared and Radio Properties of Extragalactic Sources Observed by SDSS, 2MASS and FIRST Surveys. In R. F. Green, E. Y. Khachikian, and D. B. Sanders, editors, *IAU Colloq. 184: AGN Surveys*, volume 284 of *Astronomical Society of the Pacific Conference Series*, page 137, 2002.

Knud Jahnke and Andrea V. Macciò. The non-causal origin of the black-hole-galaxy scaling relations. *The Astrophysical Journal*, 734(2):92, 2011. URL http://stacks.iop.org/0004-637X/734/i= 2/a=92.

M. J. Jarvis and S. Rawlings. The accretion history of the universe with the SKA. , 48:1173–1185, December 2004. doi: 10.1016/j.newar.2004.09.006.

D. L. Jauncey. Re-examination of the Source Counts for the 3C Revised Catalogue. *Nature*, 216: 877–878, December 1967. doi: 10.1038/216877a0.

H. Jeffreys. *Theory of Probability*. 1961.

L. Jiang, X. Fan, W. N. Brandt, C. L. Carilli, E. Egami, D. C. Hines, J. D. Kurk, G. T. Richards, Y. Shen, M. A. Strauss, M. Vestergaard, and F. Walter. Dust-free quasars in the early Universe. *Nature*, 464:380–383, March 2010. doi: 10.1038/nature08877.

R. Johnston. Shedding light on the galaxy luminosity function. *Astronomy & Astrophysics Review*, 19:41, August 2011. doi: 10.1007/s00159-011-0041-9.

E. Kalfountzou, J. A. Stevens, M. J. Jarvis, M. J. Hardcastle, D. J. B. Smith, N. Bourne, L. Dunne, E. Ibar, S. Eales, R. J. Ivison, S. Maddox, M. W. L. Smith, E. Valiante, and G. de Zotti. Herschel-ATLAS: far-infrared properties of radio-loud and radio-quiet quasars. *MNRAS*, 442:1181–1196, August 2014. doi: 10.1093/mnras/stu782.

A. Karim, E. Schinnerer, A. Martínez-Sansigre, M. T. Sargent, A. van der Wel, H.-W. Rix, O. Ilbert, V. Smolčić, C. Carilli, M. Pannella, A. M. Koekemoer, E. F. Bell, and M. Salvato. The Star Formation History of Mass-selected Galaxies in the COSMOS Field. *Astrophys. J.*, 730:61, April 2011. doi: 10.1088/0004-637X/730/2/61.

K. I. Kellermann, R. Sramek, M. Schmidt, D. B. Shaffer, and R. Green. VLA observations of objects in the Palomar Bright Quasar Survey. *A J*, 98:1195–1207, October 1989. doi: 10.1086/115207.

K. I. Kellermann, E. B. Fomalont, V. Mainieri, P. Padovani, P. Rosati, P. Shaver, P. Tozzi, and N. Miller. The VLA Survey of the Chandra Deep Field-South. I. Overview and the Radio Data. *ApJ Suppl.*, 179:71–94, November 2008. doi: 10.1086/591055.

A. E. Kimball, K. I. Kellermann, J. J. Condon, Ž. Ivezić, and R. A. Perley. The Two-component Radio Luminosity Function of Quasi-stellar Objects: Star Formation and Active Galactic Nucleus. *ApJ Lett.*, 739:29, September 2011a. doi: 10.1088/2041-8205/739/1/L29.

A. E. Kimball, K. I. Kellermann, J. J. Condon, Ž. Ivezić, and R. A. Perley. The Two-component Radio Luminosity Function of Quasi-stellar Objects: Star Formation and Active Galactic Nucleus. *ApJ Lett.*, 739:29, September 2011b. doi: 10.1088/2041-8205/739/1/L29.

D. Kirkby and BOSS Collaboration. Baryon Acoustic Oscillations in the Lyman-alpha Forest of BOSS Quasars. In *American Astronomical Society Meeting Abstracts #221*, volume 221 of *American Astronomical Society Meeting Abstracts*, page 402.03, January 2013.

J. A. Kirkpatrick, D. J. Schlegel, N. P. Ross, A. D. Myers, J. F. Hennawi, E. S. Sheldon, D. P. Schneider, and B. A. Weaver. A Simple Likelihood Method for Quasar Target Selection. *Astrophys. J.*, 743: 125, December 2011. doi: 10.1088/0004-637X/743/2/125.

J. Kormendy and D. Richstone. Inward Bound—The Search For Supermassive Black Holes In Galactic Nuclei. *ARA&A*, 33:581, 1995. doi: 10.1146/annurev.aa.33.090195.003053.

J. H. Krolik. *Active galactic nuclei : from the central black hole to the galactic environment.* 1999.

R. G. Kron. Observations of Galaxies at High Redshift. In *Bulletin of the American Astronomical Society*, volume 17 of *Bulletin of the American Astronomical Society*, page 605, March 1985.

C. Lacey and S. Cole. Merger rates in hierarchical models of galaxy formation. *MNRAS*, 262:627–649, June 1993. doi: 10.1093/mnras/262.3.627.

M. Lacy, S. A. Laurent-Muehleisen, S. E. Ridgway, R. H. Becker, and R. L. White. The Radio Luminosity-Black Hole Mass Correlation for Quasars from the FIRST Bright Quasar Survey and a "Unification Scheme" for Radio-loud and Radio-quiet Quasars. *ApJ Lett.*, 551:L17–L21, April 2001. doi: 10.1086/319836.

D. V. Lal and L. C. Ho. The Radio Properties of Type 2 Quasars. *A J*, 139:1089–1105, March 2010. doi: 10.1088/0004-6256/139/3/1089.

J. P. Leahy and R. A. Perley. VLA images of 23 extragalactic radio sources. *A J*, 102:537–561, August 1991. doi: 10.1086/115892.

G. Lemaître. Un Univers homogène de masse constante et de rayon croissant rendant compte de la vitesse radiale des nébuleuses extra-galactiques. *Annales de la Société Scientifique de Bruxelles*, 47:49–59, 1927.

R. R. Lindner. *The growth of massive galaxies and clusters at high redshift.* PhD thesis, Rutgers The State University of New Jersey - New Brunswick, 2013.

M. S. Longair. On the interpretation of radio source counts. *MNRAS*, 133:421, 1966. doi: 10.1093/mnras/133.4.421.

M. S. Longair. Radio astronomy and cosmology. In A. Maeder, L. Martinet, and G. Tammann, editors, *Saas-Fee Advanced Course 8: Observational Cosmology Advanced Course*, page 125, 1978.

D. Lynden-Bell. A method of allowing for known observational selection in small samples applied to 3CR quasars. *MNRAS*, 155:95, 1971. doi: 10.1093/mnras/155.1.95.

R. Lynds. The Absorption-Line Spectrum of 4c 05.34. *ApJ Lett.*, 164:L73, March 1971. doi: 10.1086/180695.

W. Mattig. Über den Zusammenhang zwischen Rotverschiebung und scheinbarer Helligkeit. *Astronomische Nachrichten*, 284:109, May 1958.

I. D. McGreer, D. J. Helfand, and R. L. White. Radio-Selected Quasars in the Sloan Digital Sky Survey. *A J*, 138:1925–1937, December 2009. doi: 10.1088/0004-6256/138/6/1925.

L. Miller, J. A. Peacock, and A. R. G. Mead. The bimodal radio luminosity function of quasars. *MNRAS*, 244:207–213, May 1990.

K. J. Mitchell and J. J. Condon. A confusion-limited 1.49-GHz VLA survey centered on alpha = 13 H 00 M 37 s, delta = + 30 deg 34 arcmin. *A J*, 90:1957–1966, October 1985. doi: 10.1086/113899.

K. Mitchell-Wynne, M. G. Santos, J. Afonso, and M. J. Jarvis. Beyond stacking: a maximum-likelihood method to constrain radio source counts below the detection threshold. *MNRAS*, 437:2270–2278, January 2014. doi: 10.1093/mnras/stt2035.

E. Momjian, C. L. Carilli, F. Walter, and B. Venemans. The Highest Redshift Quasar at z = 7.085: A Radio-quiet Source. *A J*, 147:6, January 2014. doi: 10.1088/0004-6256/147/1/6.

R. Morganti, J. Fogasy, Z. Paragi, T. Oosterloo, and M. Orienti. Radio Jets Clearing the Way Through a Galaxy: Watching Feedback in Action. *Science*, 341:1082–1085, September 2013. doi: 10.1126/science.1240436.

S. L. Morris, R. J. Weymann, S. F. Anderson, P. C. Hewett, P. J. Francis, C. B. Foltz, F. H. Chaffee, and G. M. MacAlpine. The large, bright QSO survey. V - QSOs in three southern fields. *A J*, 102:1627–1658, November 1991. doi: 10.1086/115984.

R. P. Norris, J. Afonso, D. Bacon, R. Beck, M. Bell, R. J. Beswick, P. Best, S. Bhatnagar, A. Bonafede, G. Brunetti, T. Budavári, R. Cassano, J. J. Condon, C. Cress, A. Dabbech, I. Feain, R. Fender, C. Ferrari, B. M. Gaensler, G. Giovannini, M. Haverkorn, G. Heald, K. Van der Heyden, A. M. Hopkins, M. Jarvis, M. Johnston-Hollitt, R. Kothes, H. Van Langevelde, J. Lazio, M. Y. Mao, A. Martínez-Sansigre, D. Mary, K. Mcalpine, E. Middelberg, E. Murphy, P. Padovani, Z. Paragi, I. Prandoni, A. Raccanelli, E. Rigby, I. G. Roseboom, H. Röttgering, J. Sabater, M. Salvato, A. M. M. Scaife, R. Schilizzi, N. Seymour, D. J. B. Smith, G. Umana, G.-B. Zhao, and P.-C. Zinn. Radio Continuum Surveys with Square Kilometre Array Pathfinders. *PASA*, 30:e020, March 2013. doi: 10.1017/pas.2012.020.

J. B. Oke. Absolute Energy Distribution in the Optical Spectrum of 3C 273. *Nature*, 197:1040–1041, March 1963. doi: 10.1038/1971040b0.

F. N. Owen and G. E. Morrison. The Deep Swire Field. I. 20 cm Continuum Radio Observations: A Crowded Sky. *A J*, 136:1889–1900, November 2008. doi: 10.1088/0004-6256/136/5/1889.

P. Padovani, P. Giommi, and F. Fiore. Are the X-ray spectra of flat-spectrum radio quasars and BL Lacertae objects different? *MNRAS*, 284:569–575, January 1997. doi: 10.1093/mnras/284.3.569.

P. Padovani, N. Miller, K. I. Kellermann, V. Mainieri, P. Rosati, and P. Tozzi. The VLA Survey of Chandra Deep Field South. V. Evolution and Luminosity Functions of Sub-millijansky Radio Sources and the Issue of Radio Emission in Radio-quiet Active Galactic Nuclei. *Astrophys. J.*, 740:20, October 2011. doi: 10.1088/0004-637X/740/1/20.

P. Padovani, M. Bonzini, N. Miller, K. I. Kellermann, V. Mainieri, P. Rosati, P. Tozzi, and S. Vattakunnel. The AGN content of deep radio surveys and radio emission in radio-quiet AGN. Why every astronomer should care about deep radio fields. In A. M. Mickaelian and D. B. Sanders, editors, *IAU Symposium*, volume 304 of *IAU Symposium*, pages 79–85, July 2014. doi: 10.1017/S1743921314003391.

P. Padovani, M. Bonzini, K. I. Kellermann, N. Miller, V. Mainieri, and P. Tozzi. Radio-faint AGN: a tale of two populations. *MNRAS*, 452:1263–1279, September 2015. doi: 10.1093/mnras/stv1375.

I. Paris, P. Petitjean, E. Aubourg, S. Bailey, N. P. Ross, A. D. Myers, M. A. Strauss, S. F. Anderson, E. Arnau, J. Bautista, D. Bizyaev, A. S. Bolton, J. Bovy, W. N. Brandt, H. Brewington, J. R. Brownstein, N. Busca, D. Capellupo, W. Carithers, R. A. C. Croft, K. Dawson, T. Delubac, G. Ebelke, D. J. Eisenstein, P. Engelke, X. Fan, A. N. Filiz, H. Finley, A. Font-Ribera, J. Ge, R. R. Gibson, P. B. Hall, F. Hamann, J. F. Hennawi, S. Ho, D. W. Hogg, Z. Ivezic, L. Jiang, A. E. Kimball, D. Kirky, J. A. Kirkpatrick, K.-G. Lee, J.-M. Le Goff, B. Lundgren, C. L. MacLeod, E. Malanushenko, V. Malanushenko, C. Maraston, I. D. McGreer, R. G. McMahon, J. Miralda-Escude, D. Muna, P. Noterdaeme, D. Oravetz, N. Palanque-Delabrouille, K. Pan, I. Perez-Fournon, M. M. Pieri, G. T. Richards, E. Rollinde, E. S. Sheldon, D. J. Schlegel, D. P. Schneider, A. Slosar, A. Shelden, Y. Shen, A. Simmons, S. Snedden, N. Suzuki, J. Tinker, M. Viel, B. A. Weaver, D. W. Weinberg, M. White, W. M. Wood-Vasey, and C. Yeche. VizieR Online Data Catalog: SDSS Quasar Catalog, DR9Q (Paris+, 2012). *VizieR Online Data Catalog*, 7269: 0, October 2012.

I. Pâris, P. Petitjean, É. Aubourg, N. P. Ross, A. D. Myers, A. Streblyanska, S. Bailey, P. B. Hall, M. A. Strauss, S. F. Anderson, D. Bizyaev, A. Borde, J. Brinkmann, J. Bovy, W. N. Brandt, H. Brewington, J. R. Brownstein, B. A. Cook, G. Ebelke, X. Fan, N. Filiz Ak, H. Finley, A. Font-Ribera, J. Ge, F. Hamann, S. Ho, L. Jiang, K. Kinemuchi, E. Malanushenko, V. Malanushenko, M. Marchante, I. D. McGreer, R. G. McMahon, J. Miralda-Escudé, D. Muna, P. Noterdaeme, D. Oravetz, N. Palanque-Delabrouille, K. Pan, I. Perez-Fournon, M. Pieri, R. Riffel, D. J. Schlegel, D. P. Schneider, A. Simmons, M. Viel, B. A. Weaver, W. M. Wood-Vasey, C. Yèche, and D. G. York. The Sloan Digital Sky Survey quasar catalog: tenth data release. *A&A*, 563:A54, March 2014. doi: 10.1051/0004-6361/201322691.

P. J. E. Peebles and Bharat Ratra. The cosmological constant and dark energy. *Rev. Mod. Phys.*, 75:559–606, Apr 2003. doi: 10.1103/RevModPhys.75.559. URL http://link.aps.org/doi/10.1103/RevModPhys.75.559.

Y. C. Pei. The luminosity function of quasars. *Astrophys. J.*, 438:623–631, January 1995. doi: 10.1086/175105.

A. A. Penzias and R. W. Wilson. Measurement of the Flux Density of CAS a at 4080 Mc/s. *Astrophys. J.*, 142:1149, October 1965. doi: 10.1086/148384.

R. A. Perley, J. J. Cowan, and J. W. Dreher. Discovery of a Jet and Filaments in Cygnus A. In *Bulletin of the American Astronomical Society*, volume 16 of *Bulletin of the American Astronomical Society*, page 412, January 1984.

S. Perlmutter, G. Aldering, G. Goldhaber, R. A. Knop, P. Nugent, P. G. Castro, S. Deustua, S. Fabbro, A. Goobar, D. E. Groom, I. M. Hook, A. G. Kim, M. Y. Kim, J. C. Lee, N. J. Nunes, R. Pain, C. R. Pennypacker, R. Quimby, C. Lidman, R. S. Ellis, M. Irwin, R. G. McMahon, P. Ruiz-Lapuente, N. Walton, B. Schaefer, B. J. Boyle, A. V. Filippenko, T. Matheson, A. S. Fruchter,

N. Panagia, H. J. M. Newberg, W. J. Couch, and T. S. C. Project. Measurements of $\Omega$ and $\Lambda$ from 42 High-Redshift Supernovae. *Astrophys. J.*, 517:565–586, June 1999. doi: 10.1086/307221.

B. M. Peterson. Emission Lines in Active Galaxies: Outlook for the Future. In B. M. Peterson, F.-Z. Cheng, and A. S. Wilson, editors, *IAU Colloq. 159: Emission Lines in Active Galaxies: New Methods and Techniques*, volume 113 of *Astronomical Society of the Pacific Conference Series*, page 489, 1997.

Planck Collaboration, P. A. R. Ade, N. Aghanim, M. Arnaud, M. Ashdown, J. Aumont, C. Baccigalupi, A. J. Banday, R. B. Barreiro, J. G. Bartlett, and et al. Planck 2015 results. XIII. Cosmological parameters. *ArXiv e-prints*, February 2015.

I. Prandoni, L. Gregorini, P. Parma, H. R. de Ruiter, G. Vettolani, A. Zanichelli, M. H. Wieringa, and R. D. Ekers. The ATESP radio survey. IV. Optical identifications and spectroscopy in the EIS-A region. *A&A*, 369:787–796, April 2001. doi: 10.1051/0004-6361:20010170.

S. Rawlings and R. Saunders. Evidence for a common central-engine mechanism in all extragalactic radio sources. *Nature*, 349:138–140, January 1991. doi: 10.1038/349138a0.

G. T. Richards. AGN Outflows in Emission and Absorption: The SDSS Perspective. *ArXiv Astrophysics e-prints*, March 2006.

G. T. Richards, X. Fan, D. P. Schneider, D. E. Vanden Berk, M. A. Strauss, D. G. York, J. E. Anderson, Jr., S. F. Anderson, J. Annis, N. A. Bahcall, M. Bernardi, J. W. Briggs, J. Brinkmann, R. Brunner, S. Burles, L. Carey, F. J. Castander, A. J. Connolly, J. H. Crocker, I. Csabai, M. Doi, D. Finkbeiner, S. D. Friedman, J. A. Frieman, M. Fukugita, J. E. Gunn, R. B. Hindsley, Ž. Ivezić, S. Kent, G. R. Knapp, D. Q. Lamb, R. F. Leger, D. C. Long, J. Loveday, R. H. Lupton, T. A. McKay, A. Meiksin, A. Merrelli, J. A. Munn, H. J. Newberg, M. Newcomb, R. C. Nichol, R. Owen, J. R. Pier, A. Pope, M. W. Richmond, C. M. Rockosi, D. J. Schlegel, W. A. Siegmund, S. Smee, Y. Snir, C. Stoughton, C. Stubbs, M. SubbaRao, A. S. Szalay, G. P. Szokoly, C. Tremonti, A. Uomoto, P. Waddell, B. Yanny, and W. Zheng. Colors of 2625 Quasars at 0Z5 Measured in the Sloan Digital Sky Survey Photometric System. *A J*, 121:2308–2330, May 2001a. doi: 10.1086/320392.

G. T. Richards, S. A. Laurent-Muehleisen, R. H. Becker, and D. G. York. Quasar Absorption Lines as a Function of Quasar Orientation Measures. *Astrophys. J.*, 547:635–648, February 2001b. doi: 10.1086/318414.

G. T. Richards, X. Fan, H. J. Newberg, M. A. Strauss, D. E. Vanden Berk, D. P. Schneider, B. Yanny, A. Boucher, S. Burles, J. A. Frieman, J. E. Gunn, P. B. Hall, Ž. Ivezić, S. Kent, J. Loveday, R. H. Lupton, C. M. Rockosi, D. J. Schlegel, C. Stoughton, M. SubbaRao, and D. G. York. Spectroscopic Target Selection in the Sloan Digital Sky Survey: The Quasar Sample. *A J*, 123: 2945–2975, June 2002. doi: 10.1086/340187.

G. T. Richards, P. B. Hall, D. E. Vanden Berk, M. A. Strauss, D. P. Schneider, M. A. Weinstein, T. A. Reichard, D. G. York, G. R. Knapp, X. Fan, Ž. Ivezić, J. Brinkmann, T. Budavári, I. Csabai, and R. C. Nichol. Red and Reddened Quasars in the Sloan Digital Sky Survey. *A J*, 126:1131–1147, September 2003. doi: 10.1086/377014.

G. T. Richards, M. A. Strauss, B. Pindor, Z. Haiman, X. Fan, D. Eisenstein, D. P. Schneider, N. A. Bahcall, J. Brinkmann, and R. Brunner. A Snapshot Survey for Gravitational Lenses among z=4.0 Quasars. I. The z5.7 Sample. *A J*, 127:1305–1312, March 2004.

G. T. Richards, R. P. Deo, M. Lacy, A. D. Myers, R. C. Nichol, N. L. Zakamska, R. J. Brunner, W. N. Brandt, A. G. Gray, J. K. Parejko, A. Ptak, D. P. Schneider, L. J. Storrie-Lombardi, and A. S. Szalay. Eight-Dimensional Mid-Infrared/Optical Bayesian Quasar Selection. *A J*, 137:3884–3899, April 2009a. doi: 10.1088/0004-6256/137/4/3884.

G. T. Richards, A. D. Myers, A. G. Gray, R. N. Riegel, R. C. Nichol, R. J. Brunner, A. S. Szalay, D. P. Schneider, and S. F. Anderson. Efficient Photometric Selection of Quasars from the Sloan Digital Sky Survey. II. ~1,000,000 Quasars from Data Release 6. *ApJ Suppl.*, 180:67–83, January 2009b. doi: 10.1088/0067-0049/180/1/67.

G. T. Richards, S. F. Anderson, D. R. Ballantyne, A. J. Barth, W. N. Brandt, R. J. Brunner, G. Chartas, P. Coppi, W. de Vries, M. Eracleous, X. Fan, R. R. Gibson, A. G. Gray, R. F. Green, M. Lacy, P. Lira, G. M. Madejski, J. A. Newman, D. P. Schneider, O. Shemmer, H. Smith, M. A. Strauss, E. Treister, and D. E. Vanden Berk. AGN Science with the LSST. In *American Astronomical Society Meeting Abstracts #215*, volume 42 of *Bulletin of the American Astronomical Society*, page 220, January 2010.

A. G. Riess, A. V. Filippenko, P. Challis, A. Clocchiatti, A. Diercks, P. M. Garnavich, R. L. Gilliland, C. J. Hogan, S. Jha, R. P. Kirshner, B. Leibundgut, M. M. Phillips, D. Reiss, B. P. Schmidt, R. A. Schommer, R. C. Smith, J. Spyromilio, C. Stubbs, N. B. Suntzeff, and J. Tonry. Observational Evidence from Supernovae for an Accelerating Universe and a Cosmological Constant. *A J*, 116: 1009–1038, September 1998. doi: 10.1086/300499.

D. J. Rosario, B. Trakhtenbrot, D. Lutz, H. Netzer, J. R. Trump, J. D. Silverman, M. Schramm, E. Lusso, S. Berta, A. Bongiorno, M. Brusa, N. M. Förster-Schreiber, R. Genzel, S. Lilly, B. Magnelli, V. Mainieri, R. Maiolino, A. Merloni, M. Mignoli, R. Nordon, P. Popesso, M. Salvato, P. Santini, L. J. Tacconi, and G. Zamorani. The mean star-forming properties of QSO host galaxies. *A&A*, 560:A72, December 2013. doi: 10.1051/0004-6361/201322196.

I. G. Roseboom and P. N. Best. Cosmic star formation probed via parametric stack-fitting of known sources to radio imaging. *MNRAS*, 439:1286–1293, April 2014. doi: 10.1093/mnras/stt2452.

N. P. Ross, A. D. Myers, E. S. Sheldon, C. Yèche, M. A. Strauss, J. Bovy, J. A. Kirkpatrick, G. T. Richards, É. Aubourg, M. R. Blanton, W. N. Brandt, W. C. Carithers, R. A. C. Croft, R. da

Silva, K. Dawson, D. J. Eisenstein, J. F. Hennawi, S. Ho, D. W. Hogg, K.-G. Lee, B. Lundgren, R. G. McMahon, J. Miralda-Escudé, N. Palanque-Delabrouille, I. Pâris, P. Petitjean, M. M. Pieri, J. Rich, N. A. Roe, D. Schiminovich, D. J. Schlegel, D. P. Schneider, A. Slosar, N. Suzuki, J. L. Tinker, D. H. Weinberg, A. Weyant, M. White, and W. M. Wood-Vasey. The SDSS-III Baryon Oscillation Spectroscopic Survey: Quasar Target Selection for Data Release Nine. *ApJ Suppl.*, 199:3, March 2012. doi: 10.1088/0067-0049/199/1/3.

M. Rowan-Robinson. Extra-galactic radio source-I. The interpretation of radio source-counts. *MNRAS*, 149:365, 1970. doi: 10.1093/mnras/149.4.365.

V. C. Rubin, W. K. J. Ford, and N. . Thonnard. Rotational properties of 21 SC galaxies with a large range of luminosities and radii, from NGC 4605 /R = 4kpc/ to UGC 2885 /R = 122 kpc/. *Astrophys. J.*, 238:471–487, June 1980. doi: 10.1086/158003.

M. Ryle. Radio stars and their cosmological significance. *The Observatory*, 75:137–147, August 1955.

M. Ryle and R. W. Clarke. An examination of the steady-state model in the light of some recent observations of radio sources. *MNRAS*, 122:349, 1961. doi: 10.1093/mnras/122.4.349.

M. Ryle and P. A. G. Scheuer. The Spatial Distribution and the Nature of Radio Stars. *Proceedings of the Royal Society of London Series A*, 230:448–462, July 1955. doi: 10.1098/rspa.1955.0146.

M. Sako. Spectroscopy of SN II Discovered by the SDSS-II. Subaru Proposal, July 2007.

E. E. Salpeter. Accretion of Interstellar Matter by Massive Objects. *Astrophys. J.*, 140:796–800, August 1964. doi: 10.1086/147973.

A. Sandage. The Existence of a Major New Constituent of the Universe: the Quasistellar Galaxies. *Astrophys. J.*, 141:1560, May 1965. doi: 10.1086/148245.

M. T. Sargent, E. Schinnerer, E. Murphy, C. L. Carilli, G. Helou, H. Aussel, E. Le Floc'h, D. T. Frayer, O. Ilbert, P. Oesch, M. Salvato, V. Smolčić, J. Kartaltepe, and D. B. Sanders. No Evolution in the IR-Radio Relation for IR-luminous Galaxies at z 2 in the COSMOS Field. *ApJ Lett.*, 714: L190–L195, May 2010. doi: 10.1088/2041-8205/714/2/L190.

K. Schawinski, C. J. Lintott, D. Thomas, S. Kaviraj, S. Viti, J. Silk, C. Maraston, M. Sarzi, S. K. Yi, S.-J. Joo, E. Daddi, E. Bayet, T. Bell, and J. Zuntz. Destruction of Molecular Gas Reservoirs in Early-Type Galaxies by Active Galactic Nucleus Feedback. *Astrophys. J.*, 690:1672–1680, January 2009. doi: 10.1088/0004-637X/690/2/1672.

P. Schechter. An analytic expression for the luminosity function for galaxies. *Astrophys. J.*, 203: 297–306, January 1976. doi: 10.1086/154079.

E. Schinnerer, C. L. Carilli, N. Z. Scoville, M. Bondi, P. Ciliegi, P. Vettolani, O. Le Fèvre, A. M. Koekemoer, F. Bertoldi, and C. D. Impey. The VLA-COSMOS Survey. I. Radio Identifications from the Pilot Project. *A J*, 128:1974–1989, November 2004. doi: 10.1086/424860.

M. Schmidt. 3C 273 : A Star-Like Object with Large Red-Shift. *Nature*, 197:1040, March 1963. doi: 10.1038/1971040a0.

M. Schmidt. Space Distribution and Luminosity Functions of Quasars. *Astrophys. J.*, 162:371, November 1970. doi: 10.1086/150668.

D. P. Schneider, G. T. Richards, P. B. Hall, M. A. Strauss, S. F. Anderson, T. A. Boroson, N. P. Ross, Y. Shen, W. N. Brandt, X. Fan, N. Inada, S. Jester, G. R. Knapp, C. M. Krawczyk, A. R. Thakar, D. E. Vanden Berk, W. Voges, B. Yanny, D. G. York, N. A. Bahcall, D. Bizyaev, M. R. Blanton, H. Brewington, J. Brinkmann, D. Eisenstein, J. A. Frieman, M. Fukugita, J. Gray, J. E. Gunn, P. Hibon, Ž. Ivezić, S. M. Kent, R. G. Kron, M. G. Lee, R. H. Lupton, E. Malanushenko, V. Malanushenko, D. Oravetz, K. Pan, J. R. Pier, T. N. Price, III, D. H. Saxe, D. J. Schlegel, A. Simmons, S. A. Snedden, M. U. SubbaRao, A. S. Szalay, and D. H. Weinberg. The Sloan Digital Sky Survey Quasar Catalog. V. Seventh Data Release. *A J*, 139:2360, June 2010. doi: 10.1088/0004-6256/139/6/2360.

S. Serjeant, S. Rawlings, M. Lacy, S. J. Maddox, J. C. Baker, D. Clements, and P. B. Lilje. The radio-optical correlation in steep-spectrum quasars. *MNRAS*, 294:494, March 1998. doi: 10.1046/j.1365-8711.1998.01303.x.

N. Seymour, I. McHardy, and K. F. Gunn. Consistency Between the Radio MIR Source Counts Using the Radio-Mir Correlation. In R. Mújica and R. Maiolino, editors, *Multiwavelength AGN Surveys*, pages 147–148, October 2004. doi: 10.1142/9789812702432_0040.

O. Shemmer, W. N. Brandt, H. Netzer, R. Maiolino, and S. Kaspi. The Hard X-Ray Spectral Slope as an Accretion Rate Indicator in Radio-quiet Active Galactic Nuclei. *ApJ Lett.*, 646:L29–L32, July 2006. doi: 10.1086/506911.

Y. Shen, G. T. Richards, M. A. Strauss, P. B. Hall, D. P. Schneider, S. Snedden, D. Bizyaev, H. Brewington, V. Malanushenko, E. Malanushenko, D. Oravetz, K. Pan, and A. Simmons. A Catalog of Quasar Properties from Sloan Digital Sky Survey Data Release 7. *ApJ Suppl.*, 194:45, June 2011. doi: 10.1088/0067-0049/194/2/45.

J. Silk. Unleashing Positive Feedback: Linking the Rates of Star Formation, Supermassive Black Hole Accretion, and Outflows in Distant Galaxies. *Astrophys. J.*, 772:112, August 2013. doi: 10.1088/0004-637X/772/2/112.

A. K. Sillanpää. The OJ287 supermassive binary black hole model and the new unified scheme for the AGNs. In S. K. Chakrabarti, editor, *Observational Evidence for the Black Holes in the Universe*, volume 234 of *Astrophysics and Space Science Library*, page 209, 1999.

C. Simpson, A. Martínez-Sansigre, S. Rawlings, R. Ivison, M. Akiyama, K. Sekiguchi, T. Takata, Y. Ueda, and M. Watson. Radio imaging of the Subaru/XMM-Newton Deep Field - I. The

100-$\mu$Jy catalogue, optical identifications, and the nature of the faint radio source population. *MNRAS*, 372:741–757, October 2006. doi: 10.1111/j.1365-2966.2006.10907.x.

J. Skilling. Nested Sampling. In R. Fischer, R. Preuss, and U. V. Toussaint, editors, *American Institute of Physics Conference Series*, volume 735 of *American Institute of Physics Conference Series*, pages 395–405, November 2004. doi: 10.1063/1.1835238.

A. Slosar, V. Iršič, D. Kirkby, S. Bailey, N. G. Busca, T. Delubac, J. Rich, É. Aubourg, J. E. Bautista, V. Bhardwaj, M. Blomqvist, A. S. Bolton, J. Bovy, J. Brownstein, B. Carithers, R. A. C. Croft, K. S. Dawson, A. Font-Ribera, J.-M. Le Goff, S. Ho, K. Honscheid, K.-G. Lee, D. Margala, P. Mc-Donald, B. Medolin, J. Miralda-Escudé, A. D. Myers, R. C. Nichol, P. Noterdaeme, N. Palanque-Delabrouille, I. Pâris, P. Petitjean, M. M. Pieri, Y. Piškur, N. A. Roe, N. P. Ross, G. Rossi, D. J. Schlegel, D. P. Schneider, N. Suzuki, E. S. Sheldon, U. Seljak, M. Viel, D. H. Weinberg, and C. Yèche. Measurement of baryon acoustic oscillations in the Lyman-$\alpha$ forest fluctuations in BOSS data release 9. , 4:026, April 2013. doi: 10.1088/1475-7516/2013/04/026.

G. F. Smoot, C. L. Bennett, A. Kogut, E. L. Wright, J. Aymon, N. W. Boggess, E. S. Cheng, G. de Amici, S. Gulkis, M. G. Hauser, G. Hinshaw, P. D. Jackson, M. Janssen, E. Kaita, T. Kelsall, P. Keegstra, C. Lineweaver, K. Loewenstein, P. Lubin, J. Mather, S. S. Meyer, S. H. Moseley, T. Murdock, L. Rokke, R. F. Silverberg, L. Tenorio, R. Weiss, and D. T. Wilkinson. Structure in the COBE differential microwave radiometer first-year maps. *ApJ Lett.*, 396:L1–L5, September 1992. doi: 10.1086/186504.

R. S. Somerville, P. F. Hopkins, T. J. Cox, B. E. Robertson, and L. Hernquist. A semi-analytic model for the co-evolution of galaxies, black holes and active galactic nuclei. *MNRAS*, 391:481–506, December 2008. doi: 10.1111/j.1365-2966.2008.13805.x.

V. Springel, S. D. M. White, A. Jenkins, C. S. Frenk, N. Yoshida, L. Gao, J. Navarro, R. Thacker, D. Croton, J. Helly, J. A. Peacock, S. Cole, P. Thomas, H. Couchman, A. Evrard, J. Colberg, and F. Pearce. Simulations of the formation, evolution and clustering of galaxies and quasars. *Nature*, 435:629–636, June 2005. doi: 10.1038/nature03597.

M. A. Strauss, D. H. Weinberg, R. H. Lupton, V. K. Narayanan, J. Annis, M. Bernardi, M. Blanton, S. Burles, A. J. Connolly, J. Dalcanton, M. Doi, D. Eisenstein, J. A. Frieman, M. Fukugita, J. E. Gunn, Ž. Ivezić, S. Kent, R. S. J. Kim, G. R. Knapp, R. G. Kron, J. A. Munn, H. J. Newberg, R. C. Nichol, S. Okamura, T. R. Quinn, M. W. Richmond, D. J. Schlegel, K. Shimasaku, M. SubbaRao, A. S. Szalay, D. Vanden Berk, M. S. Vogeley, B. Yanny, N. Yasuda, D. G. York, and I. Zehavi. Spectroscopic Target Selection in the Sloan Digital Sky Survey: The Main Galaxy Sample. *A J*, 124:1810–1824, September 2002. doi: 10.1086/342343.

M. E. C. Swanson, M. Tegmark, M. Blanton, and I. Zehavi. SDSS galaxy clustering: luminosity and colour dependence and stochasticity. *MNRAS*, 385:1635–1655, April 2008. doi: 10.1111/j. 1365-2966.2008.12948.x.

Y. Tanaka, K. Nandra, A. C. Fabian, H. Inoue, C. Otani, T. Dotani, K. Hayashida, K. Iwasawa, T. Kii, H. Kunieda, F. Makino, and M. Matsuoka. Gravitationally redshifted emission implying an accretion disk and massive black hole in the active galaxy MCG-6-30-15. *Nature*, 375:659–661, June 1995. doi: 10.1038/375659a0.

S. Tremaine, K. Gebhardt, R. Bender, G. Bower, A. Dressler, S. M. Faber, A. V. Filippenko, R. Green, C. Grillmair, L. C. Ho, J. Kormendy, T. R. Lauer, J. Magorrian, J. Pinkney, and D. Richstone. The Slope of the Black Hole Mass versus Velocity Dispersion Correlation. *Astrophys. J.*, 574: 740–753, August 2002. doi: 10.1086/341002.

R. J. Trumpler and H. F. Weaver. *Statistical astronomy.* 1953.

J. S. Ulvestad, R. R. J. Antonucci, and R. Barvainis. VLBA Imaging of Central Engines in Radio-Quiet Quasars. *Astrophys. J.*, 621:123–129, March 2005. doi: 10.1086/427426.

T. Urrutia, R. H. Becker, R. L. White, E. Glikman, M. Lacy, J. Hodge, and M. D. Gregg. The FIRST-2MASS Red Quasar Survey. II. An Anomalously High Fraction of LoBALs in Searches for Dust-Reddened Quasars. *Astrophys. J.*, 698:1095–1109, June 2009. doi: 10.1088/0004-637X/698/2/1095.

C. M. Urry and P. Padovani. Unified Schemes for Radio-Loud Active Galactic Nuclei. *PASP*, 107: 803, September 1995. doi: 10.1086/133630.

T. Vernstrom, D. Scott, J. V. Wall, J. J. Condon, W. D. Cotton, E. B. Fomalont, K. I. Kellermann, N. Miller, and R. A. Perley. Deep 3 GHz number counts from a P(D) fluctuation analysis. *MNRAS*, 440:2791–2809, May 2014. doi: 10.1093/mnras/stu470.

S. S. Vogt. HIRES - a High Resolution Echelle Spectrometer for the Keck Ten-Meter Telescope. In M.-H. Ulrich, editor, *European Southern Observatory Conference and Workshop Proceedings*, volume 40 of *European Southern Observatory Conference and Workshop Proceedings*, page 223, June 1992.

J. V. Wall and C. A. Jackson. Dual-population radio source unification. *MNRAS*, 290:L17–L22, September 1997. doi: 10.1093/mnras/290.2.L17.

R. L. Webster, P. J. Francis, B. A. Petersont, M. J. Drinkwater, and F. J. Masci. Evidence for a large undetected population of dust-reddened quasars. *Nature*, 375:469–471, June 1995. doi: 10.1038/375469a0.

M. White, M. Blanton, A. Bolton, D. Schlegel, J. Tinker, A. Berlind, L. da Costa, E. Kazin, Y.-T. Lin, M. Maia, C. K. McBride, N. Padmanabhan, J. Parejko, W. Percival, F. Prada, B. Ramos, E. Sheldon, F. de Simoni, R. Skibba, D. Thomas, D. Wake, I. Zehavi, Z. Zheng, R. Nichol, D. P. Schneider, M. A. Strauss, B. A. Weaver, and D. H. Weinberg. The Clustering of Massive Galaxies

at z ~ 0.5 from the First Semester of BOSS Data. *Astrophys. J.*, 728:126, February 2011. doi: 10.1088/0004-637X/728/2/126.

R. L. White, R. H. Becker, D. J. Helfand, and M. D. Gregg. A Catalog of 1.4 GHz Radio Sources from the FIRST Survey. *Astrophys. J.*, 475:479–493, February 1997.

R. L. White, D. J. Helfand, R. H. Becker, E. Glikman, and W. de Vries. Signals from the Noise: Image Stacking for Quasars in the FIRST Survey. *Astrophys. J.*, 654:99–114, January 2007. doi: 10.1086/507700.

S. V. White, M. J. Jarvis, B. Häußler, and N. Maddox. Radio-quiet quasars in the VIDEO survey: evidence for AGN-powered radio emission at S_{1.4 GHz 1} mJy. *MNRAS*, 448:2665–2686, April 2015. doi: 10.1093/mnras/stv134.

I. H. Whittam, J. M. Riley, D. A. Green, M. J. Jarvis, I. Prandoni, G. Guglielmino, R. Morganti, H. J. A. Röttgering, and M. A. Garrett. The faint source population at 15.7 GHz - I. The radio properties. *MNRAS*, 429:2080–2097, March 2013. doi: 10.1093/mnras/sts478.

J. P. Williams, L. Blitz, and C. F. McKee. The Structure and Evolution of Molecular Clouds: from Clumps to Cores to the IMF. *Protostars and Planets IV*, page 97, May 2000.

R. J. Wilman, L. Miller, M. J. Jarvis, T. Mauch, F. Levrier, F. B. Abdalla, S. Rawlings, H.-R. Klöckner, D. Obreschkow, D. Olteanu, and S. Young. A semi-empirical simulation of the extragalactic radio continuum sky for next generation radio telescopes. *MNRAS*, 388:1335–1348, August 2008. doi: 10.1111/j.1365-2966.2008.13486.x.

R. J. Wilman, M. J. Jarvis, T. Mauch, S. Rawlings, and S. Hickey. An infrared-radio simulation of the extragalactic sky: from the Square Kilometre Array to Herschel. *MNRAS*, 405:447–461, June 2010. doi: 10.1111/j.1365-2966.2010.16453.x.

R. A. Windhorst, G. K. Miley, F. N. Owen, R. G. Kron, and D. C. Koo. Sub-millijansky 1.4 GHz source counts and multicolor studies of weak radio galaxy populations. *Astrophys. J.*, 289:494–513, February 1985. doi: 10.1086/162911.

L. Woltjer. Emission Nuclei in Galaxies. *Astrophys. J.*, 130:38, July 1959. doi: 10.1086/146694.

B. Yanny, H. J. Newberg, J. A. Johnson, Y. S. Lee, T. C. Beers, D. Bizyaev, H. Brewington, P. R. Fiorentin, P. Harding, E. Malanushenko, V. Malanushenko, D. Oravetz, K. Pan, A. Simmons, and S. Snedden. Tracing Sagittarius Structure with SDSS and SEGUE Imaging and Spectroscopy. *Astrophys. J.*, 700:1282–1298, August 2009. doi: 10.1088/0004-637X/700/2/1282.

C. Yèche, P. Petitjean, J. Rich, E. Aubourg, N. Busca, J.-C. Hamilton, J.-M. Le Goff, I. Paris, S. Peirani, C. Pichon, E. Rollinde, and M. Vargas-Magaña. Artificial neural networks for quasar selection and photometric redshift determination. *A&A*, 523:A14+, November 2010. doi: 10. 1051/0004-6361/200913508.

D. G. York, J. Adelman, J. E. Anderson, Jr., S. F. Anderson, J. Annis, N. A. Bahcall, J. A. Bakken, R. Barkhouser, S. Bastian, E. Berman, W. N. Boroski, S. Bracker, C. Briegel, J. W. Briggs, J. Brinkmann, R. Brunner, S. Burles, L. Carey, M. A. Carr, F. J. Castander, B. Chen, P. L. Colestock, A. J. Connolly, J. H. Crocker, I. Csabai, P. C. Czarapata, J. E. Davis, M. Doi, T. Dombeck, D. Eisenstein, N. Ellman, B. R. Elms, M. L. Evans, X. Fan, G. R. Federwitz, L. Fiscelli, S. Friedman, J. A. Frieman, M. Fukugita, B. Gillespie, J. E. Gunn, V. K. Gurbani, E. de Haas, M. Haldeman, F. H. Harris, J. Hayes, T. M. Heckman, G. S. Hennessy, R. B. Hindsley, S. Holm, D. J. Holmgren, C.-h. Huang, C. Hull, D. Husby, S.-I. Ichikawa, T. Ichikawa, Ž. Ivezić, S. Kent, R. S. J. Kim, E. Kinney, M. Klaene, A. N. Kleinman, S. Kleinman, G. R. Knapp, J. Korienek, R. G. Kron, P. Z. Kunszt, D. Q. Lamb, B. Lee, R. F. Leger, S. Limmongkol, C. Lindenmeyer, D. C. Long, C. Loomis, J. Loveday, R. Lucinio, R. H. Lupton, B. MacKinnon, E. J. Mannery, P. M. Mantsch, B. Margon, P. McGehee, T. A. McKay, A. Meiksin, A. Merelli, D. G. Monet, J. A. Munn, V. K. Narayanan, T. Nash, E. Neilsen, R. Neswold, H. J. Newberg, R. C. Nichol, T. Nicinski, M. Nonino, N. Okada, S. Okamura, J. P. Ostriker, R. Owen, A. G. Pauls, J. Peoples, R. L. Peterson, D. Petravick, J. R. Pier, A. Pope, R. Pordes, A. Prosapio, R. Rechenmacher, T. R. Quinn, G. T. Richards, M. W. Richmond, C. H. Rivetta, C. M. Rockosi, K. Ruthmansdorfer, D. Sandford, D. J. Schlegel, D. P. Schneider, M. Sekiguchi, G. Sergey, K. Shimasaku, W. A. Siegmund, S. Smee, J. A. Smith, S. Snedden, R. Stone, C. Stoughton, M. A. Strauss, C. Stubbs, M. SubbaRao, A. S. Szalay, I. Szapudi, G. P. Szokoly, A. R. Thakar, C. Tremonti, D. L. Tucker, A. Uomoto, D. Vanden Berk, M. S. Vogeley, P. Waddell, S.-i. Wang, M. Watanabe, D. H. Weinberg, B. Yanny, N. Yasuda, and SDSS Collaboration. The Sloan Digital Sky Survey: Technical Summary. *A J*, 120:1579–1587, September 2000. doi: 10.1086/301513.

M. Young, M. Elvis, and G. Risaliti. The Reddest DR3 SDSS/XMM-Newton Quasars. *Astrophys. J.*, 688:128–147, November 2008. doi: 10.1086/592083.

N. L. Zakamska, K. Lampayan, A. Petric, D. Dicken, J. E. Greene, T. M. Heckman, R. C. Hickox, L. C. Ho, J. H. Krolik, N. P. H. Nesvadba, M. A. Strauss, J. E. Geach, M. Oguri, and I. V. Strateva. Star formation in quasar hosts and the origin of radio emission in radio-quiet quasars. *MNRAS*, 455:4191–4211, February 2016. doi: 10.1093/mnras/stv2571.

J. Zwart, J. Wall, A. Karim, C. Jackson, R. Norris, J. Condon, J. Afonso, I. Heywood, M. Jarvis, F. Navarrete, I. Prandoni, E. Rigby, H. J. A. Rottgering, M. Santos, M. Sargent, N. Seymour, R. Taylor, and T. Vernstrom. Astronomy Below the Survey Threshold in the SKA Era. *Advancing Astrophysics with the Square Kilometre Array (AASKA14)*, art. 172, 2015a.

J. T. L. Zwart, M. J. Jarvis, R. P. Deane, D. G. Bonfield, K. Knowles, N. Madhanpall, H. Rahmani, and D. J. B. Smith. The star formation history of mass-selected galaxies from the VIDEO survey. *MNRAS*, 439:1459–1471, April 2014. doi: 10.1093/mnras/stu053.

J. T. L. Zwart, M. Santos, and M. J. Jarvis. Far beyond stacking: fully Bayesian constraints on sub-$\mu$Jy radio source populations over the XMM-LSS-VIDEO field. *MNRAS*, 453:1740–1753, October 2015b. doi: 10.1093/mnras/stv1716.

F. Zwicky. On the Masses of Nebulae and of Clusters of Nebulae. *Astrophys. J.*, 86:217, October 1937. doi: 10.1086/143864.